



NASA CR-159,544

NASA CR-159544
R79AEG197



National Aeronautics and
Space Administration

NASA-CR-159544
19790023177

CONTAINMENT OF COMPOSITE FAN BLADES FINAL REPORT

by

C.L. Stotler

A.P. Coppa

GENERAL ELECTRIC COMPANY

July 1979

LIBRARY COPY

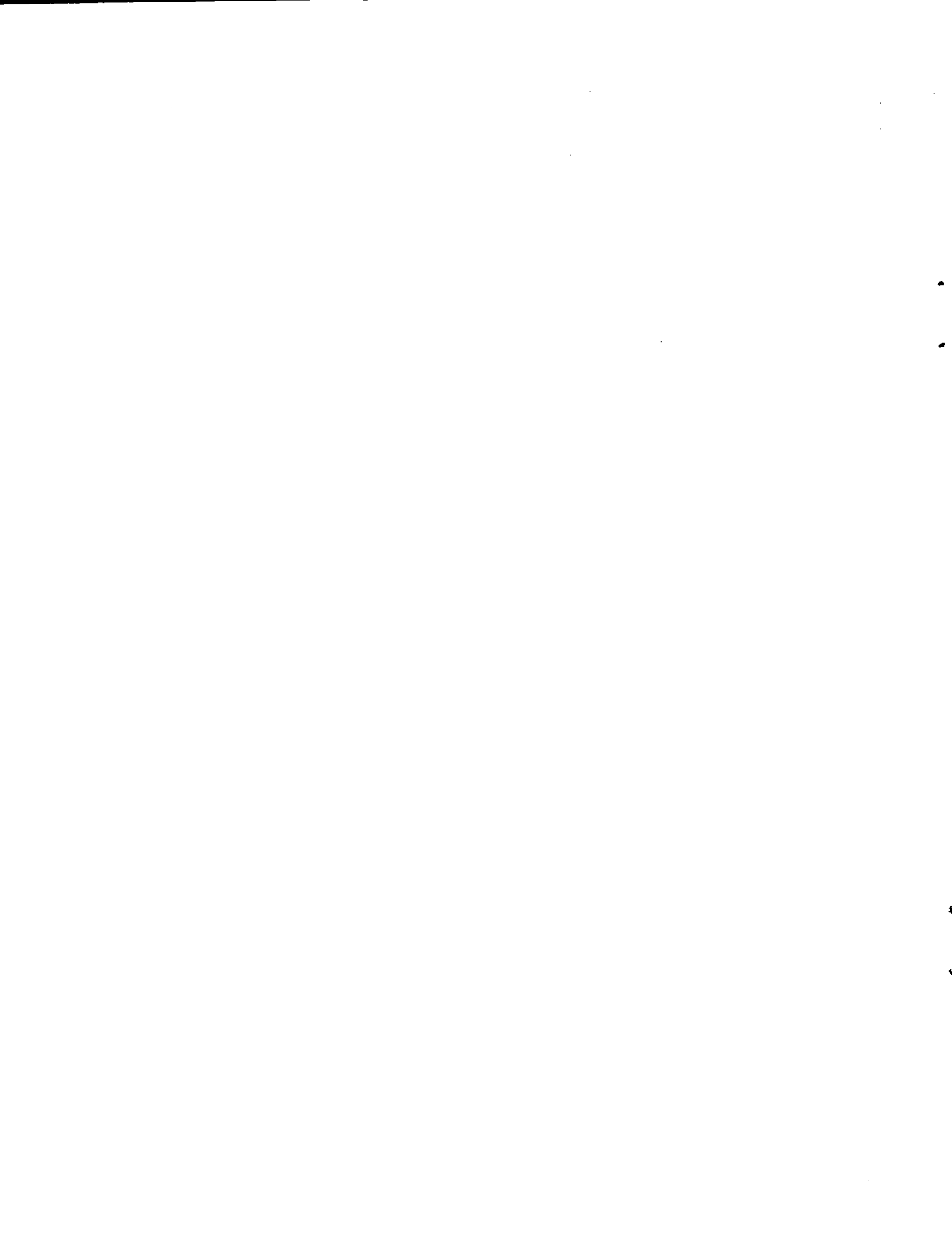
SEP 18 1979

Prepared For

LANGLEY RESEARCH CENTER
LIBRARY, NASA
HAMPTON, VIRGINIA

National Aeronautics and Space Administration

NASA Lewis Research Center
Contract NAS3-20118



1. Report No. NASA CR-159544	2. Government Accession No.	3. Recipient's Catalog No.	
4. Title and Subtitle Containment of Composite Fan Blades Final Report		5. Report Date July 1979	
		6. Performing Organization Code	
7. Author(s) C. L. Stotler, A. P. Coppa		8. Performing Organization Report No. R79AEG197	
		10. Work Unit No.	
9. Performing Organization Name and Address General Electric Company Aircraft Engine Group Cincinnati, Ohio 45215		11. Contract or Grant No. NAS3-20118	
		13. Type of Report and Period Covered Contractor Report	
12. Sponsoring Agency Name and Address National Aeronautics & Space Administration Washington, D. C. 20546		14. Sponsoring Agency Code	
		15. Supplementary Notes Final Report, Project Manager G. T. Smith NASA - Lewis Research Center Cleveland, Ohio 44135	
16. Abstract A lightweight containment was developed for turbofan engine fan blades. Subscale ballistic-type tests were first run on a number of concepts. The most promising configuration was selected and further evaluated by larger scale tests in a rotating test rig. Weight savings made possible by the use of this new containment system were determined and extrapolated to a CF6-size engine. An analytical technique was also developed to predict the released blades motion when involved in the blade/casing interaction process. Initial checkout of this procedure was accomplished using several of the tests run during the program.			
17. Key Words (Suggested by Author(s)) Containment Composite Materials Fan Casing Fan Blades		18. Distribution Statement	
19. Security Classif. (of this report) Unclassified	20. Security Classif. (of this page) Unclassified	21. No. of Pages 159	22. Price*

* For sale by the National Technical Information Service, Springfield, Virginia 22151

N79-31345 #

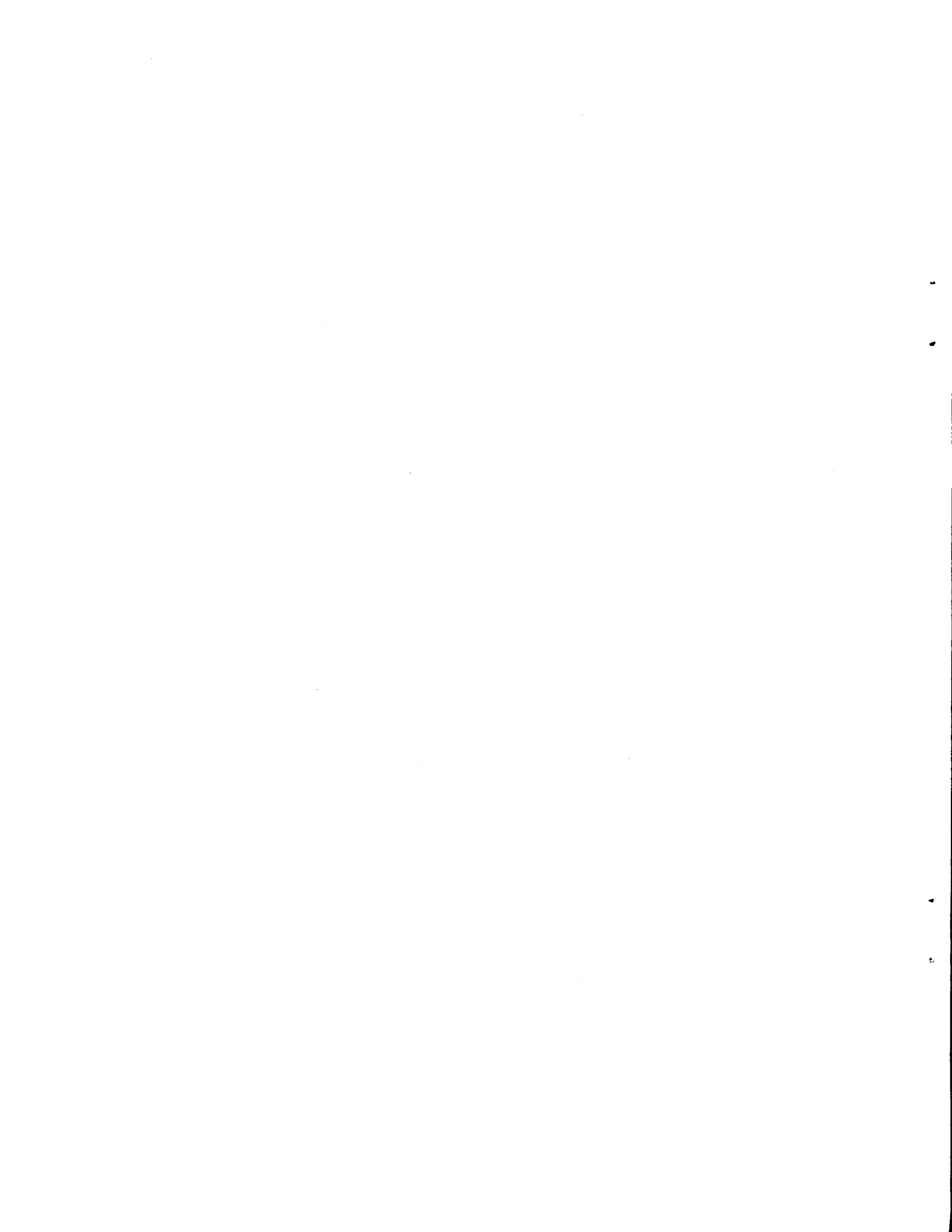


TABLE OF CONTENTS

<u>Section</u>		<u>Page</u>
1.0	SUMMARY	1
2.0	INTRODUCTION	3
3.0	BACKGROUND	6
	3.1 Blade Containment Process - Current Design Practice	6
	3.2 Developments Toward Improved Containment Systems	8
4.0	TECHNICAL DISCUSSION	12
	4.1 Task I - Analytical Determination of Blade Impact Conditions	12
	4.2 Task II - Blade Impact Penetration Tests	21
	4.2.1 Containment Scaling Basis	21
	4.2.2 Comparison of Ballistic and Rotating Test Techniques	24
	4.2.3 Test Method Description	25
	4.2.4 Projectile Description	29
	4.2.5 Containment Description	29
	4.2.6 Test Results	33
	4.3 Task III - Design and Fabrication of Blade Containment Systems	78
	4.4 Task IV - Test Evaluation of Blade Containment Systems	81
	4.4.1 Test Facility Description	81
	4.4.2 Test Results	84
	4.5 Task V - Formulation of Blade Containment Systems Requirements	106
	4.5.1 Correlation of Test Results with Analysis	106
	4.5.2 Design Criteria Definition	127
	4.5.3 Full-Scale Containment System Evaluation	128
5.0	CONCLUSIONS AND RECOMMENDATIONS	133
	5.1 Conclusions	133
	5.2 Recommendations	133
6.0	REFERENCE	136
	DISTRIBUTION LIST	137

LIST OF ILLUSTRATIONS

<u>Figure</u>		<u>Page</u>
1	Typical Bird Impact Damage to Metallic Fan Rotor.	2
2	Typical State-of-the-Art Containment Case.	5
3	Undesirable Fragment Interactions.	10
4	Stratified Containment Structure Design Concept.	11
5	Containment Structure Model Used in the Computer Program.	13
6	Blade Fragment Model.	15
7	Geometry of Analytical Containment Model.	16
8	Gas Gun Containment Test Facility.	26
9	Containment Structure Segment.	27
10	Titanium Projectile.	30
11	Superhybrid Composite Projectile.	31
12	Blade Projectile and Mounting Arrangement on Sabot.	32
13	Finned-Type Containment Specimens.	34
14	Short-Finned Kevlar/Epoxy Laminate.	35
15	Long-Finned Kevlar/Epoxy Laminate.	36
16	Long-Finned 6Al-4V Titanium.	37
17	Long-Finned 2024 T-3 Aluminum Structure.	38
18	Nonfinned-Type Containment Structure.	39
19	Kevlar Cloth-Filled Concept.	40
20	Honeycomb-Filled Concept.	41
21	Current Practice Sheet Metal Ring.	42
22	Posttest Condition of Type 321 Stainless Steel Containment Structure Showing Overall Out-of-Roundness Deformation - Blade Impact Velocity \sim 260 m/sec (850 ft/sec).	46

LIST OF ILLUSTRATIONS (Continued)

<u>Figure</u>		<u>Page</u>
23	View of Inner Surface of Type 321 Stainless Steel Containment Structure After Impact at a Velocity of ~ 260 m/sec (850 ft/sec) Showing Large Local Deformation and Track of Blade Projectile.	47
24	Steel Containment Structure After Tests 1 and 2.	49
25	Steel Containment Structure After Tests 3 and 4.	50
26	Superhybrid Impact on Kevlar Belt Target.	52
27	Superhybrid Projectile Contained by Kevlar Belt Target.	53
28	Titanium Projectile Contained by Kevlar Belt Target.	54
29	Impact Side of Transverse Honeycomb Target.	57
30	Typical Exit Side - Penetration of Transverse Honeycomb Target.	58
31	Impact Side of Titanium Finned Target After Impact of a Superhybrid Projectile.	59
32	Titanium Projectile Contained by Titanium Finned Target.	60
33	Penetration of Aluminum Finned Target.	62
34	Exit Side - Aluminum Finned Target - Test 13.	64
35	Short-Finned Kevlar Target After Impact.	66
36	Test 17 - Side View.	67
37	Test 17 - Interior Closeup.	68
38	Test 17 - Exterior Closeup.	69
39	Test 18 - Side View.	70
40	Test 18 - Interior Closeup.	71
41	Test 18 - Exterior Closeup.	72
42	Test 19 - Exterior Closeup.	74

LIST OF ILLUSTRATIONS (Continued)

<u>Figure</u>		<u>Page</u>
43	Test 20 - Side View.	75
44	Test 20 - Interior Closeup.	76
45	Test 20 - Exterior Closeup.	77
46	Thickness of Kevlar Required Versus Kinetic Energy Gas Gun Data.	79
47	Steel/Kevlar Containment Concepts.	80
48	Basic Whirligig Test Setup.	83
49	TF34 Titanium Blade.	85
50	TF34 Superhybrid Titanium Composite TiCom Blade.	86
51	Composite Containment System - Test 1.	88
52	Composite Casings Following Test 1.	90
53	Honeycomb Casing Showing Outer Wall Following Rotating Test 1.	91
54	Composite Containment System - Test 2, Before Test.	93
55	Impact Location, Right Side, Following Test 2.	94
56	Impact Location, Left Side, Following Test 2.	95
57	Casings From Test 2 Following Removal From Test Facility.	96
58	Composite Containment System Following Impact Test 3.	98
59	Impact Location Showing Nested Blade - Test 3.	99
60	Containment Half-Ring With Steel Inner Liner Removed Following Test 3.	100
61	Test Part with Honeycomb Removed Showing Precured Kevlar/Epoxy.	101
62	Test Part Showing Dry Kevlar with Precured Kevlar/Epoxy Peeled Back.	102

LIST OF ILLUSTRATIONS (Concluded)

<u>Figure</u>		<u>Page</u>
63	Whirligig Test Setup Before Test 4.	103
64	Containment Test 4 Following Impact.	105
65	Calculated Interaction of a Task II Titanium Blade Projectile with Finned-Type Containment Structure.	109
66	Calculated Blade Motion Parameters Corresponding to Figure 65.	110
67	Computed Blade Trajectory - TF34 Rotating Test 3.	114
68	Computed Blade χ Displacement Versus Time - Rotating Test 3.	115
69	Computed Blade θ Displacement Versus Time - Rotating Test 3.	116
70	Computed Blade ϕ Displacement Versus Time - Rotating Test 3.	117
71	Computed Blade Kinetic Energy Versus Time - Rotating Test 3.	118
72	Computed Blade Velocity ∇ Versus Time - Rotating Test 3.	119
73	Computed Blade Velocity θ Versus Time - Rotating Test 3.	120
74	Computed Blade Velocity ϕ Versus Time - Rotating Test 3.	121
75	Computed Blade Relative Positions $T = 0$.	122
76	Computed Blade Relative Positions $T = 6 \times 10^{-4}$ Seconds.	123
77	Computed Blade Relative Positions $T = 13.5 \times 10^{-4}$ Seconds.	124
78	Computed Blade Relative Positions $T = 15 \times 10^{-4}$ Seconds.	125
79	Thickness of Kevlar Versus Kinetic Energy - All Test Data.	129
80	State-of-the-Art Steel Containment Ring.	131
81	Lightweight Containment System.	132
82	Amount of Kevlar Required Versus Kinetic Energy.	135

LIST OF TABLES

<u>Table</u>		<u>Page</u>
I	Scaling Relationships.	22
II	Projectile Impact Testing Summary.	43
III	Planned Tests.	87
IV	Revised Test Plan.	92
V	Structure Input Data for Run 10.	107
VI	Containment Structure Analysis Input Data for Rotating Test 3.	112
VII	Computed Blade Displacements and Velocities - TF34 Rotating Rig - Test 3.	113
VIII	Time Values (T) Corresponding to Time Points (NT) for TF34 Rotating Test 3 Trajectory Plot (Figure 67).	126

1.0 SUMMARY

This report presents the results of the analysis and test effort performed under Contract NAS3-20118. "Containment of Composite Fan Blades". Originally, this program's principal objective was to determine the containment weight that could be saved if composite fan blades were to replace the current titanium fan blades. It was expected that this weight savings would have two sources: (1) the higher frangibility of the composite blades, resulting in smaller fragments to be contained, and (2) the introduction of a new, lightweight containment design concept.

As the program progressed, the containment weight savings allowed by using a frangible blade became apparent. But this frangibility had a drawback: it would make lightweight blades more vulnerable during random bird strikes. Since this problem was delaying the introduction of composite fan blades in production engines, it was decided to direct the major portion of the program towards the lightweight containment aspect and develop these concepts for the containment of current titanium blades.

A number of concepts was investigated which used various forms of aluminum, titanium, steel, composites, and combinations thereof. These concepts were initially evaluated using a 0.102 m (4 in.) diameter gas gun to propel blade-like fragments into 0.6096 m (24 in.) diameter 180° subscale containment rings representing the concepts being investigated. The efficiency of each concept was evaluated using high-speed photography. The evaluation criteria were weight, impact resistance, fragment retention, and ability to remain round. Of the concepts tested, the one which demonstrated the most energy-absorbing capability per unit weight consisted of a thin steel facing backed up by a number of layers of dry Kevlar cloth. Not only did this concept have good energy-absorbing characteristics, but the fragments were retained by the system.

This concept was further investigated in a rotating rig using TF34 fan blades. Both titanium and superhybrid versions of this blade were used. The superhybrid version consisted of a titanium spar, a graphite/glass/epoxy shell, and a titanium foil outer covering. The amount of Kevlar used was based on the results of the subscale testing. Between the steel face and the Kevlar cloth some of these TF34 size containment rings had aluminum honeycomb to provide a nesting area (not evaluated during the gas gun testing) for the released blade fragment so that it would not protrude into the rotor path. This feature worked very well and should be incorporated into any containment design of this general configuration.

The results of the rotating rig tests were used to project a containment system design for a CF6-50 size engine. The results of this study indicated an 18% weight savings on a retrofit basis but a 30 to 40% potential savings on an original equipment basis for a new engine.

In addition to the empirical testing performed during the program, an analytical approach was developed to predict the motion of the released blade as it interacts with the containment system. The analysis takes into account the fact that various layers of the containment ring may have different resistances depending on material and construction. The analysis was checked against several of the tests and gave a reasonable representation of the motion of the released blade as it interacts with the containment case.

The overall result of the program was to develop and demonstrate a new, lightweight containment system for engine fan blades, a system that shows promise of significant weight savings over current containment designs.

2.0 INTRODUCTION

One of the primary requirements of modern, high-bypass turbofan engine installations in commercial service is that they contain any fan blades or pieces of blades should a failure occur to prevent any damage to the rest of the aircraft. The size of the objects to be contained ranges from a complete blade airfoil to pieces of blades such as would result from bird impact. The type of damage caused by a bird strike on titanium blades can be seen in Figure 1.

Current containment practice is to install heavy steel rings around the nacelle fan area. A typical containment ring is shown in Figure 2. In large turbofan engines, this can amount to over 181 kg (400 lb). Except for the rare occasion when debris must be contained, this heavy structure serves little purpose yet adds significantly to engine weight and fuel consumption. With the advent of advanced composites as potential structural materials, two possibilities for reducing the weight of the containment system became apparent. The greatest weight savings should be obtainable when both the fan blades and the containment system are constructed using composite materials. Not only should this approach provide a containment system lighter than a steel ring, based on equivalent energy absorbing capability, but the fracture characteristics of composite blades should result in smaller masses to be contained, lowering the energy absorption requirements. Even if composite blades are not considered, much weight can still be saved through the proper use of composites in an overall hybrid containment system designed to contain titanium fan blades.

In order to quantify these potential weight savings, the program discussed herein was performed. The original goal was limited to evaluating the containment weight that could be saved just through the use of composite blades. But as the program progressed, the goal was expanded to include a second objective - determine how much weight could be saved by using advanced containment systems to contain titanium blades. A number of advanced containment systems was then evaluated using subscale simulated blades of both composite and titanium construction. Based on the results of these tests, the most promising system was selected and further evaluated in a rotating test rig.

In addition to the generation of empirical data on advanced containment systems, an analytical technique was developed to predict the motion of a released blade as it contacts the containment system.

By correlating this analysis to the test results, the containment process was better understood, and the program did not have to rely exclusively on test data to design containment casings.

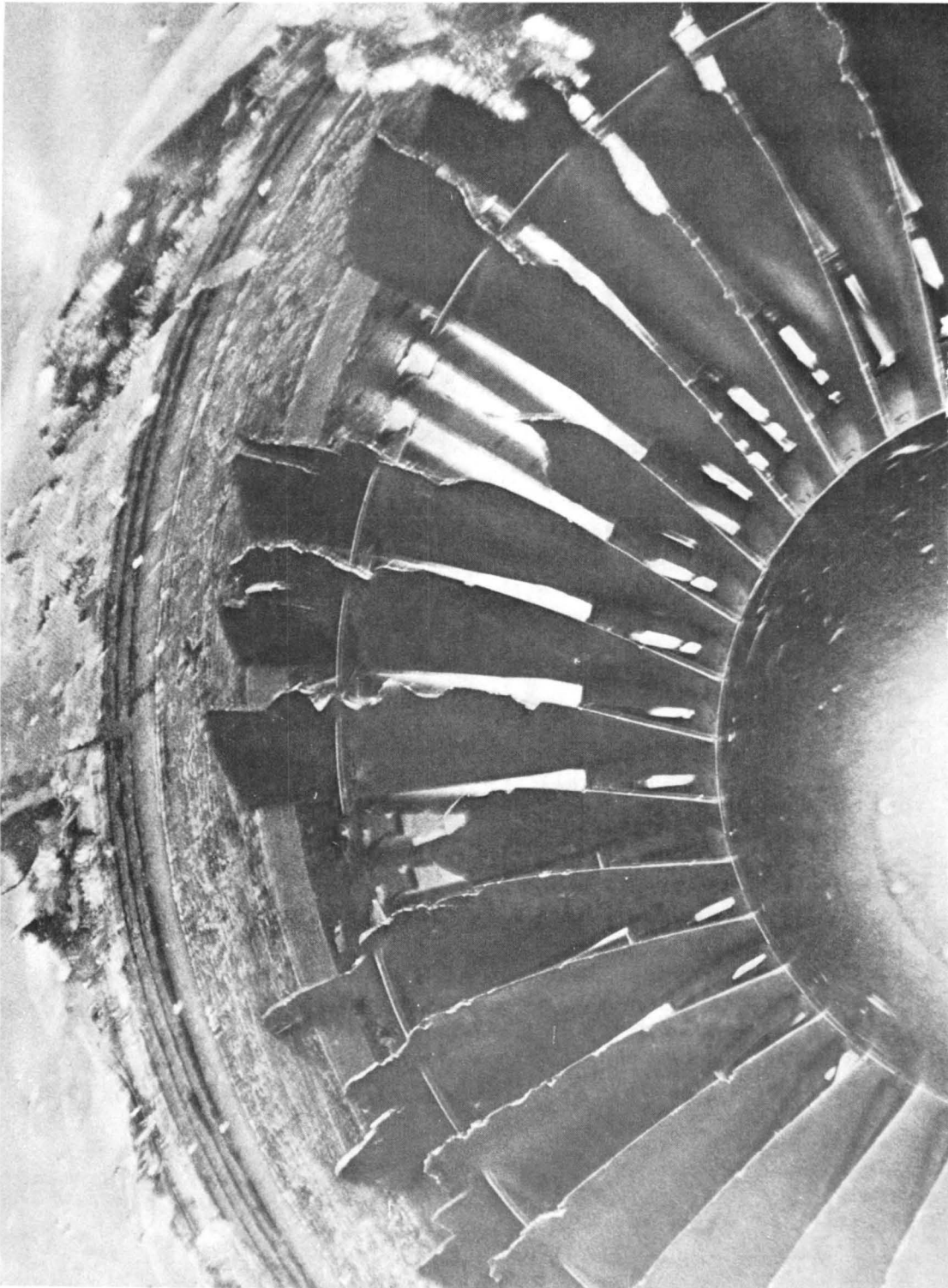


Figure 1. Typical Bird Impact Damage to Metallic Fan Rotor.

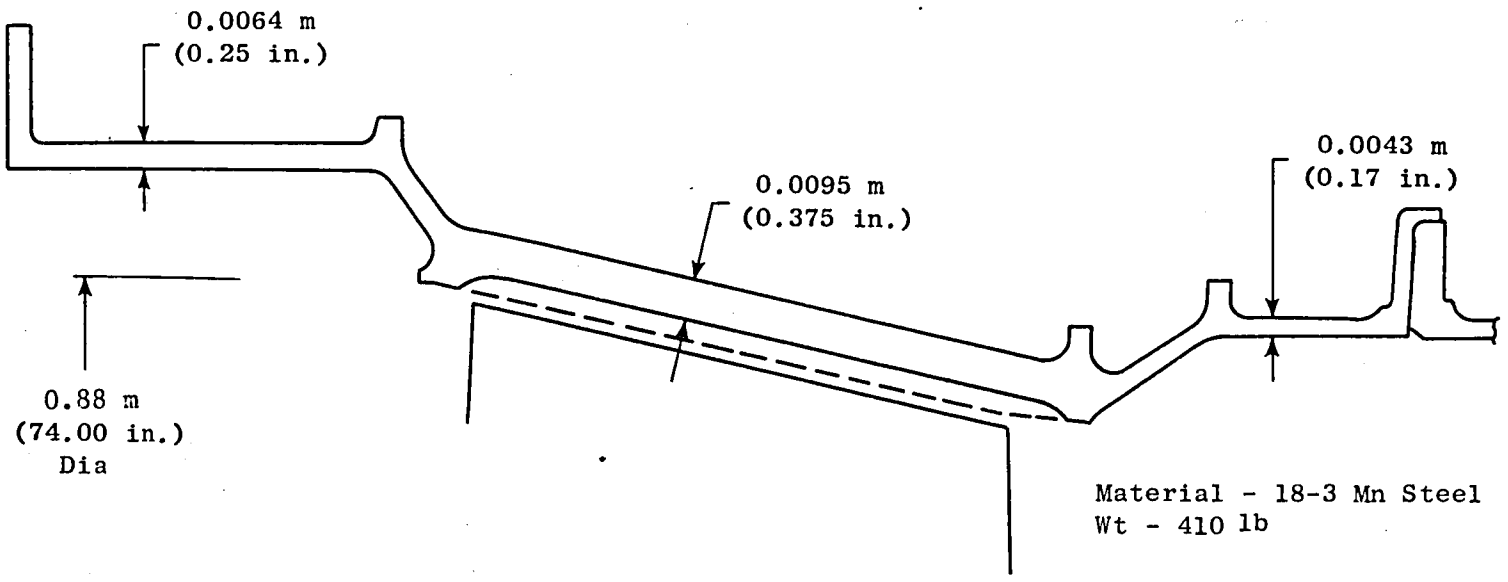


Figure 2. Typical State-of-the-Art Containment Case.

3.0 BACKGROUND

3.1 BLADE CONTAINMENT PROCESS - CURRENT DESIGN PRACTICE

The containment of failed rotor blades is a complex process involving violent, high-speed interactions among numerous local and remotely located engine components such as the failed blades, attached blades, containment structure, adjacent casings, stator vanes, bearings, and bearing supports. Once initiated, the process is dependent on a sequence of largely accidental events whose course and ultimate conclusion are difficult to predict. To give a better understanding of the containment problem, the effects of some of the more important structural interactions that are observed with current design practice are discussed below.

Blade Motion

For a full blade, released at the root with a clean, instantaneous break, the blade center of gravity moves tangentially while the blade continues to rotate. However, the blade immediately contacts the casing in the tip region. This slows the tip, moves it forward due to blade camber, and locally deforms or fractures the blade and shroud. Further, the trailing blade almost immediately contacts the released blade near its root and tends to accelerate the root rearward and circumferentially. Bending and twisting moments also are applied to the blade by the casing and the trailing blade. In addition, the initial blade release flaw may not be uniform chord-wise, so the blade will be tipped forward or aft depending on the fore and aft restraint release sequence as the root region fails. Large forces also are applied to the trailing blade, and it, too, may be totally or partially released. A further degree of complication is introduced by tip or midspan blade shrouds and the forces they apply to the blades. Due to the violent forces, the released blade and following blades are drastically deformed or fractured during the process.

Casing Motion

As the released blade initially contacts the casing and containment structure, it tends to push the casing outward circumferentially and rearward. The rearward force is due to the blade camber and plowing effect of the blade tip. As the casing slows the released blade, a "wedging" action can quickly build up as the trailing blades successively overtake and impact the released blade. These impacts tend to force the blade outward, and rearward, with resultant violent forces applied to the casing. The rotor immediately moves off-center due to unbalance, so the remaining blade tips may begin to rub heavily on the casing. This effect is accentuated by the out-of-roundness which the casing acquires from the initial impact. Hence, the casing, to a degree, is constrained by the blade

tips to follow the orbiting motion of the rotor as it rotates about a new center. In effect, the blade tip-to-casing rub region becomes a new bearing which introduces very strong rearward and circumferential forces on the casing. The localized forces on the casing produce deformation.

Rotor Motion

As the blade is released, the rotor immediately moves off-center due to unbalance forces which for large engines may range from 445,000 to 890,000 N (100,000 to 200,000 lb). This causes a very heavy tip rub, mentioned above, which applies large circumferential and forward forces on the rotor. These forward forces, per blade, can build up to significant fractions of the centrifugal force per blade. The normal rotor bearing may become greatly overloaded radially and axially which can bring on rapid deterioration.

The bearing static structure also deforms both elastically and perhaps plastically as it absorbs the large loads.

Frame Motion

The casing and rotor forces are transmitted to the frame, where they cancel each other to some extent. The balance of the forces is transmitted through the mounts and core engine interfaces.

The torques applied to the casing by the rotor and debris are not cancelled by the rotor and, hence, must be carried by the frame and casing into the mount structure. These torques are increased to some extent by any core rotor torques and low pressure turbine torques which might occur from rubs due to the heavy vibration.

Inlet Motion

The inlet normally is carried on the fan casing. Due to its large size, stiffness, and forward center of gravity, it, too, is a major element in the system dynamics. Specifically, it will apply large inertial forces to the casing and also provide a large amount of axial stiffening as well as some circumferential stiffening. Keeping the inlet-to-casing fastenings intact as the casing distorts is an important requirement.

Casing Rub Strip

The casing normally has a special "soft" rub strip region over the blades. It may be open or filled honeycomb or another readily abrasible material. It permits normal operation with close tip clearance. In the event of a modestly heavy rub due to high vibrations or excessive maneuver forces, this rub strip readily deforms to limit the rotor blade and casing

damage. The strip is fairly thin and is closely backed up by the containment ring. Industry practice generally is to place the ring quite close to the blade tips, so that the blade contacts the ring immediately after release. This limits the radial impact velocity to a small value, since the initial blade motion is tangential. A rapid shroud load buildup is still required to prevent a rapid increase in radial velocity. Although the close clearance is desirable to limit the radial velocity increase, it perhaps is undesirable because it prevents easy exit of debris from the rotor blade tip region and accentuates the rotor-to-casing rub and the resultant forces and torques.

Containment Ring

To a large extent, the containment ring and casing are combined in one physical part. The containment ring must extend over the blade tips and also fore and aft beyond the tips to catch debris with axial velocities. It has been desirable, therefore, to use the containment ring to support the rub strip and, in large fan stages, to support the inlet. The inlet support integrity, however, must be maintained during the containment process.

The containment ring normally is made of a single layer of high ductility, high-strength steel. Energy absorption capacity is a major selection parameter. Fabricability and cost are also important. In the thickness required for containment, the ring essentially is a thin hoop with little capability to maintain its own roundness during local loading. Hence, the roundness and support of the ring come primarily from the frame, the inlet, and (to some degree) the blade tips during a heavy rub. Other engine components, such as the accessory gearbox, may be mounted on or near the containment ring and may introduce significant loads during high vibratory operation. The ring must be hard enough to prevent penetration by fragments, yet soft enough to yield and absorb energy.

3.2 DEVELOPMENTS TOWARD IMPROVED CONTAINMENT SYSTEMS

Design solutions for containment systems can be produced only when an adequate understanding of the above interactions is effectively applied. Previous research (Reference 1) has been directed at gaining a better understanding of the blade containment process. That work resulted in an insight about the process, namely, that the character of the process itself is highly dependent on the containment casing design. A well-designed case can accomplish an orderly, controlled arrest of blade fragments with a minimum of secondary damage. A poorly designed case, however, tends to induce a disorderly process in which blade fragments, casing, and rotor undergo mutually destructive interactions whose outcome may be highly accidental. This is because the fragments aggravate the containment process as long as they continue to interact with rotor components.

Some of these deleterious effects are illustrated by the two examples shown in Figures 3A and 3B. Figure 3A depicts a relatively thick and rigid metallic containment ring that surrounds a counterclockwise rotating row of blades. Blade fragment A, having separated from the disk when it was at the 2 o'clock position, now is forced between the ring and other blades. This sets up severe interactions with the other blades and the casing. The result is severe secondary damage to these components and probable release of other blades. A similar result is produced with a relatively thin and flexible metallic ring, shown in Figure 3B, although the initial action is different. The ring readily deflects under the action of the released blade and thereby the severity of interaction is momentarily reduced relative to that corresponding to Figure 3A. Severe interactions quickly occur between the released blade and the rotor, however, as the deflecting ring moves against them. This process can also result in breakaway of other blades. In addition, the penetration as well as sidewise escape capability of blade fragments is enhanced as they move along highly deformed portions of the containment ring.

In sharp contrast to the above is the containment process associated with a "stratified" casing design concepts illustrated in Figure 4. The structure consists of a relatively thick, readily penetrable, low-resistance inner layer attached to a relatively thin, high-resistance outer layer. The layers are so constructed that their assembly has high overall bending and torsional rigidity. When a released blade fragment engages such a structure, it penetrates into the thick inner layer in a predictable manner, nesting deeper and deeper into it. This action minimizes interaction with other blades. The outer layer provides the additional resistance that is required to assure containment of the fragment. High overall rigidity of the combined structure serves to minimize rubbing interactions with the rotor. As a result, secondary damage effects can be greatly limited.

During the present program, such a process was demonstrated under rotating conditions for the first time. The essential orderliness of the process makes possible the design and development of predictable and optimum containment system.

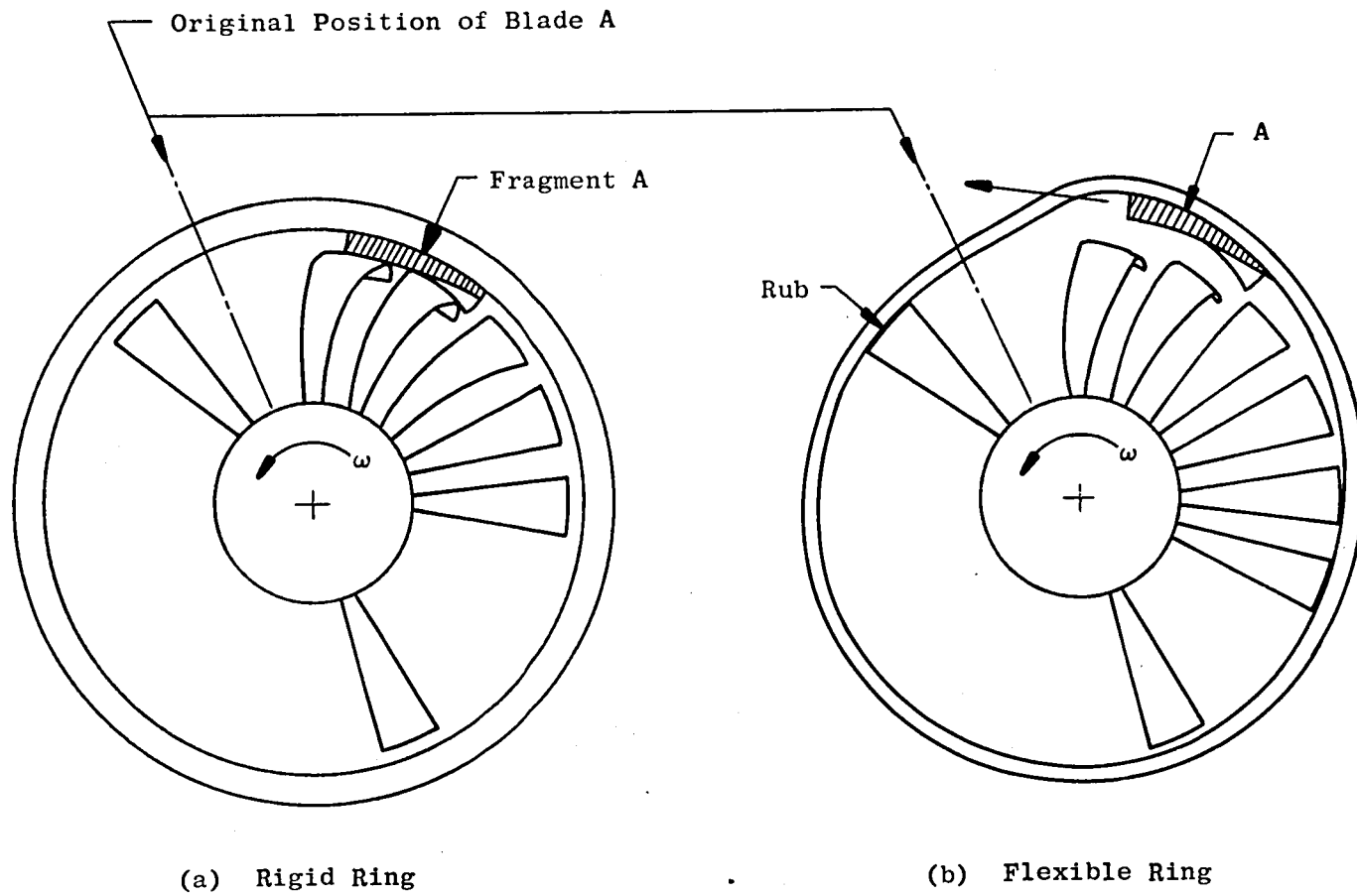


Figure 3. Undesirable Fragment Interactions.

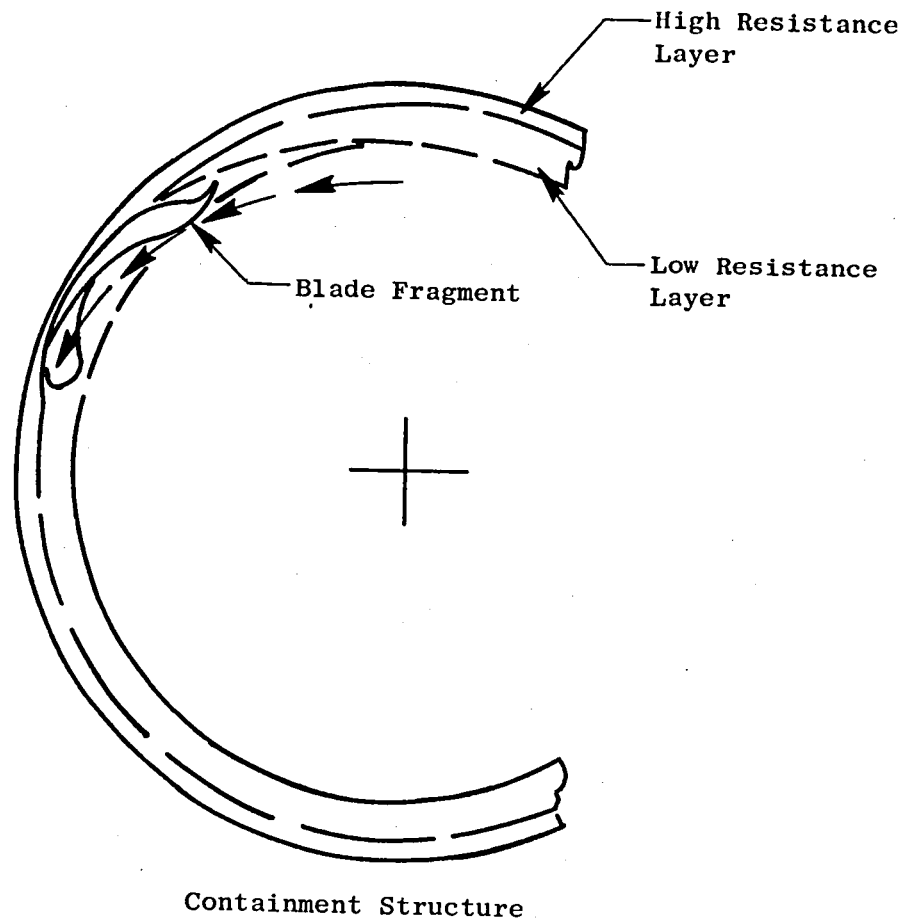


Figure 4. Stratified Containment Structure Design Concept.

4.0 TECHNICAL DISCUSSION

This section presents the results of the technical effort performed under this program. This work was divided into five specific tasks and is discussed below.

4.1 TASK I - ANALYTICAL DETERMINATION OF BLADE IMPACT CONDITIONS

The objective of this task was to develop a method to analytically predict the interaction between a failed fan blade and the blade containment structure.

With recognition of what is involved in the containment process discussed above, an analysis was developed to define the blade/casing interaction. This analysis considers the motion of a blade fragment as it interacts with a containment structure. The structure illustrated in Figure 5 is characterized as an assembly of concentric circular cylindrical layers whose central axis is coincident with the rotational axis of the rotor. These layers are assumed to be so bound together that their assembly obtains high circumferential and torsional rigidity. Another feature of the assembly is that inner layers are generally more bulky and readily penetrated than the outer ones. Hence, as the fragment penetrates the inner region, it experiences relatively low, design-controllable resistance that causes the fragment to move into a flatter circumferential orientation relative to the structure. In a properly designed situation, this action permits the fragment to become nested within the structure, thereby minimizing destructive contact with other blades that remain attached to the rotor, and finally to be arrested and retained totally within the confine of the structure.

The outer layers are generally denser and more resistant than the inner layers and provide a structural base for the latter. They participate in various ways in the fragment deceleration process. They provide toughness for resisting rupture and puncture, and they limit the maximum radial displacement of the fragment.

The material of all layers is assumed to respond in a localized manner as the blade moves through it; that is, the material is assumed to not transmit deformations to remote parts of the containment structure. This assumption implies that localized failure mechanisms such as crushing, shearing, or small-scale rupture dominate the material's response to the action of the fragment. This material characteristic further implies a type of construction that is generically cellular; that is, made up of a distribution of relatively thin-walled elements and interstitial spaces. These spaces may be occupied by air or by material that is readily compressed to a small volume.

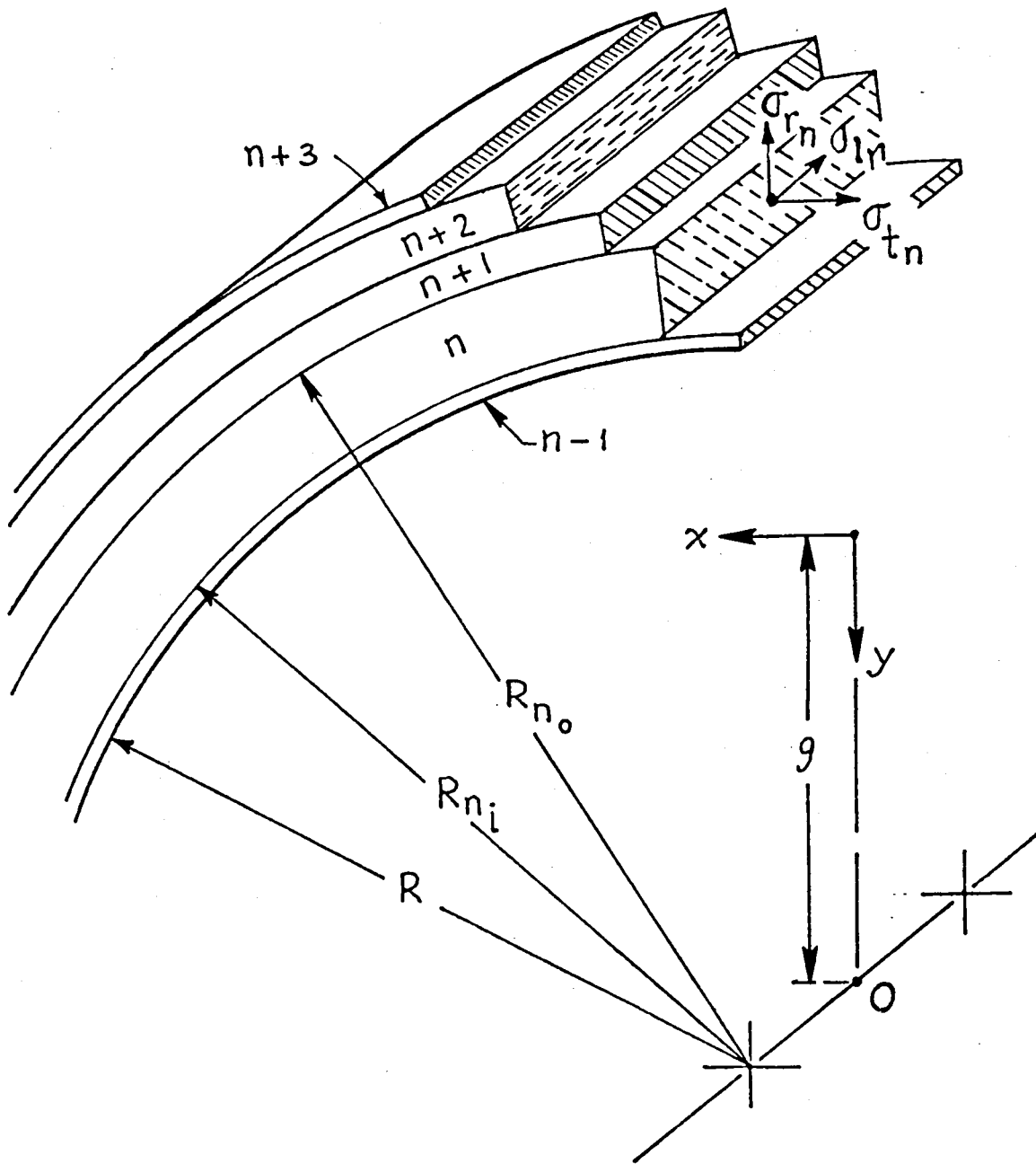


Figure 5. Containment Structure Model Used in the Computer Program.

For any particular layer, designated by subscript n, the material is assumed to offer three orthogonal constant structural resistances: σ_{tn} , σ_{rn} , and σ_{ln} , where subscripts t, r, and l refer to the circumferential, radial, and longitudinal directions through the point of application. Also present are friction components corresponding to the constant coefficients, μ_{tn} , μ_{rn} , and μ_{ln} .

The blade fragment is modeled as a rigid rectangular solid as shown in Figure 6. The face of the blade is divided into rectangular elements identified by the indices ij ; the tip and base edges into elements $i1$ and $i2$, respectively; and leading and trailing edges into elements, lj and $2j$, respectively. These elements are referenced about coordinate axes z and c which move with the blade fragment and whose origin is at the fragment center-of-mass.

The instantaneous position of the blade fragment center-of-mass is defined by the coordinates x and $g-y$ relative to the fixed axes x and y . The origin of these axes is coincident with the initial position of the center-of-mass which is located vertically above point 0 (the intersection of the engine rotor axis with x , y plane) by a distance, g , as shown in Figure 7. The angular orientation of the fragment is defined by the angles θ and ϕ ; θ is the angle between the fragment central axis (coincident with the blade airfoil stacking axis) and the negative y axis, and ϕ is the angle between the blade chord axis C and the $x-y$ plane, measured from the leading edge and in the plane normal to the fragment central axis.

Interaction forces between the containment structure and the blade are calculated for each face, section, and edge element of the blade fragment. The forces are nonzero only for those elements that are in contact with the structure, that is, moving against the structural material. For example, when both the leading and trailing edges of the blade are located within the containment structure, forces will only act on those edge elements which are moving into (engaging) the structural material. Corresponding elements on the opposite edge will have zero forces imposed on them, as will all elements that are not located within the containment structure.

The location of any element is determined by the position of its geometric center. Referring to Figure 6, the coordinates of the center of these elements relative to the blade center-of-mass are:

Face Elements: $c = c_i; z = z_i$

Section Elements: $c = c_i; z = l_k$ where $k = 1$ or 2 . For tip section, $k = 1$ and $l_1 = \bar{l}$ and for the base section, $k = 2$ and $l_2 = (\bar{l} - L)$.

Edge Elements: $c = c_m; z = z_j$, where for the leading edge (LE), $m = 1$ and $c_1 = \bar{C}$ and for the trailing edge (TE), $m = 2$ and $c_2 = (\bar{C} - L_c)$.

The coordinates of the element centers relative to the x and y axes are:

Face Elements: $\bar{x}_{ij} = M = x + c_i \cos \phi \cos \theta + z_j \sin \theta$

$\bar{y}_{ij} = N = g - y - c_i \cos \phi \sin \theta + z_j \cos \theta$

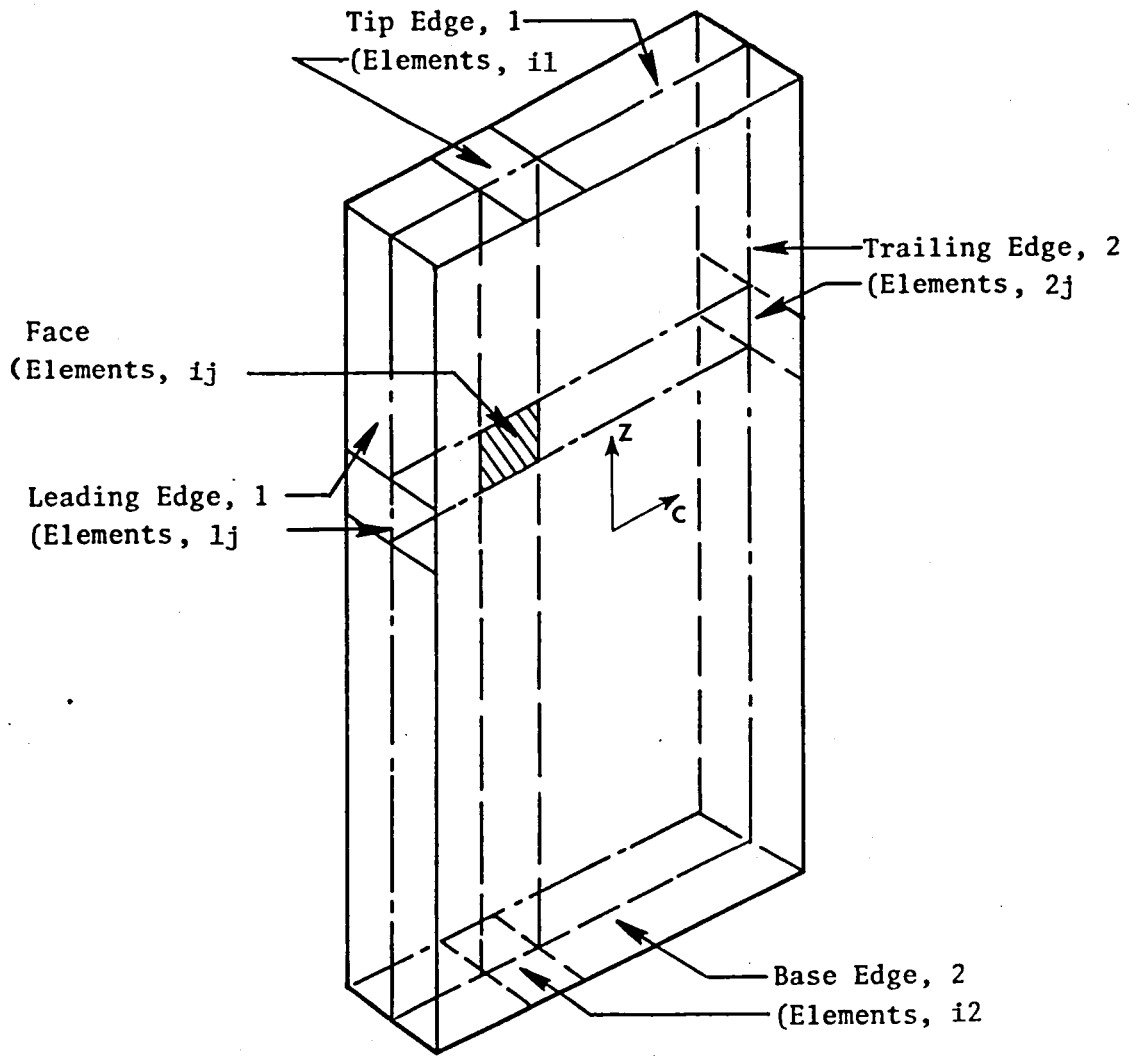


Figure 6. Blade Fragment Model.

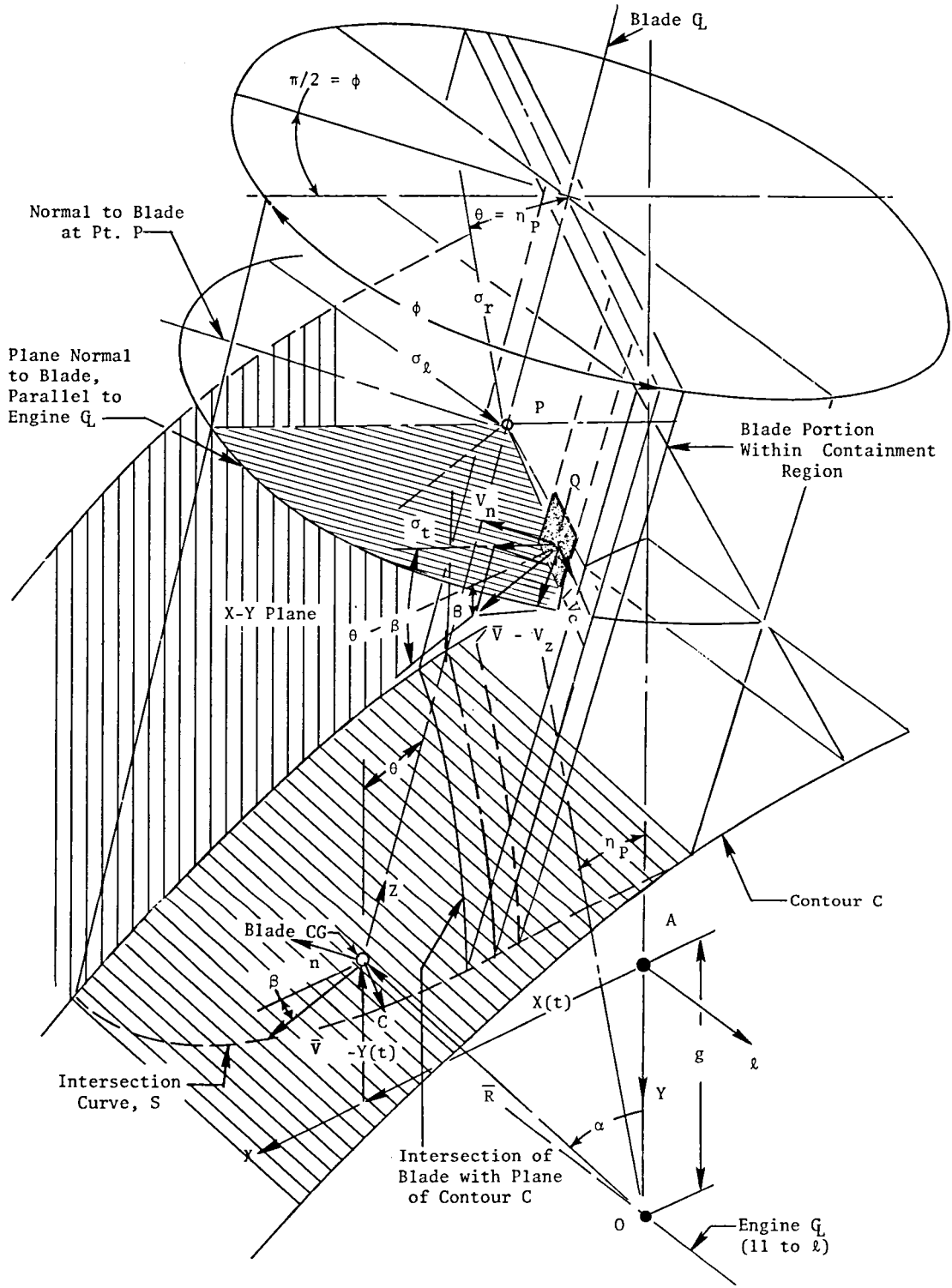


Figure 7. Geometry of Analytical Containment Model.

Section Elements: $\bar{x}_{ik} = P = x + c_i \cos \phi \cos \theta + l_k \sin \theta$

$$\bar{y}_{ik} = Q = g - y - c_i \cos \phi \sin \theta + l_k \cos \theta$$

Edge Elements: $\bar{x}_{jm} = S = x + c_m \cos \phi \cos \theta + z_j \sin \theta$

$$\bar{y}_{jm} = T = g - y - c_m \cos \phi \sin \theta + z_j \cos \theta$$

The angular positions of the element centers relative to the x, y axes are determined by the angles η , which, for the face, section, and edge elements, are, respectively:

$$\eta_{ij} = \tan^{-1} \frac{M}{N}; \quad \eta_{ik} = \tan^{-1} \frac{P}{Q}; \quad \eta_{jm} = \tan^{-1} \frac{S}{T}$$

The radial distances to these same element centers are:

$$R_{ij} = \sqrt{M^2 + N^2}; \quad R_{ik} = \sqrt{P^2 + Q^2}; \quad R_{jm} = \sqrt{S^2 + T^2}$$

The criterion for an element's being within a specific region, n, of the containment structure is:

$$R_{n0} < R_e < R_{ni}$$

where R_e is the element radial distance and R_{n0} , and R_{ni} are the bounding radii of element n, as shown in Figure 5. Similarly, the criterion for an element being outside of the containment structure is:

$$R_0 < R_e < R,$$

where R_0 and R are the boundary radii of the total containment structure.

The criterion for element "engagement" with the containment structure is based on the normal velocity of the element center. These velocities for the various elements are:

Face Elements: $V_{nij} = \bar{V} \cos(\theta - \beta) \sin \phi + z_j \dot{\theta} \sin \phi - c_i \dot{\phi}$ (1)

Section Elements: $V_{zji} = \bar{V} \sin(\theta - \beta) - c_i \dot{\theta} \cos \phi$ (2)

Edge Elements: $V_{cj} = \bar{V} \cos(\theta - \beta) \cos \phi + z_j \dot{\theta} \cos \phi$ (3)

The subscripts n, z, and c refer to the blade axes shown in Figure 6 and the velocity components in Figure 7. The positive z and c axes point toward the tip section and LE, respectively. The positive n axis is determined by applying a right-hand rule to an acute rotation of the positive c axis toward the positive z axis. \bar{V} is the velocity of the blade center of mass:

$$\bar{v} = \sqrt{\dot{x}^2 + \dot{y}^2}, \quad (4)$$

where \dot{x} and \dot{y} are the corresponding velocity components, and β the angle between \bar{v} and the positive x axis:

$$\beta = \tan^{-1}\left(\frac{\dot{y}}{\dot{x}}\right) \quad (5)$$

$\dot{\theta}$ and $\dot{\phi}$ are the angular velocities of the blade about the normal to the x, y plane and the blade airfoil stacking axis, respectively.

The local engagement forces are considered to act normal to the plane of the individual blade element. Their magnitudes are:

Face Elements:

$$A_{ij} = (\Delta c) (\Delta z) [\sigma_t \sin^2 \phi \cos^2(\theta - \eta_{ij}) + \sigma_r \sin^2 \phi \sin^2(\theta - \eta_{ij}) + \sigma_\ell \cos^2 \phi] \quad (6)$$

Section Elements:

$$B_{ik} = (\Delta c) h [\sigma_t \sin^2(\theta - \eta_k) + \sigma_r \cos^2(\theta - \eta_{lk})] \quad (7)$$

Edge Elements

$$C_{jm} = h (\Delta z) [\sigma_t \cos^2 \phi \cos^2(\theta - \eta_{jm}) + \sigma_r \cos^2 \phi \sin^2(\theta - \eta_{jm}) + \sigma_i \sin^2 \phi \cos^2(\theta - \eta_{jm})] \quad (8)$$

The friction forces associated with these normal forces are:

$$A_{\mu_{ij}} = (\Delta c) (\Delta z) [\mu_t \sigma_t \sin^2 \phi \cos^2(\theta - \eta_{ij}) + \mu_r \sigma_r \sin^2 \phi \sin^2(\theta - \eta_{ij}) + \mu_\ell \sigma_\ell \cos^2 \phi] \quad (9)$$

$$B_{\mu_{iR}} = (\Delta c) h [\mu_t \sigma_t \sin^2(\theta - \eta_{ik}) + \mu_r \sigma_r \cos^2(\theta - \eta_{ik})] \quad (10)$$

$$c_{\mu_{jm}} = h (\Delta z) [\mu_t \sigma_t \cos^2 \phi \cos^2 (\theta - \eta_{jm}) + \mu_r \sigma_r \cos^2 \phi \sin^2 (\theta - \eta_{jm}) + \mu_\ell \sigma_\ell \sin^2 \phi \cos^2 (\theta - \eta_{jm})] \quad (11)$$

The forces are computed for each blade element whose center is within the containment structure. The normal forces may or may not act on the element, however, and their particular mode of action is dependent on the local normal velocity of the element center, namely $v_{n_{ij}}$, V_{z_i} , and V_{c_j} of the face, section, and edge elements, respectively. If the velocity is zero, the force is not considered to act on the element. If the particular velocity component is in the positive direction, the force will be positive for face, tip, and leading edge elements, and zero for base trailing edge elements. If the velocity component is in the reactive direction, the force will be negative for face, base, and trailing edge elements, and zero for tip and face, base, and trailing edge elements, and zero for tip and leading edge elements.

Friction force will act on an element only when the corresponding normal force is not equal to 0. Friction force will act in a direction opposite to that of the corresponding velocity component.

The normal friction forces are summed to determine the total forces acting on the blade in the n, Z, and C directions. These are:

$$F_n = \sum_{ij} A_{ij} + \sum_{ik} B_{\mu_{ik}} + \sum_{jm} C_{\mu_{jm}} \quad (12)$$

$$F_z = \sum_{ij} A_{\mu_{ij}} + \sum_{ik} B_{ik} + \sum_{jm} C_{\mu_{jm}} \quad (13)$$

$$F_c = \sum_{ij} A_{\mu_{ij}} + \sum_{ik} B_{\mu_{ik}} + \sum_{jm} C_{jm} \quad (14)$$

These forces are resolved relative to the x and y axes into the following components:

$$F_x = F_n \sin \phi \cos \theta + F_z \sin \theta + F_c \cos \phi \cos \theta \quad (15)$$

$$F_y = F_n \sin \phi \sin \theta - F_z \cos \theta + F_c \cos \phi \sin \theta \quad (16)$$

The torques due to the normal and friction forces relative to the blade center-of-mass and the ℓ and z axes are:

$$T_\theta = \sin \phi \left[\sum_{ij} A_{ij} z_j + \sum_{ik} B_{\mu_{ik}} \ell_k + \sum_{jm} C_{\mu_{jm}} z_j \right] + \cos \phi \left[\sum_{ij} A_{\mu_{ij}} c_i - \sum_{ik} B_{ik} c_i - \sum_{jm} C_{\mu_{jm}} c_m \right] + \sum_{ij} A_{\mu_{ij}} z_j + \sum_{ik} B_{\mu_{ik}} \ell_k + \sum_{jm} C_{jm} z_j \quad (17)$$

$$T_{\phi} = \sum_{ij} A_{ij} c_j + \sum_{ik} B_{ik} c_i + \sum_{jm} C_{jm} c_m \quad (18)$$

The equations of motion for the blade are:

$$\ddot{x} = -\frac{F_x}{M} \text{ and } \ddot{y} = -\frac{F_y}{M} \quad (19)$$

where M is the blade mass, and

$$\ddot{\theta} = -\frac{T_{\theta}}{J_{\ell}} \text{ and } \ddot{\phi} = \frac{T_{\phi}}{J_z} \quad (20)$$

where $J_{\ell} = J_c \sin^2 \phi + J_n \cos^2 \phi - 2J_{cn} \cos \phi \sin \phi$. J_{ℓ} , J_c , J_n , and J_{cn} are the mass moments of inertia of the blade about the respective axes and through the center-of-mass.

The computer program processing of the analysis begins with the initial conditions:

$$x_0, y_0, \theta_0, \phi_0, \dot{x}_0, \dot{y}_0, \dot{\theta}_0, \text{ and } \dot{\phi}_0$$

and calculates the position and velocities of all blade fragment elements relative to the containment structure ring sections. It then applies the velocity criteria and computes the normal forces (Equations 6, 7, and 8) and friction forces (Equations 9, 10, and 11). Next, it sums these to obtain the total forces F_n , F_z , F_c , F_x and F_y and the torques T_{θ} and T_{ϕ} . These apply to the positions at the beginning of each time increment. Next, the equations of motion are integrated and the positions and velocities of the blade fragment determined at a time corresponding to the end of the time interval. This process is repeated for a specified number of time intervals.

The program prints out the following output data for each time interval:

1. Position radii R_{ik} and n_{ik} of all tip and base section elements.
2. Blade fragment position coordinates, x , y , θ , and ϕ ; velocities, \dot{x} , \dot{y} , \bar{V} , $\dot{\theta}$ and $\dot{\phi}$; and the angle β of the velocity \bar{V} relative to the x , y axes.
3. Total kinetic energy, linear momentum, and angular momentum of the blade fragment.
4. Total forces F_n , F_z , F_c , F_x , and F_y and torques T_{θ} and T_{ϕ} .
5. Forces on all individual elements for selected values of time.

The relationship of this type of analytical approach to the actual containment process is shown in Section 4.5.1.

4.2 TASK II - BLADE IMPACT PENETRATION TESTS

The objective of this task was to design and evaluate several containment concepts which, based on the analysis presented in Section 4.1, seemed to provide some advantages over current practice. To evaluate these concepts, several methods were considered. Small-scale pure ballistic tests were not felt to be sufficiently representative of the blade containment process. Rotating tests using actual blades are expensive when a large number of tests must be run. Therefore, the method chosen for this task was the gas gun containment simulation test method. This method (Reference 1) utilizes simulated blade projectiles as the impacting projectiles and provides a reasonable method of qualitatively evaluating different containment concepts quickly and at moderate cost.

4.2.1 Containment Scaling Basis

The basis for relating gas gun and rotating rig test data to large turbofan containment behavior was two fold; namely, (a) scaling relations developed in previous containment research (Reference 1) and (b) a general analysis of the containment process.

Scaling Relations

Assuming the orderly type process discussed previously that is associated with well-designed containment structures, a set of applicable scaling relations can be defined (Reference 1). These relations, which are given in Table I, do not include consideration of blade/blade processes because these interactions are likely to be relatively minor for such processes.

The scaling relations refer the behavior of a containment structure/blade fragment model (subscript m) whose linear dimensions are smaller than a prototype (subscript p) by a scale factor S. They are based on the assumption that the initial linear velocity of the blade fragment is identical in both model and prototype and that the model and prototype are geometrically similar. Another assumption is that the initial blade fragment position and orientation relative to the containment structure are identical in both model and prototype.

If these conditions are maintained between the model and prototype, as they would be in a rotating test of an exact scaled replica of the prototype, then the observed containment behavior will be similar to that of the full scale test. In the gas gun containment test, however, it is difficult to simulate the initial rotational speed ($\dot{\theta}_0$) of the prototype, namely $\theta_{0m} = S\theta_{0p}$. While this is not important from an initial kinetic energy standpoint

Table I. Scaling Relationships.

<u>Quantity(1)</u>	<u>Scaling Relation</u>
Linear Dimensions	$\frac{L_m}{L_p} = \frac{c_m}{c_p} = \frac{h_m}{h_p} = \frac{w_m}{w_p} = \frac{R_m}{R_p} = \frac{1}{S}$
Mass	$\frac{M_m}{M_p} = \frac{1}{S^3}$
Kinetic Energy	$\frac{KE_m}{KE_p} = \frac{1}{S^3}$
Blade Mass Moment of Inertia	$\left(\frac{I_m}{I_p}\right)_M = \frac{1}{S^5}$
Plane Moment of Inertia	$\left(\frac{I_m}{I_p}\right)_A = \frac{1}{S^4}$
Displacement	$\frac{x_m}{x_p} = \frac{1}{S}$
Blade Velocity	$\frac{V_m}{V_p} = 1$
Acceleration	$\frac{\ddot{x}_m}{\ddot{x}_p} = S$
Angular Position(2)	$\theta_m/\theta_p = \phi_m/\phi_p = 1$
Angular Velocity(2)	$\dot{\theta}_m/\dot{\theta}_p = \dot{\phi}_m/\dot{\phi}_p = S$
Angular Acceleration	$\ddot{\theta}_m/\ddot{\theta}_p = \ddot{\phi}_m/\ddot{\phi}_p = S^2$

Table I. Scaling Relationships (Concluded).

<u>Quantity</u>	<u>Scaling Relation</u>
Time	$t_m/t_p = \frac{1}{S}$
Containment Resistance	$\sigma_m/\sigma_p = 1$
Bending Moment	$H_m/H_p = \frac{1}{S^3}$
Bending Stress	$\frac{\sigma_m}{\sigma_p} = 1$
Bending Deflection	$\frac{\delta_m}{\delta_p} = \frac{1}{S}$
Energy Index	$I_{E_m}/I_{E_p} = 1$

- (1) Applies to blade fragment and containment structure unless noted otherwise.
- (2) Caused by containment forces acting on the blade fragment.

(for example, the rotational energy of a CF6 fan blade is -6% of its total kinetic energy), the nonsimulation of the angular position θ_m can be significant. This shortcoming, however, can be compensated rather easily in the gas gun test.

Correlation by Containment Analysis

An analysis of the containment process provides another means of relating subscale test results to full scale behavior. The analysis, described previously in this report, permits applying containment data obtained from subscale tests (gas gun and rotating types) directly to predicting full scale prototype behavior. Presently, the analysis has been applied to extract design data from gas gun tests. When fully developed to account for more realistic blade geometry and other effects, it is anticipated that the analysis will form the basis for a design procedure for containment systems. Such a practice should reduce the dependency on scaled testing and expedite the development of improved systems.

4.2.2 Comparison of Ballistic and Rotating Test Techniques

The Gas Gun Development Simulation Test method is based on the scaling relations previously shown in Table 1. It utilizes a blade fragment and containment structure that have close geometrical similarity and material identity to the full scale prototype. The method utilizes a semicircular containment structure, although it is possible to use one which corresponds to a smaller or larger arc. Ideally, the method should employ blade fragments that are exact scaled replicas of the prototype; but since such replicas are not usually available, approximate blade models are employed. These models, however, are accurately scaled with respect to length, width, mass and mass moment-of-inertia.

In the gas gun method, the blade is linearly accelerated to the desired test velocity by means of a gas gun.

The initial conditions of the blade are:

$$x = y = 0; \theta = 0, \phi = \phi_S$$

$$\dot{x} = \bar{V}_0 = \omega \bar{R}; \dot{y} = 0, \dot{\theta} = 0, \dot{\phi} = 0$$

where x and y are displacement coordinates of the blade center-of-gravity relative to fixed x (vertical) and y (horizontal) coordinate axis. The origin of the x, y axis is coincident with the position of the blade c.g., at the instant of release; \bar{R} is the distance between the blade c.g. and axis of rotation; θ is the angular position of the blade stacking axis in the x, y plane and relative to the y axis; ϕ is the angle between the tip chord axis and the x, y plane; ϕ_S is equal to the initial tip stagger angle; the dots indicate velocity.

In the rotating method, the test blade is released by explosive means. The initial conditions of the blade are:

$$x = y = 0, \theta = 0, \phi = \phi_S;$$

$$\dot{x} = \omega \bar{R}, \dot{y} = 0, \dot{\theta} = \omega, \dot{\phi} = 0$$

Hence, the initial conditions of the "released" blade are identical in both test methods with the sole exception of θ . The nonsimulation of this quantity in the gas gun test method results in (1) a slightly lower (-6%) initial kinetic energy, which can be compensated by a slight increase in \bar{V}_0 and (2) a kinematic effect which can be largely compensated by using an initial $\theta = \theta_0$ rather than $\theta = 0$. Therefore, an initial angle, $\theta_0 = -76.7^\circ$ was employed. This angle is similar to the blade strike attitude during the more violent phase of the containment interaction. Use of such an initial angle did, however, result in a more severe test evaluation, one producing a lower penetration threshold velocity. The subsequent motion of the blade and its interaction with the containment structure follow directly from the blade initial conditions.

An important feature of the containment process that is not simulated by the gas gun test method is the action of rotor blades with the blade projectile. Simulation of such interactions, however, is considered relatively unimportant to the initial containment process for tests involving structures that have good nesting and retaining qualities. The rotating tests, of course, also feature other rotor blades which can interact with the released blade.

Based on the above comparison of gas gun (ballistic) tests versus rotation tests, it was felt that the combination of gas gun testing to screen a number of concepts combined with the rotating tests of the most promising configuration provides an efficient and cost effective means to develop improved containment systems.

4.2.3 Test Method Description

The gas gun containment facility, shown in Figure 8, consists of a blade accelerator section, a sabot deceleration section, and a totally enclosed impact chamber. The accelerator section is made up of a gas driver vessel and a smooth bore barrel having a length of 5.49 m (18 ft) and bore diameter of 0.10 m (4 in.). The decelerator is a heavy steel tube assembly and is shown attached to the left of the gun barrel. The impact chamber consists of an adjustable apparatus for mounting the containment structure and a protective housing approximately 0.91 x 0.91 x 0.30 m (3 x 3 x 1 ft) and is shown in the left half of Figure 8.

The technique utilizes a semicircular containment structure segment. Figure 9 shows a close-up of a mounted structure and the impact chamber.

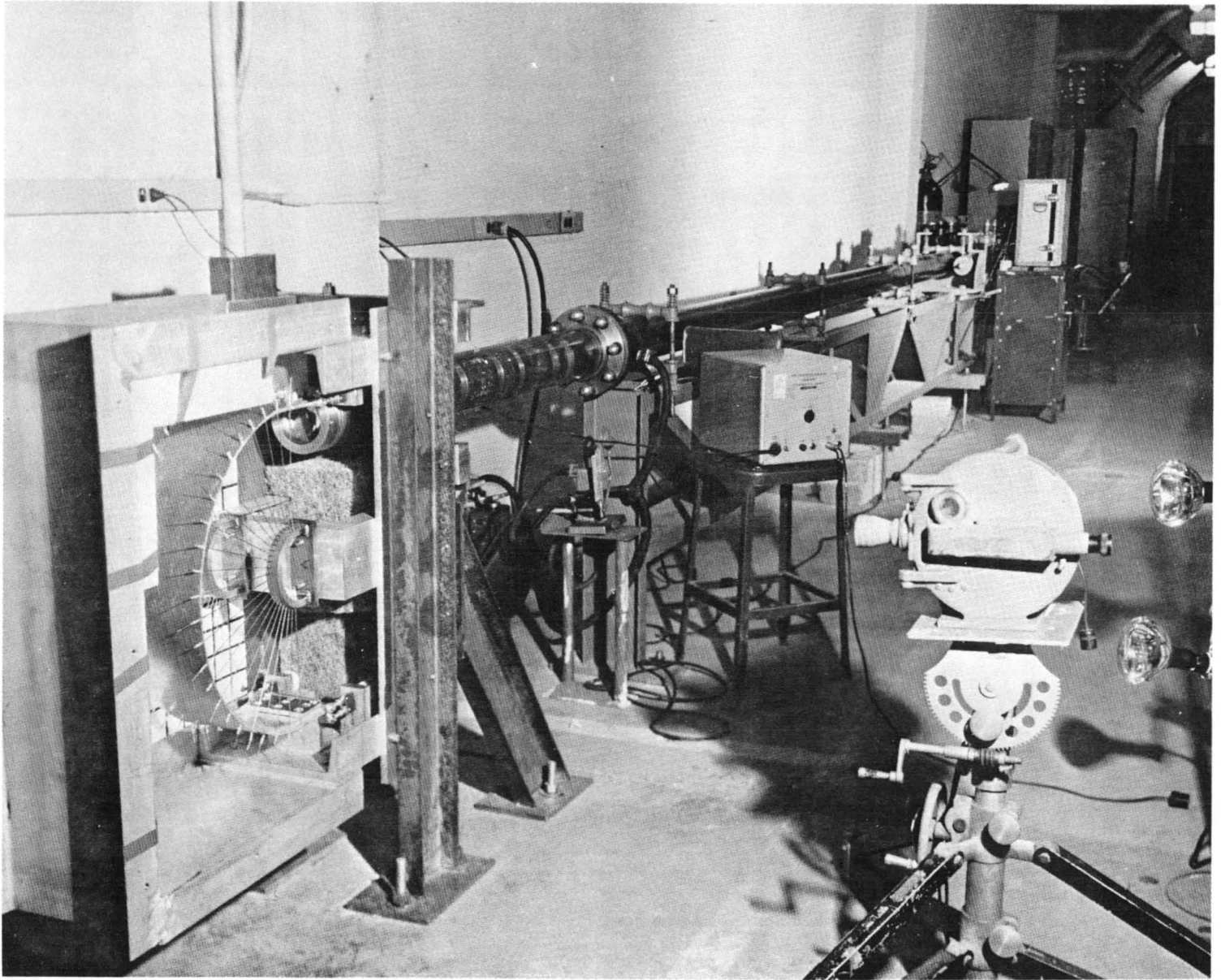


Figure 8. Gas Gun Containment Test Facility.

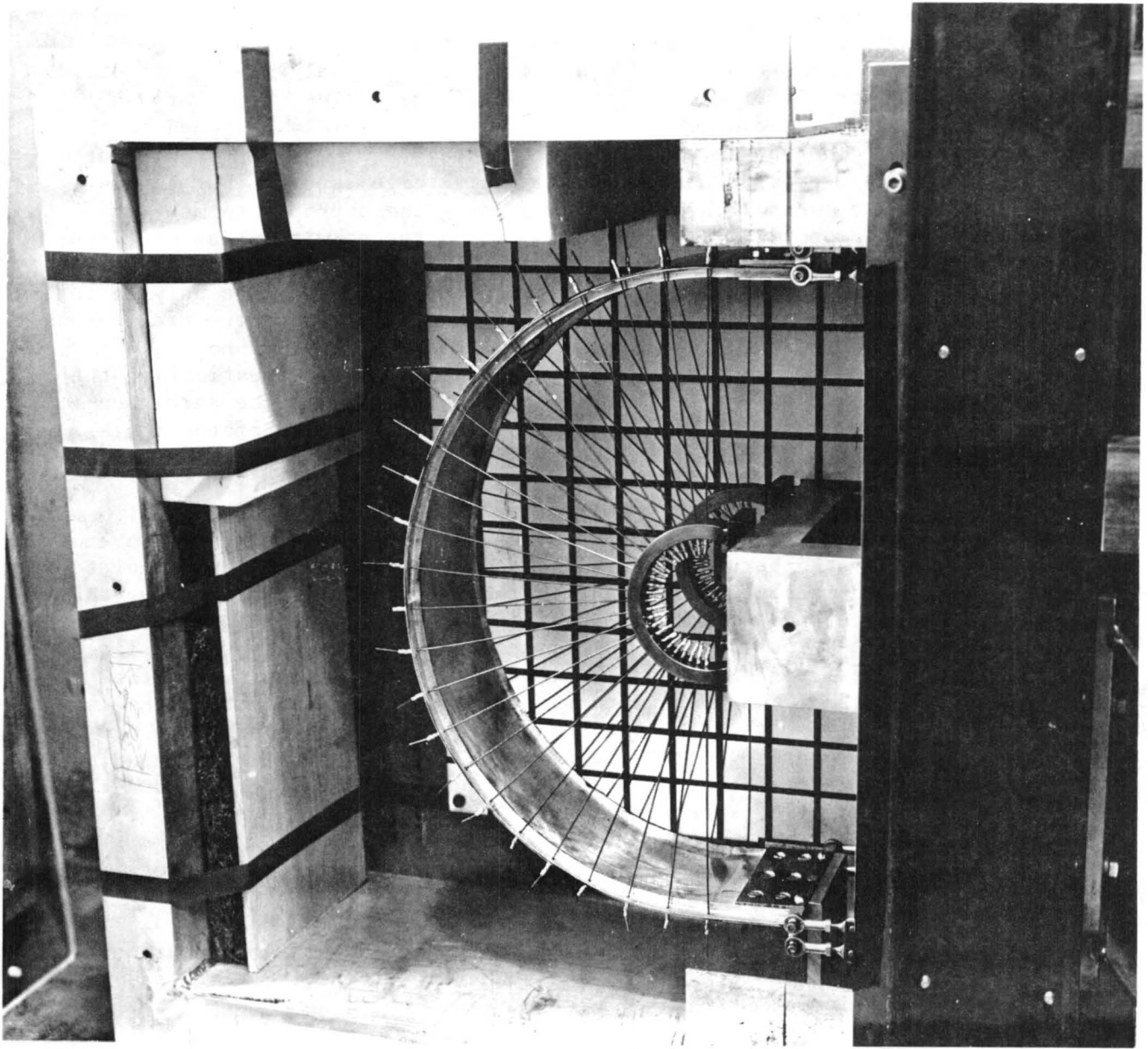


Figure 9. Containment Structure Segment.

The structure is supported in the test frame in two distinct ways which attempt to simulate the effect of casing restraint on the containment structure. First, it is supported by two equal sets of 24 radial wires, or spokes, which are attached to the ring along its lateral edges. The spokes are secured at the inner end to a heavy steel ring which is rigidly fastened to the ring support beam. The spokes, spaced approximately 0.02 m (1 in.) apart at the containment ring, provide a distributed radial edge support that can be varied easily to any desired value simply by using the appropriate material and diameter for the spokes. The ring also can be tested without spokes; and, as a result, casing support ranging from zero to any practical value can be simulated. This simulation, of course, is only approximate, since only radial support is provided whereas in the actual case axial and circumferential forces and moments also are present. The system used, however, enables positive definition of magnitude of casing support and provides a means of estimating the amount of strain energy associated with the casing response. The strain energy can be estimated merely by measuring the change of length of the spoke resulting from the test and entering the tensile load deflection curve for the spokes at the measured value of deflection.

The second type of support is provided by reaction forces at the two ends of the ring. Shock absorbers and inertial mass attached to each end simulate the effect of casing forces associated with the missing half of the ring, that is, opposite to where blade impact is occurring; and only their integrated (rather than detailed) local effect is of importance. The end reaction forces due to structural resistance are each set equal to one-half the sum of the horizontal components of the spoke forces. This is done by selecting the proper shock absorption material. The shock absorber was designed to use a plastic foam as the absorbing medium. Polyurethane foam actually was used, since it provides a fairly constant resistance over large deflections and can be obtained in a variety of strengths.

The gas gun facility provides the following features for blade containment testing:

1. Control of blade impact conditions such as: angular orientation relative to the pitch, roll, and yaw axes, strike location, and initial velocity.
2. Large range of impact velocity, up to 304.8 m/sec (1000 ft/sec).
3. Accommodation of a variety of blade projectile masses and shapes and containment structure sizes.
4. Clean test environment due to absence of debris and gas discharge. This results in clear, readable, high-speed photographic records of the test from start to finish.
5. Close-up and well-aligned viewing of the test events which results in accurate data extraction.
6. Easy assembly and disassembly of test specimens.

The gas gun facility utilizes a Fastax high-speed motion camera for photographic coverage of the containment process events. The camera provides a maximum framing rate of 16,000 frames/sec. The camera is pointed in a direction normal to the x, y plane, which represents the fan rotational plane. The photographic aim center is situated close to the blade path in order to permit accurate measurement of blade motions. The blade motion appears relative to a square background grid which facilitates data acquisition from the photographs. This grid is clearly visible in Figure 9.

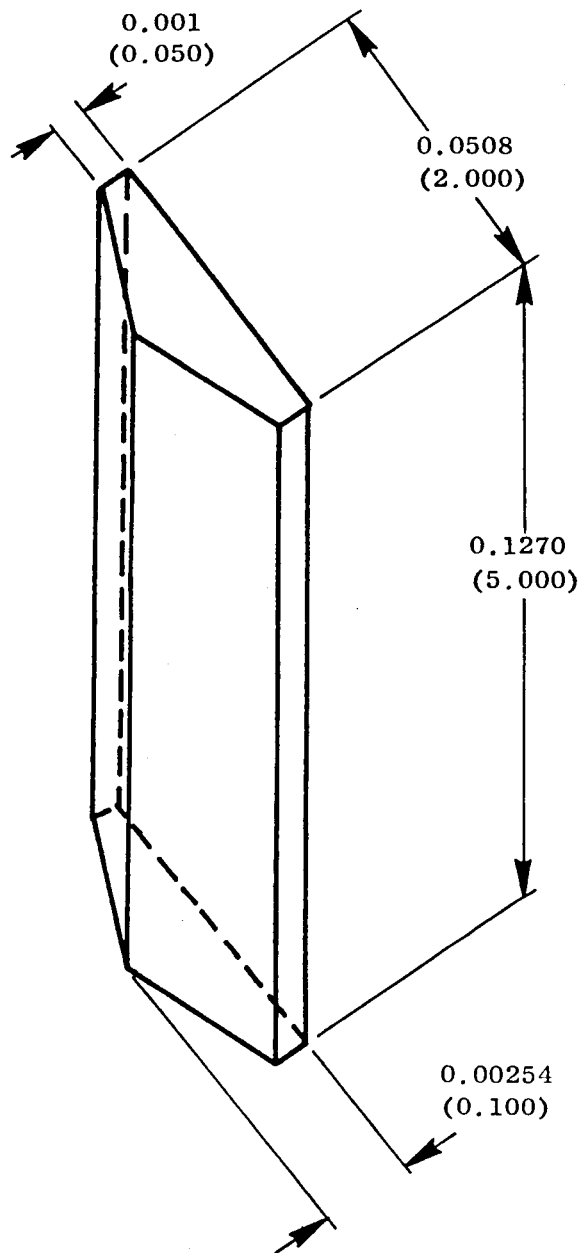
4.2.4 Projectile Description

The projectiles used in this task were designed to simulate a fragment of an actual blade. They were 0.051 by 0.13 m (2.0 by 5.0 in.) in planform and were tapered in thickness from 0.01 m (0.05 in.) on the long edges to 2.5×10^{-3} m (0.10 in.) in the center. Two types of these projectiles were used. To represent a fragment on an existing titanium blade, the all-titanium projectile shown in Figure 10 was used. This projectile weighed 0.06 kg (0.128 lb). Originally, two composite projectile configurations were also to be used - one of all graphite/epoxy construction and the other representing a superhybrid design. Since at the time that the projectile design was finalized, the superhybrid concept seemed to be the one more likely to see near-term service. This was the only type of projectile fabricated for use in this program. The projectile used to simulate the superhybrid type of construction is shown in Figure 11. Titanium foil was used in place of boron/aluminum to reduce the fabrication costs of these projectiles. The superhybrid projectiles weighed 0.03 kg (0.0675 lb). These projectiles were mounted on a wooden sabot, as shown in Figure 12, which was then propelled down the gas gun barrel.

4.2.5 Containment Description

Several different containment design concepts were selected for evaluation at the start of the program and were subsequently tested in the gas gun facility. They were designed to meet one or more of the following desirable characteristics:

1. Penetration Resistance - prevention of fragment perforation or fragment pass-through.
2. Nesting - accommodation of fragments to imbed within the cross-sectional volume of the containment structure.
3. Retention - capture and retention of fragments within the containment structure.
4. Tracking Control - constraint of fragments from movement within the lateral confines of the containment structure.
5. Overall Deformation Resistance - preclusion of large, overall deformations that cause twisting and out-of-roundness motions of the containment structure.



• Dimensions: ^m
(in.)

Figure 10. Titanium Projectile.

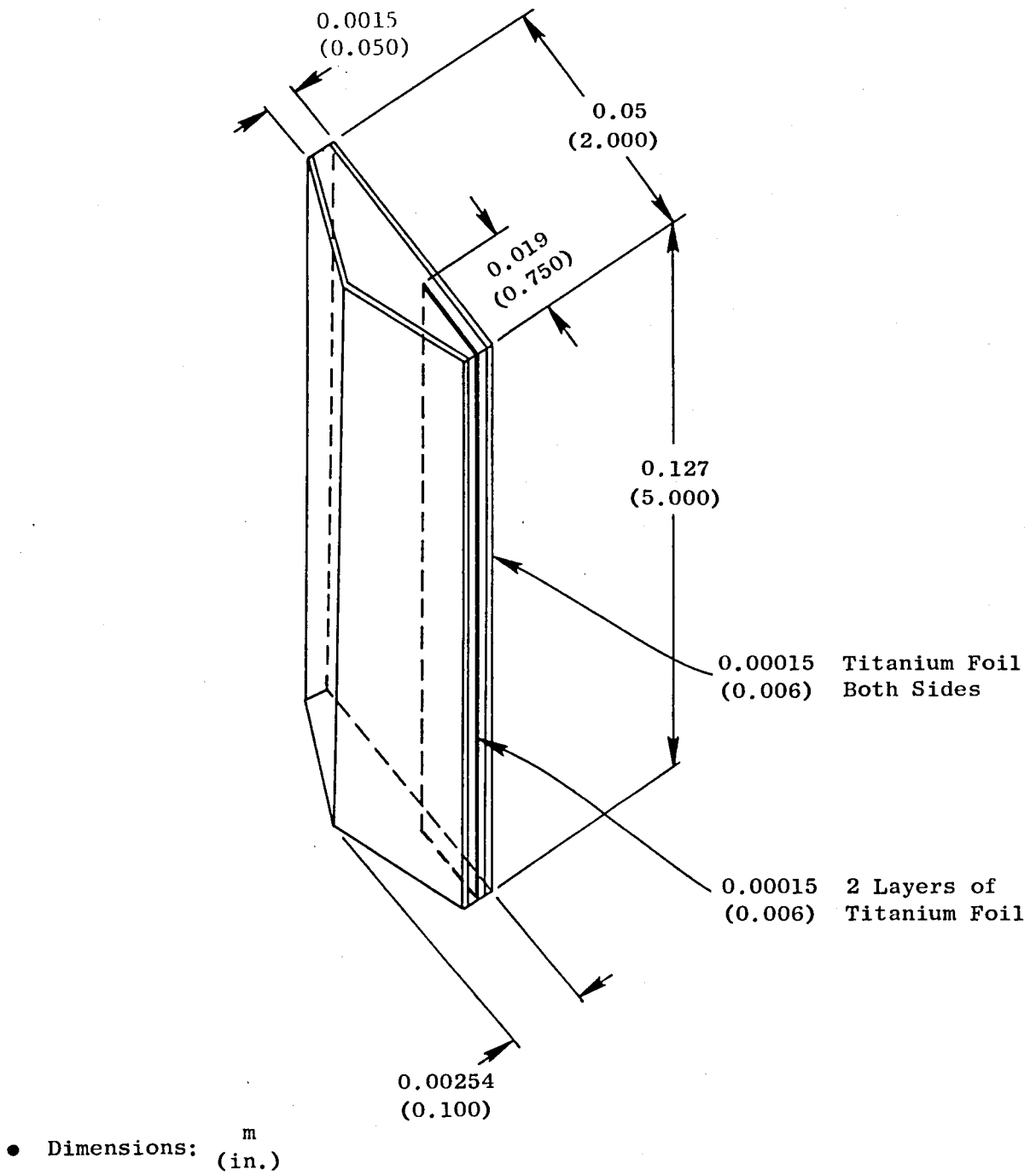


Figure 11. Superhybrid Composite Projectile.

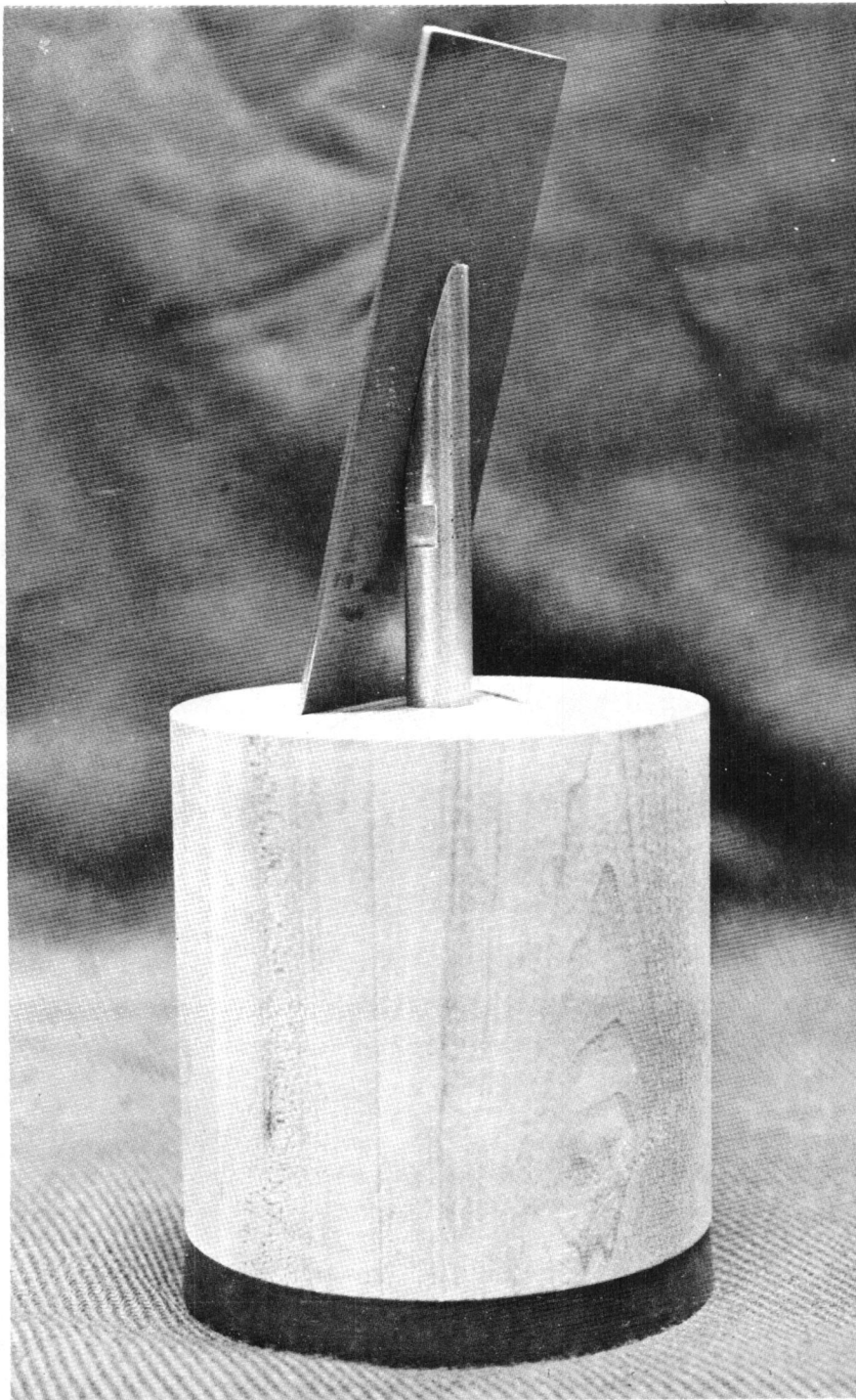


Figure 12. Blade Projectile and Mounting Arrangement on Sabot.

Figure 13 shows various finned-type specimens. These are identical to one another except for the material, thickness, and depth of the fin elements. The backing ring is made of 6061 T-6 aluminum alloy. Figure 13 shows from bottom to top; short-finned Kevlar/epoxy laminate; long-finned Kevlar/epoxy laminate; long-finned 6Al-4V titanium; and long-finned 2024 T-3 aluminum structures. These designs are described in more detail in Figures 14 through 17.

Other concepts are shown in Figure 18. Figure 18A involves a layered assembly consisting of inner and outer walls of 2024 T-3 aluminum with the space between them filled with unimpregnated Kevlar cloth plies. Two other variations of this design were also tested, in which the number of Kevlar plies was varied and a stainless steel inner wall utilized. A detailed view of this configuration is shown in Figure 19.

Figure 18B shows a design that features a thick inner layer of aluminum honeycomb core and a thin aluminum backing ring. The inner layer is constructed of bonded segments of core whose cells are circumferentially oriented. The construction is shown in Figure 20 in more detail.

Finally, a stainless steel (AMS-5514) sheet metal ring, shown in Figure 21, was also tested. This construction represents conventional containment ring practice and was included in the program in order to provide a comparison reference for the various design concepts evaluated.

4.2.6 Test Results

Twenty gas gun tests were performed on 10 different 180°-type containment structures, each of which structures was subjected to two blade fragment impacts. Testing each structure twice is practicable because containment action and resulting damage are almost invariably confined to the initial 90° portion of the structure. The exception is the simple-sheet stainless steel specimens, where the entire surface was traversed by the blade fragment, as is shown in subsequent photographs. Even for these, little significant damage was incurred beyond the initial 90° region; therefore, a valid second test was allowed.

Fifteen of the tests utilized titanium blade projectiles and the remainder superhybrid composite projectiles. Invariably, the titanium projectiles produced much more damage than the superhybrid projectiles at identical initial impact velocities.

High-speed photographs with an average frame rate of over 12,000 frames/sec were obtained for all tests. These permitted observation and measurement of the initial velocity and orientation of the projectile. The results of the tests are summarized in Table II and discussed individually below.

Test 1

This test was the first of four baseline impact tests on state-of-the-art steel containment rings. The containment structure utilized in the test was a stainless steel ring (Type 321) of simple sheet construction having a unit

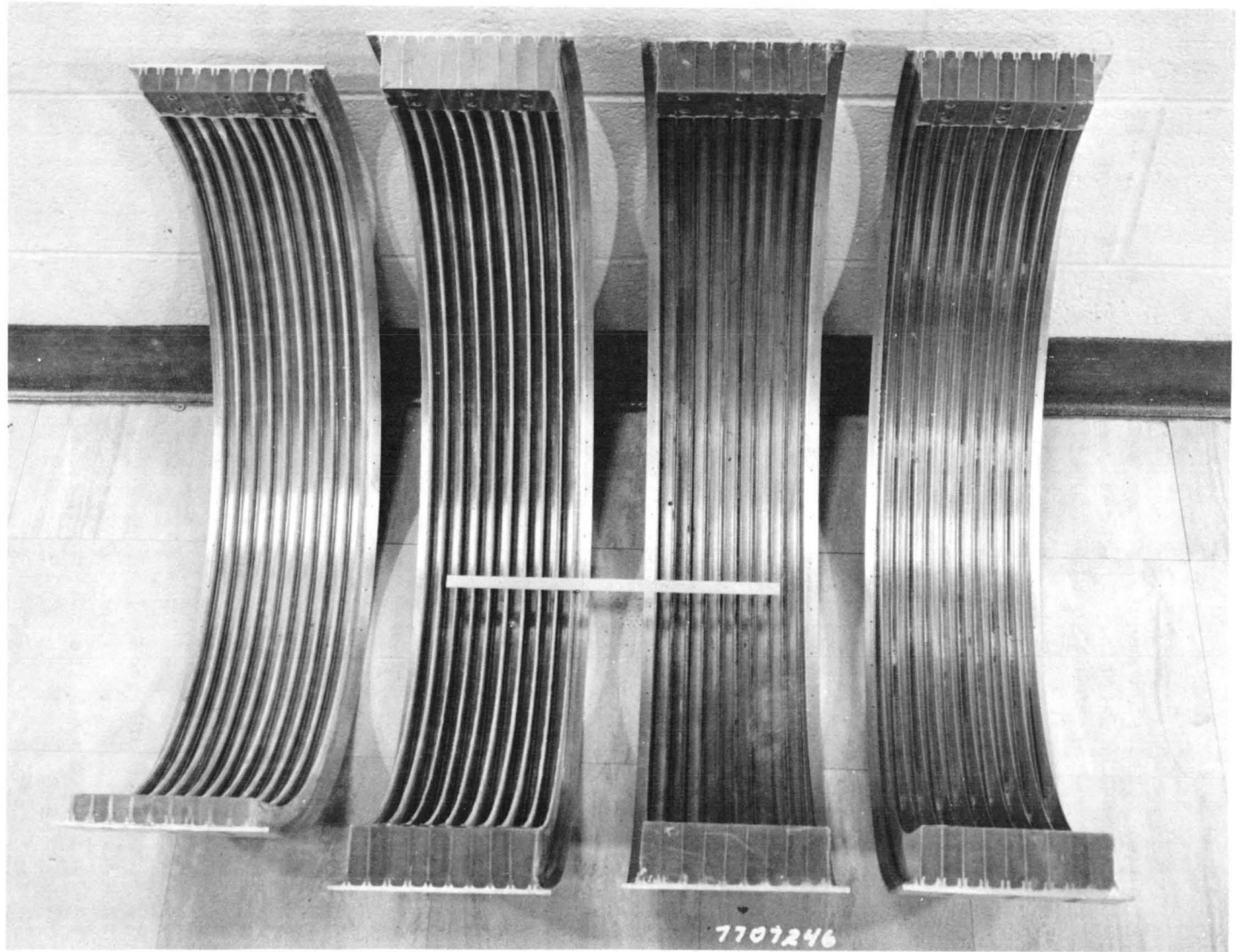
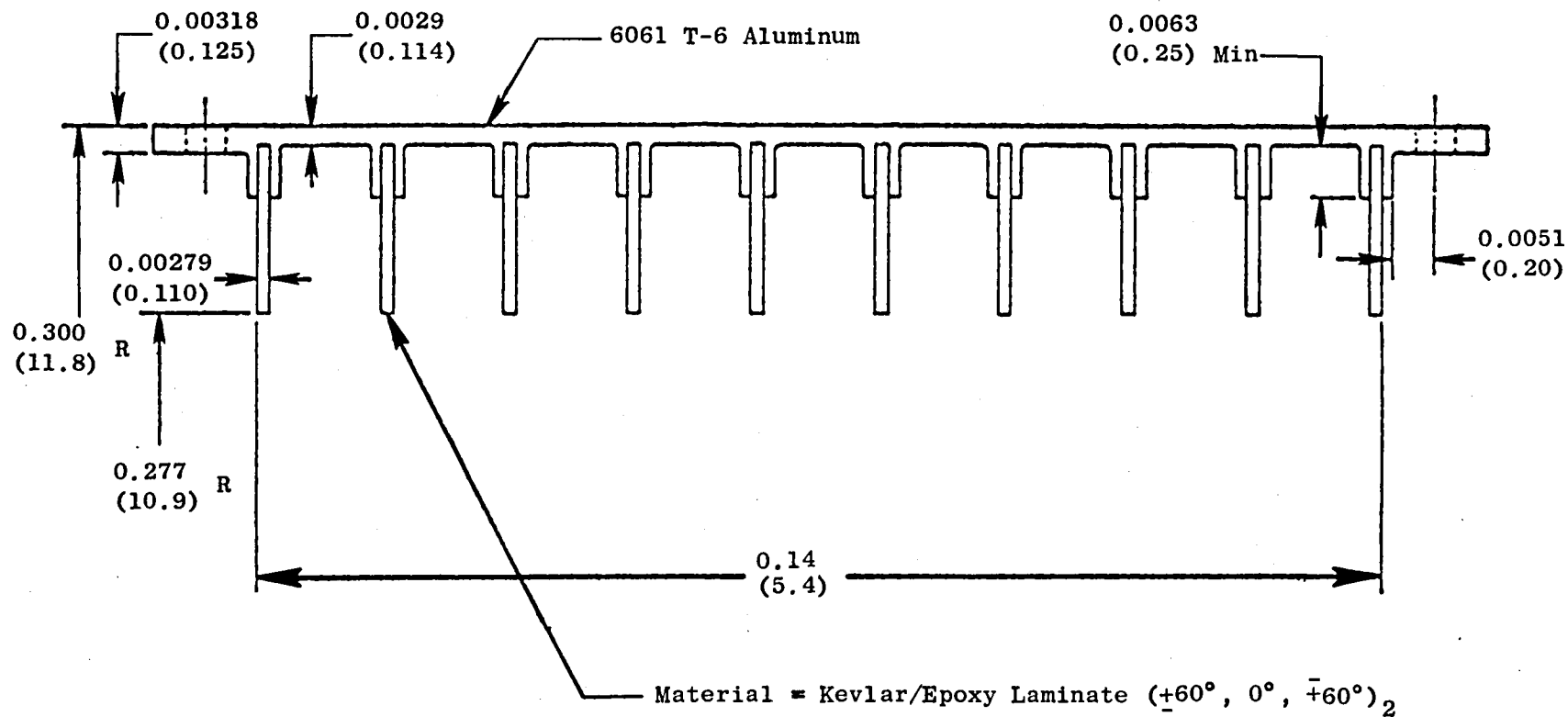
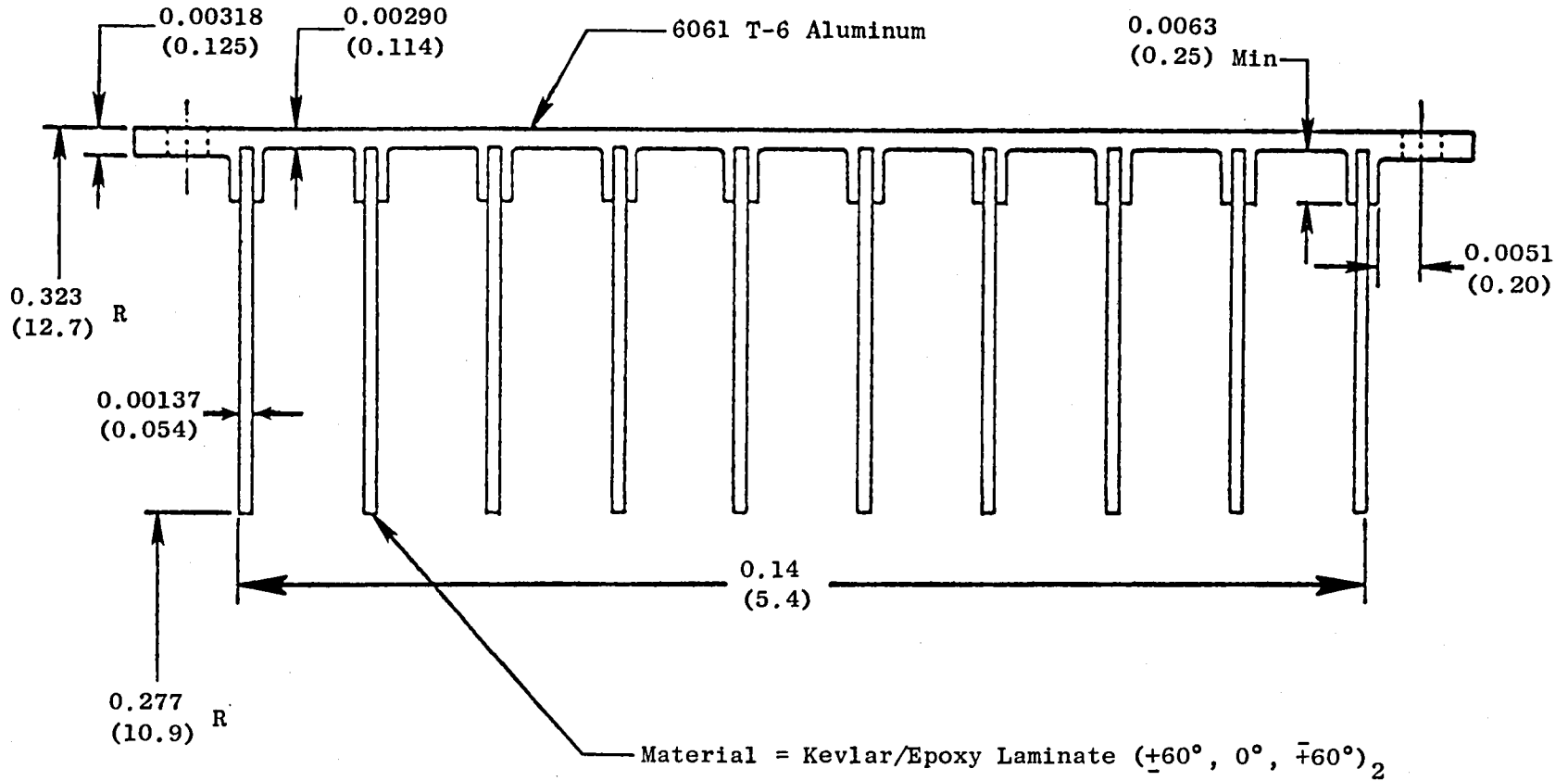


Figure 13. Finned-Type Containment Specimens.



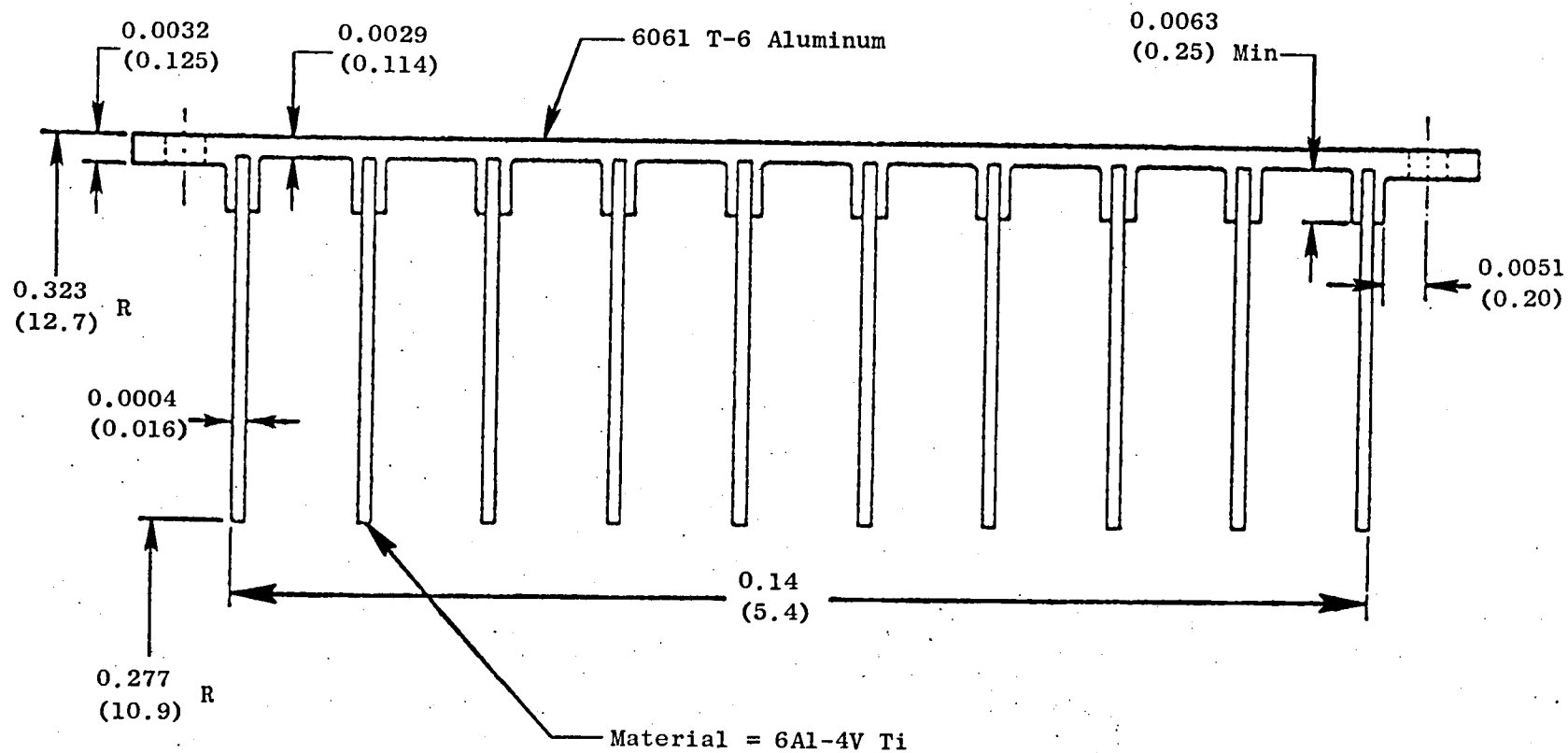
● Dimensions: ^m
(in.)

Figure 14. Short-Finned Kevlar/Epoxy Laminate.



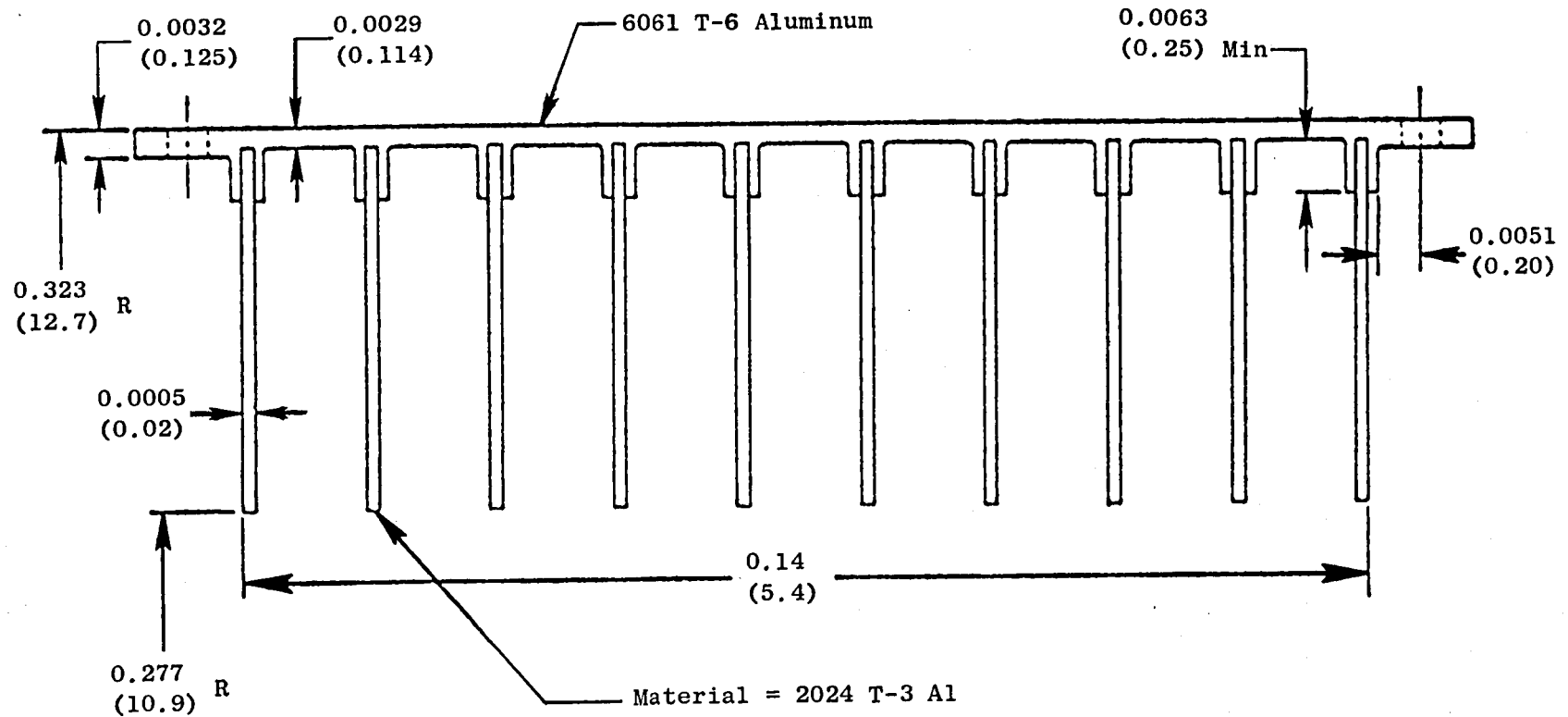
• Dimensions: $\begin{matrix} \text{m} \\ \text{(in.)} \end{matrix}$

Figure 15. Long-Finned Kevlar/Epoxy Laminate.



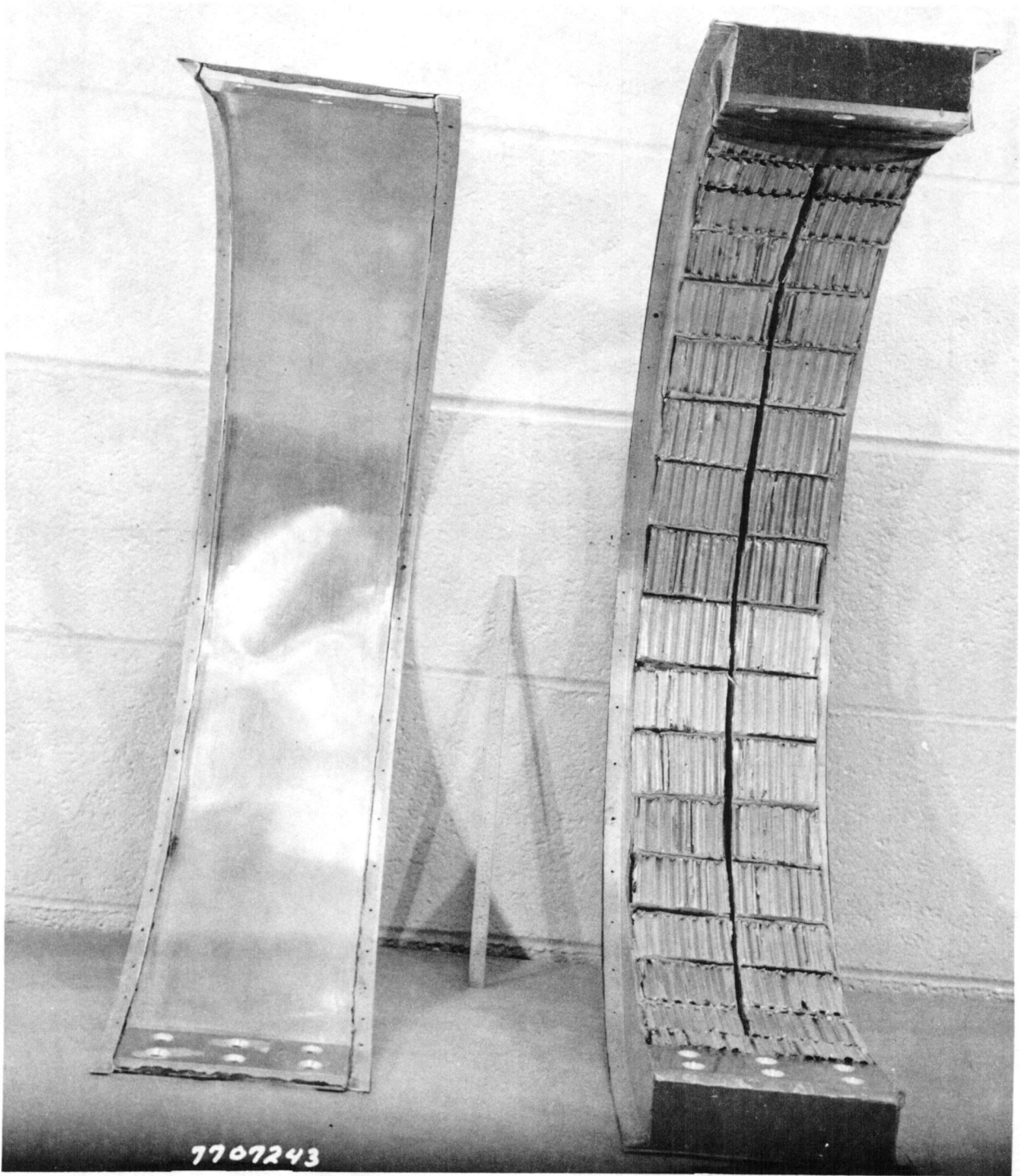
• Dimensions: ^m
(in.)

Figure 16. Long-Finned 6Al-4V Titanium.



• Dimensions: ^m
(in.)

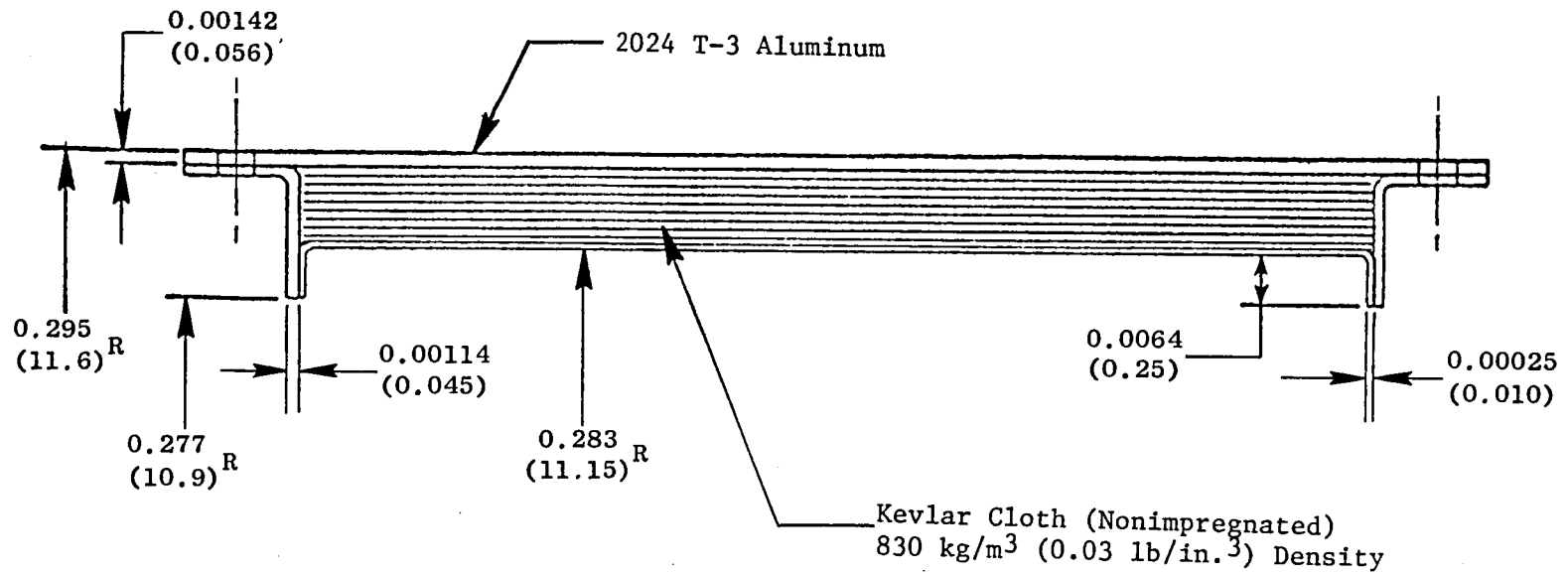
Figure 17. Long-Finned 2024 T-3 Aluminum Structure.



(a) Left

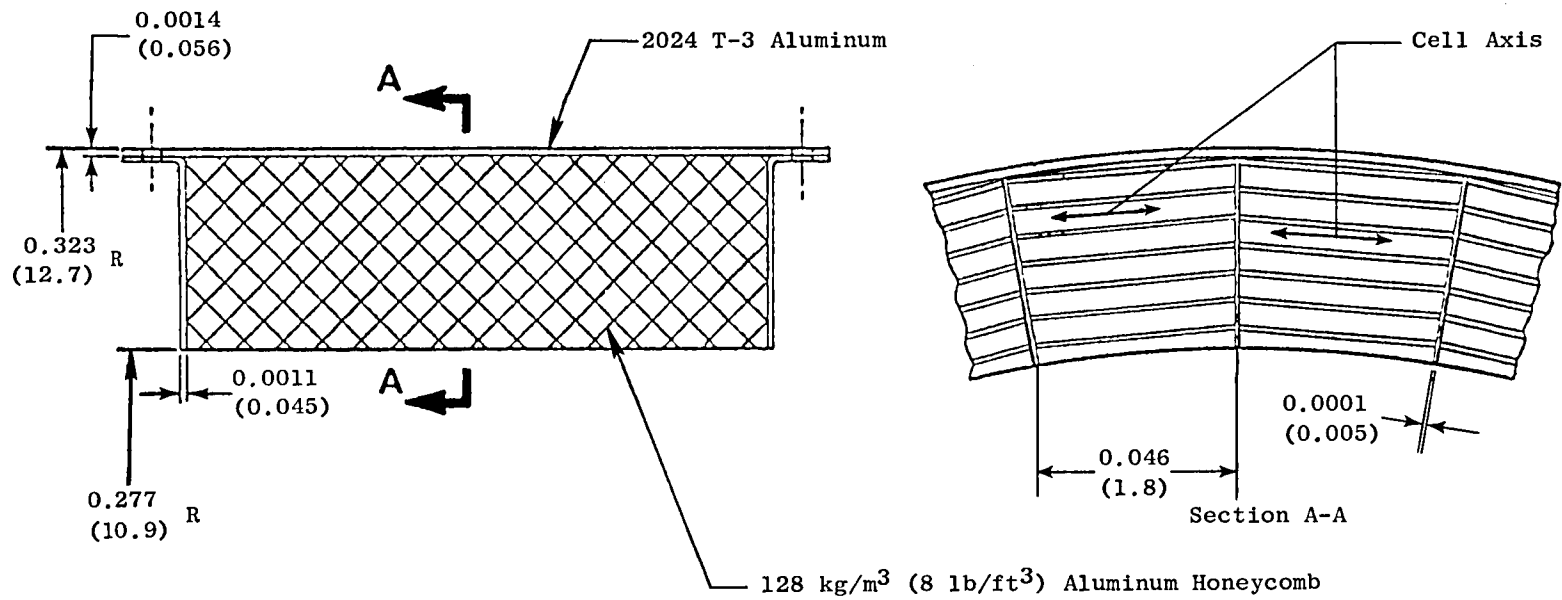
(b) Right

Figure 18. Nonfinned-Type Containment Structure.



- Dimensions: $\begin{matrix} \text{m} \\ \text{(in.)} \end{matrix}$

Figure 19. Kevlar Cloth-Filled Concept.



• Dimensions: ^m
(in.)

Figure 20. Honeycomb-Filled Concept.

- Dimensions: $\begin{matrix} \text{m} \\ (\text{in.}) \end{matrix}$
- Material = Steel AMS 5514

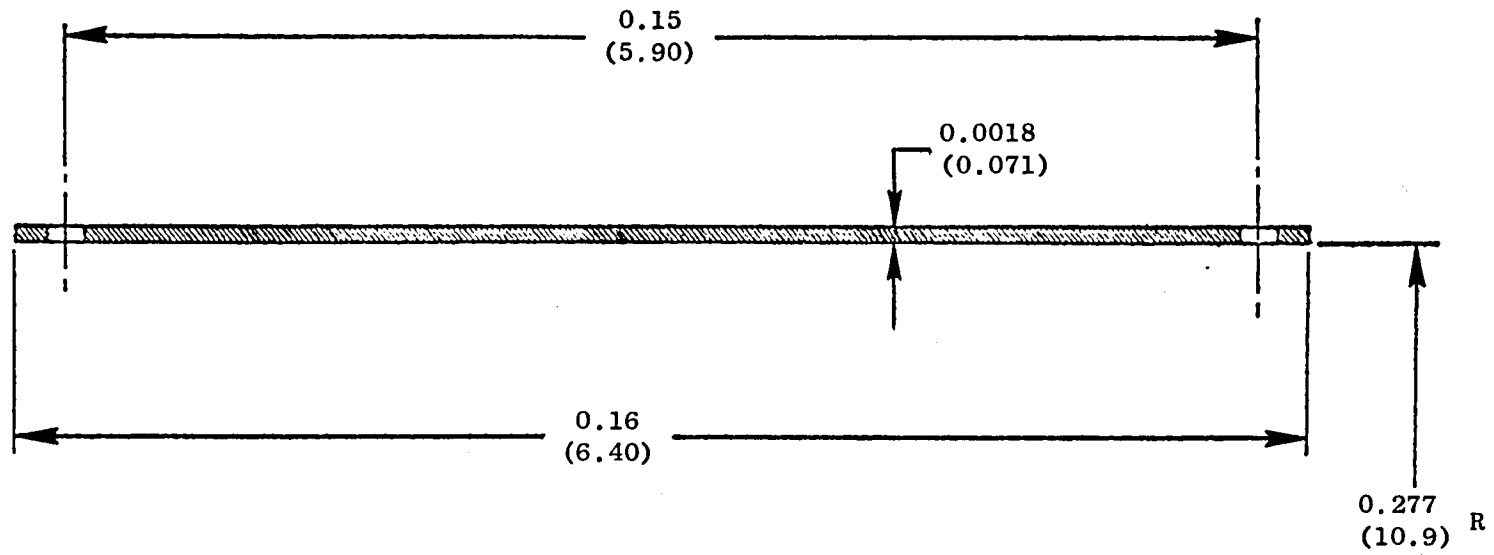


Figure 21. Current Practice Sheet Metal Ring.

Table II. Projectile Impact Testing Summary.

<u>Test</u>	<u>Type</u>	kg (lb) <u>Wp</u>	m/sec (fps) <u>V</u>	J (ft-lb) <u>K.E.</u>	N/m ² (lb/ft ²) <u>B</u>	Jm ² /N (ft ³) <u>K.E./B</u>	<u>Blade Type</u>	<u>Comments</u>
1	Steel	0.0581 (0.1281)	259.1 (850)	1948.5 (1437)	142.0 (2.965)	13.72 (485)	Titanium	Redirected
2	Steel	0.0581 (0.1281)	278.0 (912)	2242.8 (1654)	142.0 (2.965)	15.79 (558)	Titanium	Redirected
3	Steel	0.0306 (0.0675)	273.4 (897)	1143.1 (843)	142.0 (2.965)	8.047 (284)	Superhybrid	Shattered
4	Steel	0.0581 (0.1281)	267.0 (876)	2069.2 (1526)	142.0 (2.965)	14.57 (515)	Titanium	Redirected
5	Aluminum/Kevlar	0.0306 (0.0675)	224.0 (735)	767.5 (566)	69.71 (1.456)	11.01 (389)	Superhybrid	Caught
6	Aluminum/Kevlar	0.0581 (0.1281)	193.2 (634)	1084.8 (800)	69.71 (1.456)	15.56 (549)	Titanium	Caught - Kevlar Pulled Out
7	Honeycomb	0.0581 (0.1281)	280.4 (920)	2283.5 (1684)	99.11 (2.070)	23.04 (814)	Titanium	Punctured - Escaped
8	Honeycomb	0.0581 (0.1281)	286.5 (940)	2383.8 (1758)	99.11 (2.070)	24.05 (849)	Titanium	Punctured - Escaped
9	Titanium Finned	0.0306 (0.0675)	286.5 (940)	1255.7 (926)	164.2 (3.429)	7.641 (270)	Superhybrid	Caught - Slit Projectile
10	Titanium Finned	0.0581 (0.1281)	286.5 (940)	2383.8 (1758)	164.2 (3.429)	14.51 (513)	Titanium	Caught

Table II. Projectile Impact Testing Summary (Concluded).

<u>Test</u>	<u>Type</u>	<u>kg</u> (lb) <u>W_p</u>	<u>m/sec</u> (fps) <u>V</u>	<u>J</u> (ft-lb) <u>K.E.</u>	<u>N/m²</u> (lb/ft ²) <u>B</u>	<u>Jm²/N</u> (ft ³) <u>K.E./B</u>	<u>Blade Type</u>	<u>Comments</u>
11	Kevlar Finned-Long	0.0581 (0.1281)	286.5 (940)	2383.8 (1758)	163.1 (3.407)	14.61 (516)	Titanium	Punctured - Escaped
12	Kevlar Finned-Long	0.0306 (0.0675)	286.5 (940)	1255.7 (926)	163.1 (3.407)	7.703 (272)	Superhybrid	Caught - Slit Projectile
13	Aluminum Finned	0.0581 (0.1281)	286.5 (940)	2383.8 (1758)	166.2 (3.471)	14.34 (506)	Titanium	Punctured - Escaped
14	Aluminum Finned	0.0581 (0.1281)	232.3 (762)	1566.2 (1155)	166.2 (3.471)	9.423 (333)	Titanium	Caught
15	Kevlar Finned-Short	0.0581 (0.1281)	286.5 (940)	2383.8 (1758)	160.2 (3.345)	14.88 (526)	Titanium	Caught
16	Kevlar Finned-Short	0.0306 (0.0675)	286.5 (940)	1255.7 (926)	160.2 (3.345)	7.838 (277)	Superhybrid	Caught - Slit Projectile
17	Steel/ Kevlar-Thick	0.0581 (0.1281)	234.7 (770)	1598.7 (1179)	99.58 (579)	16.05 (579)	Titanium	Caught
18	Steel/ Kevlar-Thick	0.0581 (0.1281)	286.5 (940)	2383.8 (1758)	99.58 (2.038)	23.94 (863)	Titanium	Punctured - Caught- Kevlar Pulled Out
19	Steel/ Kevlar-Thin	0.0581 (0.1281)	233.8 (767)	1586.5 (1170)	87.43 (1.826)	18.15 (641)	Titanium	Punctured - Caught Barely - Kevlar Pulled Out
20	Steel/ Kevlar-Thin	0.0581 (0.1281)	220.4 (723)	1410.2 (1040)	87.43 (1.826)	16.13 (570)	Titanium	Partial Puncture - Caught

W_p - Blade Projectile Weight; V - Projectile Impact Velocity; K.E. - Projectile Kinetic Energy;
B - Containment Structure Weight Per Unit Area

weight of 14.7 kg/m^2 (3 lb/ft^2). The material and construction of the structure are representative of conventional, present-day fan containment practice.

Examination of the high-speed motion pictures showed that the blade projectile speed prior to striking the containment structure was close to 259.1 m/sec (850 ft/sec). The orientation and position of the projectile relative to the containment structure were excellent. Photographic quality was good, and the blade was clearly observable throughout the process. The resulting containment ring motion and gross deformation were also clearly observable.

The structure is shown in its posttest condition and still mounted in the test apparatus in Figures 22 and 23. Figure 22 presents an overall view of the structure as viewed approximately normal to the engine cross-section plane. Figure 23 shows a more detailed view of the path of the blade along the inner surface of the containment structure.

Substantial deformation of the structure resulted. This is characterized by heavy local bulging of the structure in the region where the deviation of the flight trajectory of the projectile was most abrupt. Large out-of-roundness occurred in the vicinity of the local bulging as shown in Figure 22, and this propagates with diminishing magnitude to remote regions of the structure. Twisting deformation of the structure was minor because the projectile trajectory remained centered relative to the width of the structure.

As is consistent with the blade orientation and position relative to the containment structure, the rear corner (corresponding to the tip, leading edge corner of the blade in an actual engine situation) struck the structure first. This produced a crease in the steel surface, as indicated by the arrow labeled 1 in Figure 23. Shortly thereafter, the forward (base) edge of the blade struck, and the blade rapidly becomes reoriented to a flat attitude relative to the surface of the structure. Throughout its subsequent motion, the blade remained in the flat orientation and did not experience any appreciable yaw. The visible track of the blade along the containment structure has a width close to the width dimension of the blade.

The velocity of the blade did not diminish substantially as it moved along the containment structure. It had a large velocity when it reached the 180° opposite end of the structure. A comparison with Watertown Arsenal data for the impact energy involved showed that the containment thickness was marginal for a obliquity angle of 60° . The fact that the actual obliquity angle was approximately 75° resulted in the successful containment of the projectile.

Test 2

The untested 90° portion of the stainless steel containment ring that was previously tested in Test 1 was employed for this test. Damage to the containment ring after Test 1 was essentially confined well within a 90° portion subjected to impact. Prior to conducting Test 2, the specimen was respoked.

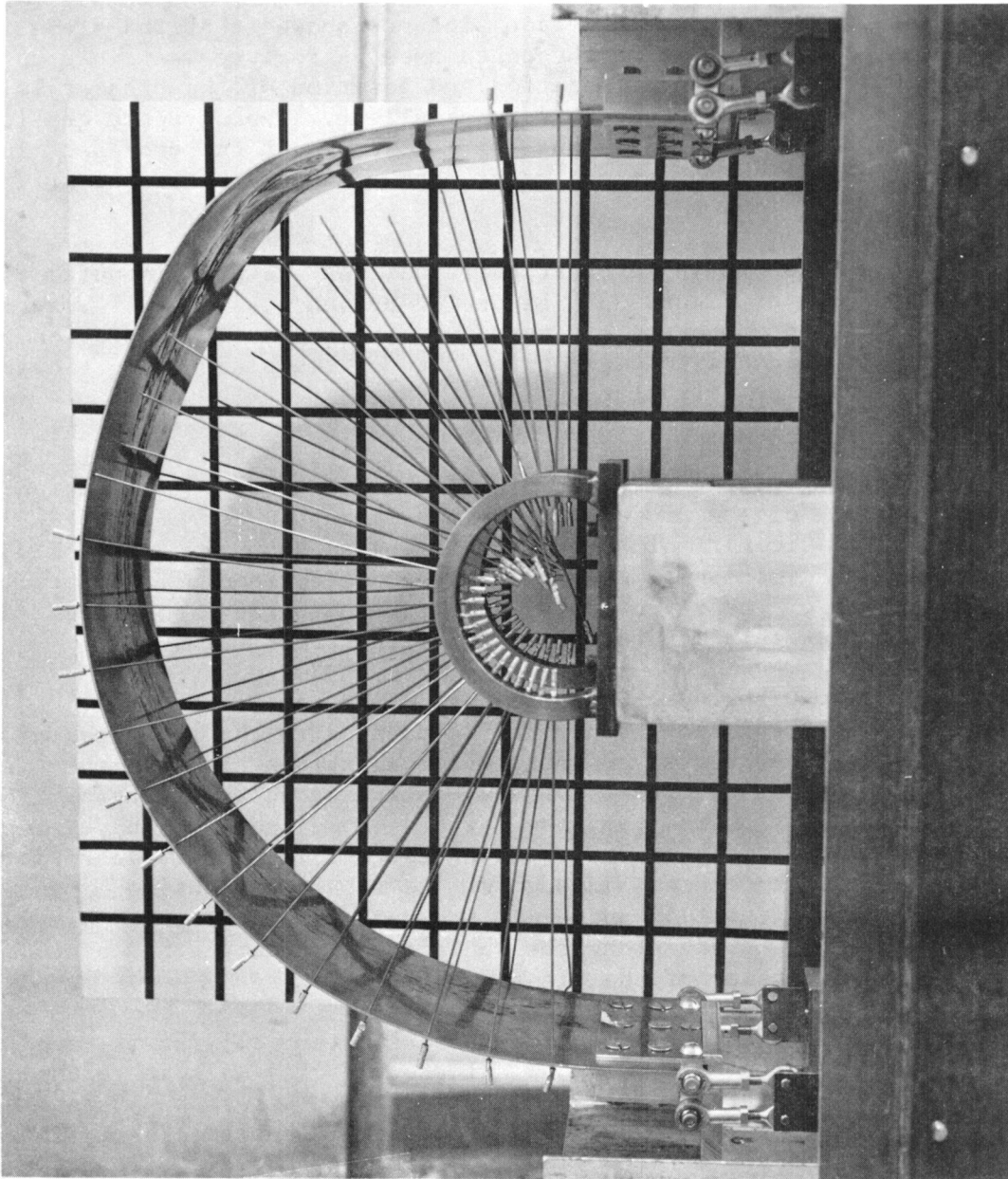


Figure 22. Posttest Condition of Type 321 Stainless Steel Containment Structure Showing Overall Out-of-Roundness Deformation - Blade Impact Velocity ~ 260 m/sec (850 ft/sec).

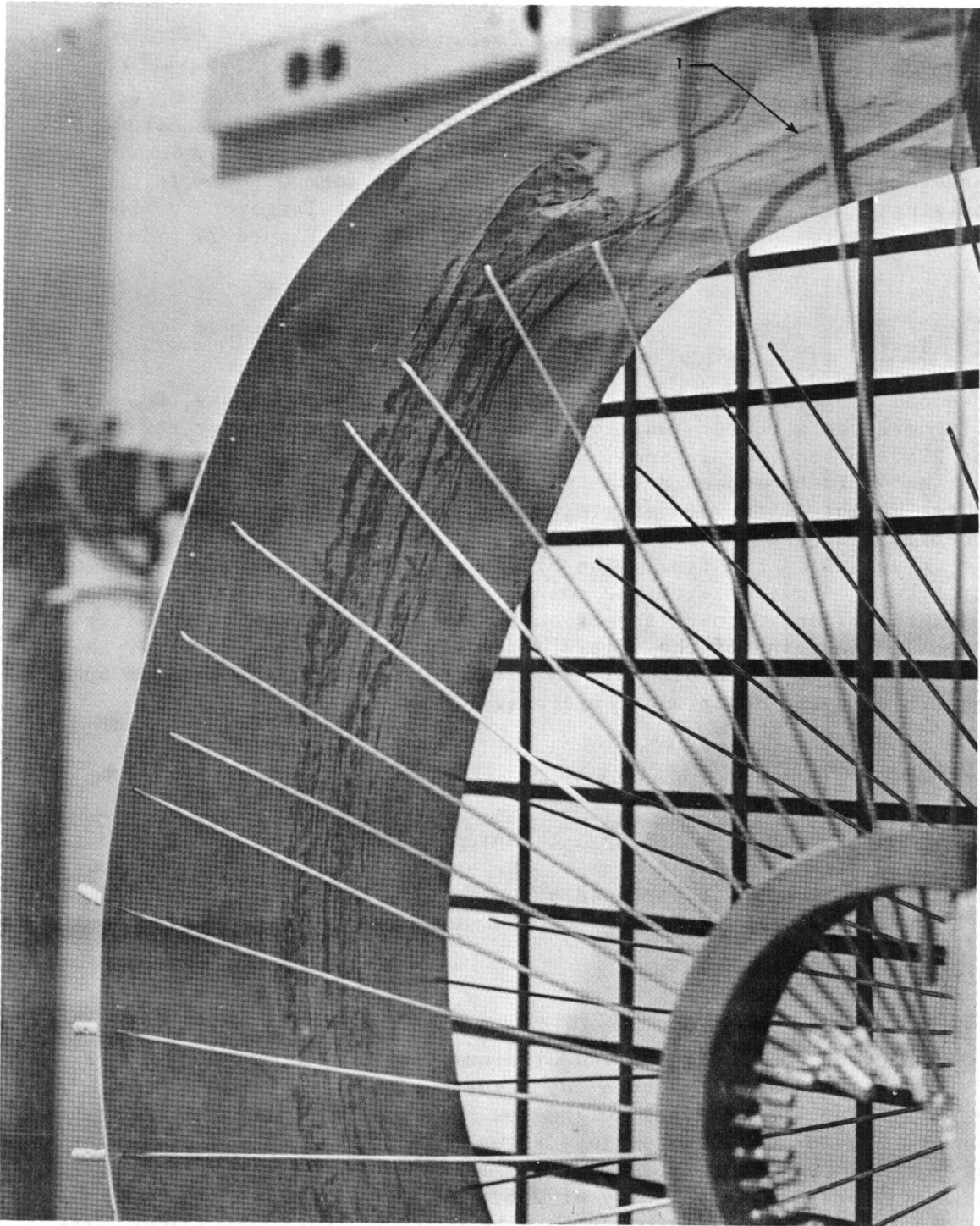


Figure 23. View of Inner Surface of Type 321 Stainless Steel Containment Structure After Impact at a Velocity of ~ 260 m/sec (850 ft/sec) Showing Large Local Deformation and Track of Blade Projectile.

A higher energy index, I_E^* , was employed for Test 2 and greater damage was inflicted on the ring than in the previous test. The blade was contained, however, and tracked near the center of the ring width for the entire 180° of the specimen, existing in the reverse direction of the initial velocity with considerable speed. The damage produced was in the form of out-of-roundness, local bulging, and bearing depressions similar to, but larger than, those of Test 1. The results of these two tests can be seen in Figure 24. Test 2 was at the top of the specimen.

Test 3

A second stainless steel specimen was adjusted to two tests, Nos. 3 and 4. In the former, the structure was impacted by a superhybrid blade at a velocity of about 273.4 m/sec (897 ft/sec). Considerably less damage was done to the specimen, as would be expected from the much lower energy index resulting from the lighter weight of the projectile. The high speed photographs did not show any perceptible breakup of the blade during its passage over the 100° of observable travel along the ring. The blade was, however, completely fragmented in its posttest condition with the composite constituent broken into many pieces and the titanium cover sheets entirely separated from one another and highly bent. The print of the initial impact was significantly wider than those left by the titanium blades. This indicates that initiation of breakup occurred early in the containment process.

Test 4

The structure was impacted by a titanium blade at a velocity of about 267 m/sec (876 ft/sec). The damage to the specimen was similar to that in Test 1. The specimen as it appeared after Tests 3 and 4 is shown in Figure 25. The superhybrid projectile impacted at the top of the specimen.

Test 5

This specimen, of double-walled aluminum construction filled with a mat of Kevlar cloth, was impacted by a superhybrid blade at a speed of 224 m/sec (735 ft/sec). The specimen was weighed as part of the pretest procedure and was found to have a unit weight close to half those of the previously tested structures. An energy index of 0.363 was selected, in accord with the test plan, and a corresponding velocity of 226.8 m/sec (744 ft/sec) was determined. This energy index value corresponds to a velocity of 320 m/sec (1050 ft/sec) for a unit weight equal to that of the stainless steel specimens employed in Tests 1 through 4.

* $I_E = K.E./BA$ (Reference Table I); A = Projectile Initial Footprint Area

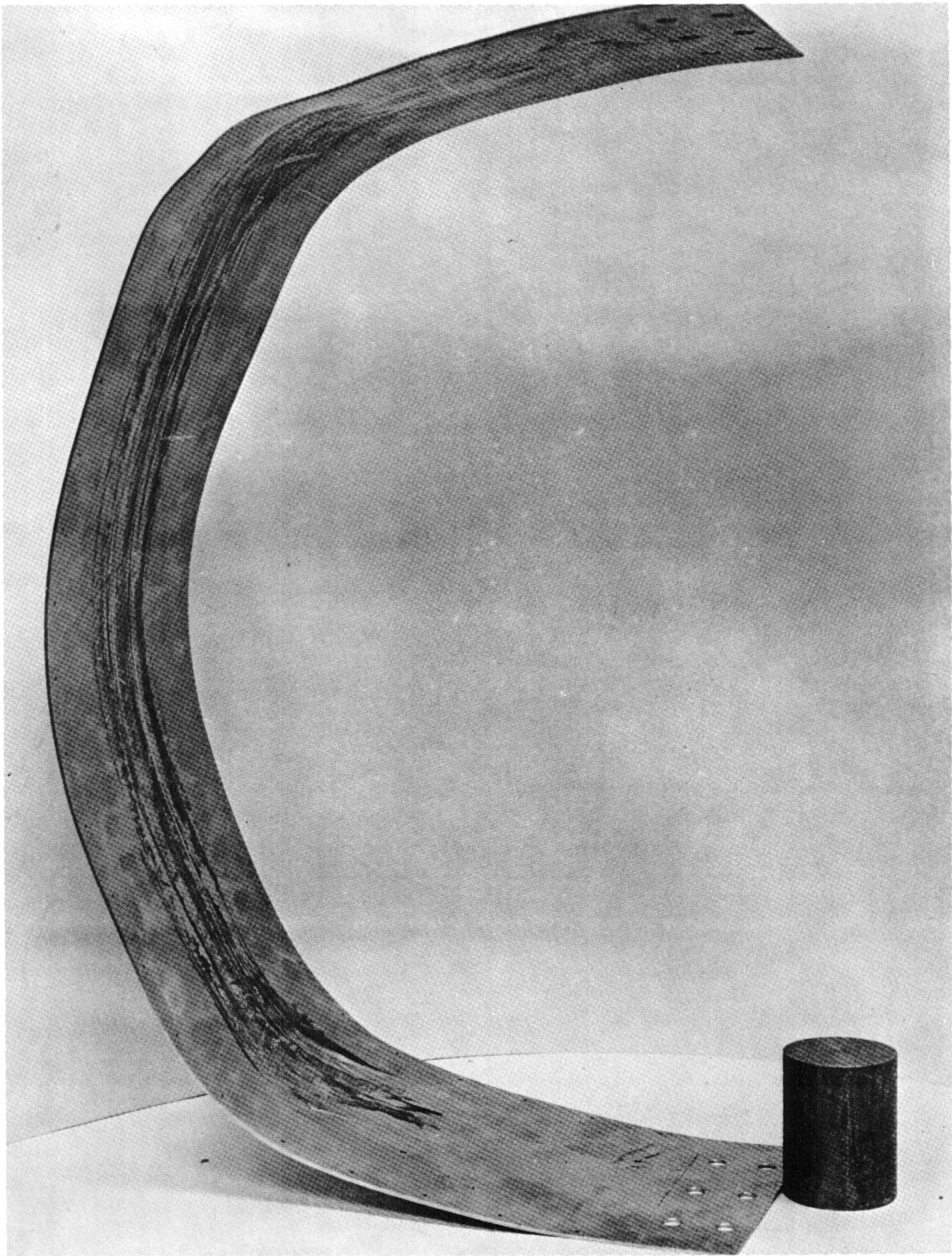


Figure 24. Steel Containment Structure After Tests 1 and 2.

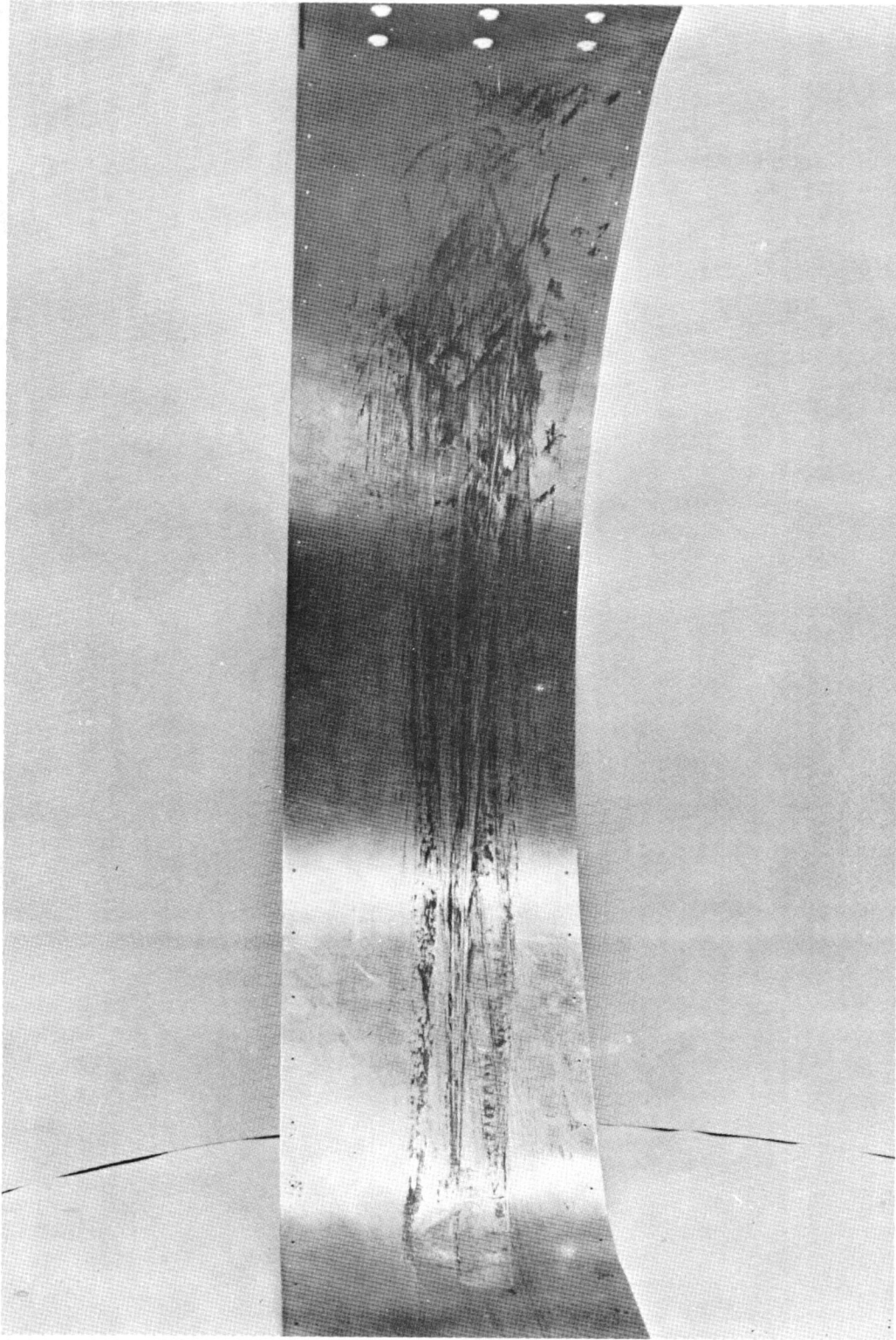


Figure 25. Steel Containment Structure After Tests 3 and 4.

The blade depressed the thin inner sheet upon initial impingement, leaving a distinctive wide print which appears to be characteristic of superhybrid blade impact impression. After deeply impressing the inner sheet, the blade cleanly sliced through it and entered the interior space. Apparently it was deflected by the Kevlar mat, but it did not cut the mat in the process. The blade proceeded to move entirely within the internal space and came to rest completely out of sight. As a result, the inner skin of the structure was bulged outward, resembling a pouch. The pouch region extends about 0.2 m (6 in.) along the curved contour of the structure. A small outward bulge was produced in the outer skin in the region of blade entry. The impact area is shown in Figures 26 and 27, the projectile being lodged in the bulged area apparent in Figure 27.

Overall, the structure looked impressively intact for having absorbed and dissipated 781.1 J (567 lb-ft) of energy. None of the supporting spokes was broken as a result of the test which is indicative of the ring's small resistance to radial deflection.

Test 6

The unused half of the specimen used in Test 5 was subjected to impact by a titanium blade projectile at a velocity of about 193.2 m/sec (634 ft/sec). The energy index was 0.509 which was equal to the Test 2 index, the highest value employed in all previous tests. Hence, considering both the 40% higher index and the use of a much more rugged blade projectile, this test was much more severe than Test 5. Nevertheless, the ring succeeded in completely stopping the blade and retaining it without any rupture of the external shell of the structure. The blade was not retained in the total manner of the previous test and protruded out from the inner shell as shown in Figure 28. A portion of the inner shell in the vicinity of the major interaction also protruded outward toward the center of the ring approximately 0.1 m (3 in.) radially from its initial position, having been sheared by the blade and subsequently torn. The behavior of the structure would probably have been cleaner if the Kevlar mat had remained secured at the end of the ring. Because of the attachment design, which was unrepresentative of a continuous circular band of material as would be used in a 360° containment structure, the end of the Kevlar mat was pulled out of the end by the blade action. As a result a considerable amount of Kevlar mat was displaced forward of the blade movement and gathered (via gross folding) in front of the moving blade. This resulted in the buildup of a substantial volume of mat within the space between the two walls and contributed to the dislodgement of inner casing material in the manner described previously. In addition, springback action of the highly folded Kevlar mat probably pushed the blade in the reverse direction out of a well retained position once the forward motion of the blade had been completely stopped.

The outer casing of the structure was bulged outward by a similar radial dimension as resulted in Test 5 but the bulging occurred over a greater circumferential distance. The ring assumed a moderate amount of out-of-roundness in the local region of impact. As in Test 5, not a single supporting spoke was broken.



Figure 26. Superhybrid Impact on Kevlar Belt Target.

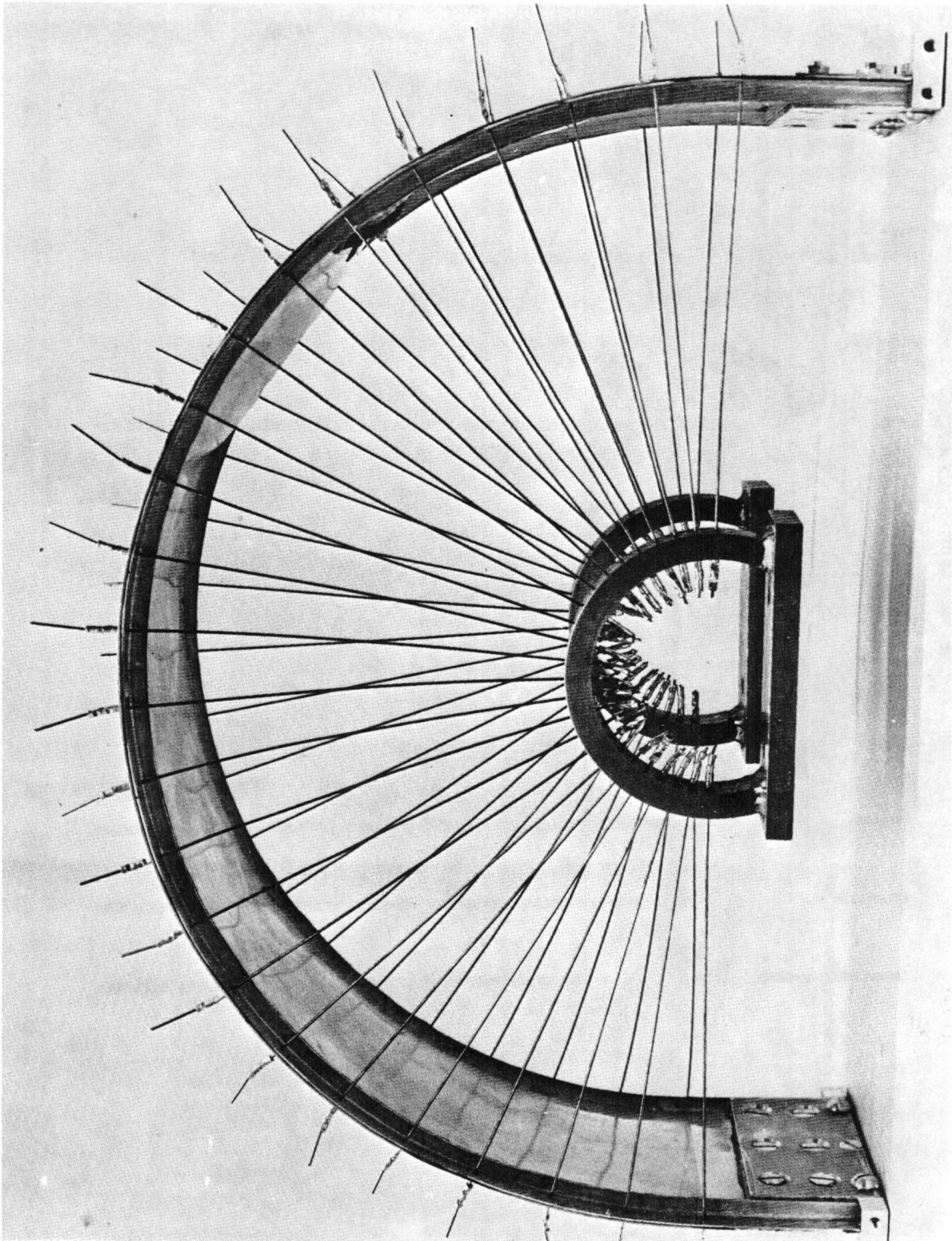


Figure 27. Superhybrid Projectile Contained by Kevlar Belt Target.

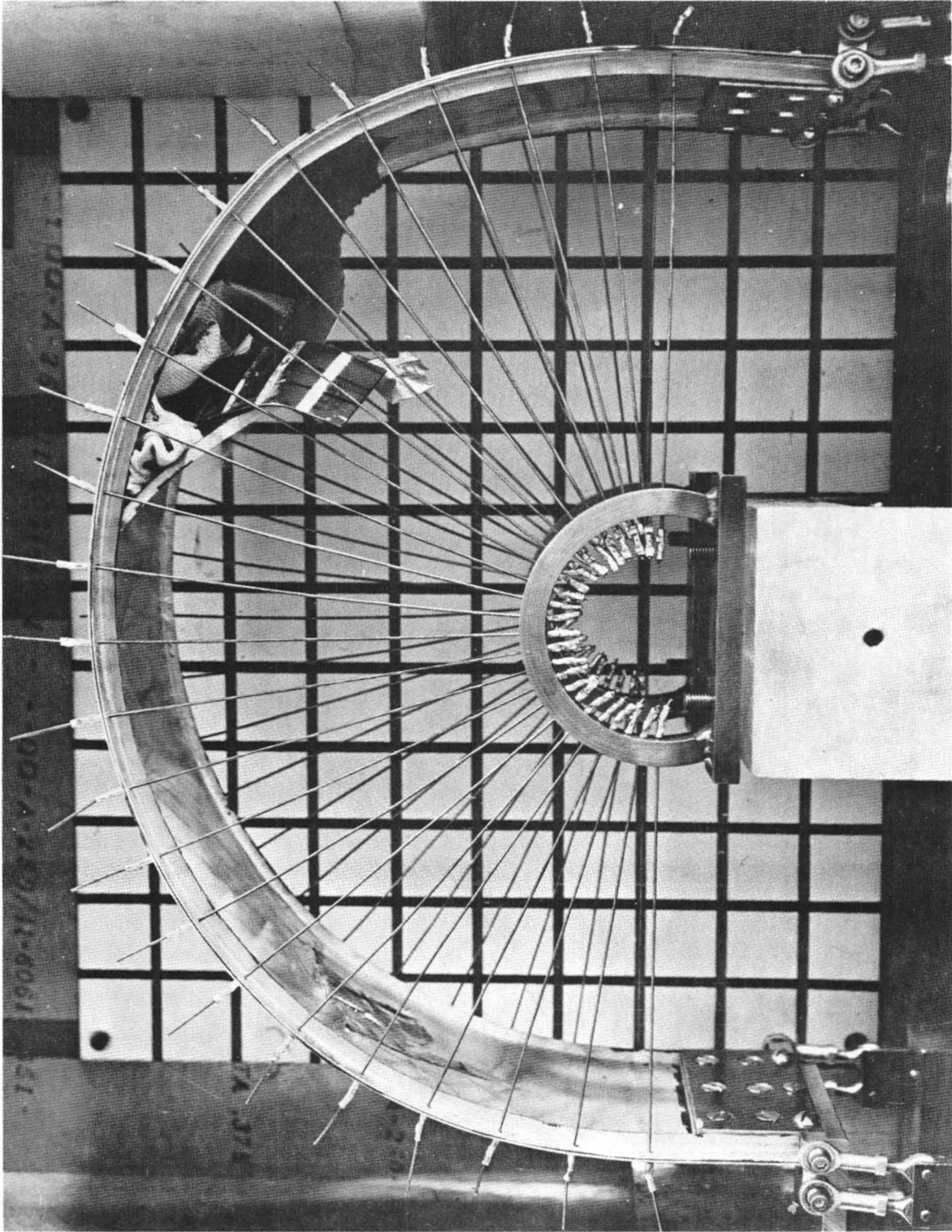


Figure 28. Titanium Projectile Contained by Kevlar Belt Target.

The amount of deformation of the blade was impressively low, in view of the relative lightness of the structure and the ruggedness of the titanium projectile. It was deformed to about the same extent as were the blades of Tests 2 and 4. The region situated between the impact and retention sites of both tests was found to be in good general condition.

Test 7

The specimen tested was an all-aluminum structure made up of segmented honeycomb having a density of 128 kg/m^3 (8 lb/ft^3). The honeycomb was bonded together within an external backing ring of $1.4 \times 10^{-3} \text{ m}$ (0.055 in.) thickness and two outboard boundary flanges of $1.1 \times 10^{-3} \text{ m}$ (0.045 in.) thickness.

The blade projectile (titanium) impacted the structure at 280.4 m/sec (920 ft/sec) at the typical orientation and location. It penetrated into the honeycomb region and proceeded through it to the 90° position of the structure where it exited at high velocity. The blade exited by separating the seam between the backing ring and the inboard closure flange (inboard position is adjacent to the grid plate; outboard position is adjacent to the plexiglass window). If the blade had not exited in this manner, it probably would have punctured either the closure flange or backing ring for it possessed sufficient kinetic energy to penetrate the aluminum grid plate a depth of $6 \times 10^{-3} \text{ m}$ (1/4 in.) when it later struck it.

The structure retained excellent roundness because of its high circumferential rigidity. This was as expected from its construction.

The test, however, showed the inadequacy of this design concept. The foil that makes up the honeycomb cell walls is quite thin, providing little resistance to shear. Such resistance is a nonlinear function of wall thickness, and very thin walls are easier to cut through per unit weight than thick walls. There is another reason this design is not very effective: only about half the cross section of a given cell can resist a slicing action that is parallel to the cell axis. Probably the blade sliced through much of the honeycomb in an orientation approximately parallel with the cell axis.

Test 8

The unused half of the honeycomb specimen from Test 7 was impacted by a titanium blade at a velocity of about 286.5 m/sec (940 ft/sec) in the typical manner. The projectile entered the honeycomb region in much the same way as did the projectile of Test 7. It travelled through the honeycomb until it burst at high velocity through the backing ring near the 80° position.

The difference between the results of Tests 7 and 8 can only partially be explained by the higher energy in the latter. Since the index was only slightly more than 4% higher, the difference is probably due mainly to the detailed paths of the projectile through the honeycomb structure. It seems

obvious that the blade completely overpowered the structure in both tests and that the reason that it did not break through the backing ring in Test 7 is that it found an easier path out of the structure through the seam. Hence, the structure performed poorly both in resistance to perforation and also in its inability to guide the projectile along a desirable path. The impact side of the target, as it appeared after Tests 7 and 8, is shown in Figure 29. The exit side after Test 8 is shown in Figure 30.

Test 9

A superhybrid blade was impacted at a speed of about 286.5 m/sec (940 ft/sec) and an energy density index I_E of 6.80×10^4 m (2.23×10^5 ft) against a titanium finned structure. It proceeded to deflect three central fins, causing them to bend and roll over. But the fins remained uncut, doubtless because the I_E was relatively low and the superhybrid blade fragmented during the early stages of contact. The blade broke up apparently before it had traversed a distance equal to its length. Damage to the three fins was limited to a region of about 0.1 m (4 in.) beyond which there is scarcely any trace of significant blade interaction.

The fins accelerated the blade break-up. The blade fragments nested deeply within the spaces between the fins. Most of the fragments swept around in these spaces and reached the other end of the ring, where they became firmly lodged.

The structure exhibited excellent roundness and overall deformation resistance. Fin deformations were such that all material was displaced into the interior of the ring section, a very desirable trait for precluding interactions with other rotor blades. The impact side of the specimen is shown in Figure 31.

Test 10

The unused half of the Test 9 titanium finned structure was impacted by a titanium blade at a velocity of about 286.5 m/sec (940 ft/sec) and an energy density index (I_E) of 1.30×10^5 m (4.28×10^5 ft). Upon impact, the blade proceeded to cut the forth inboard fin, as shown in Figure 32, and then to bend over the adjacent three outboard fins, generally causing one to press against the next as it proceeded on. After this, the blade cut through these three fins near their bases but outside the backing ring-fin joints. After proceeding to cut through the three inboard fins, the blade deeply nested within the interior of the structure, and gradually came to rest, firmly locked in the inboard fins.

The structure exhibited excellent roundness, and the backing ring remained virtually unaffected by the impact. No material was displaced into the flowpath region of the ring. The impact side is shown in Figure 32. The captured projectile can be seen protruding from the right side of the target of the 90° counterclockwise position.

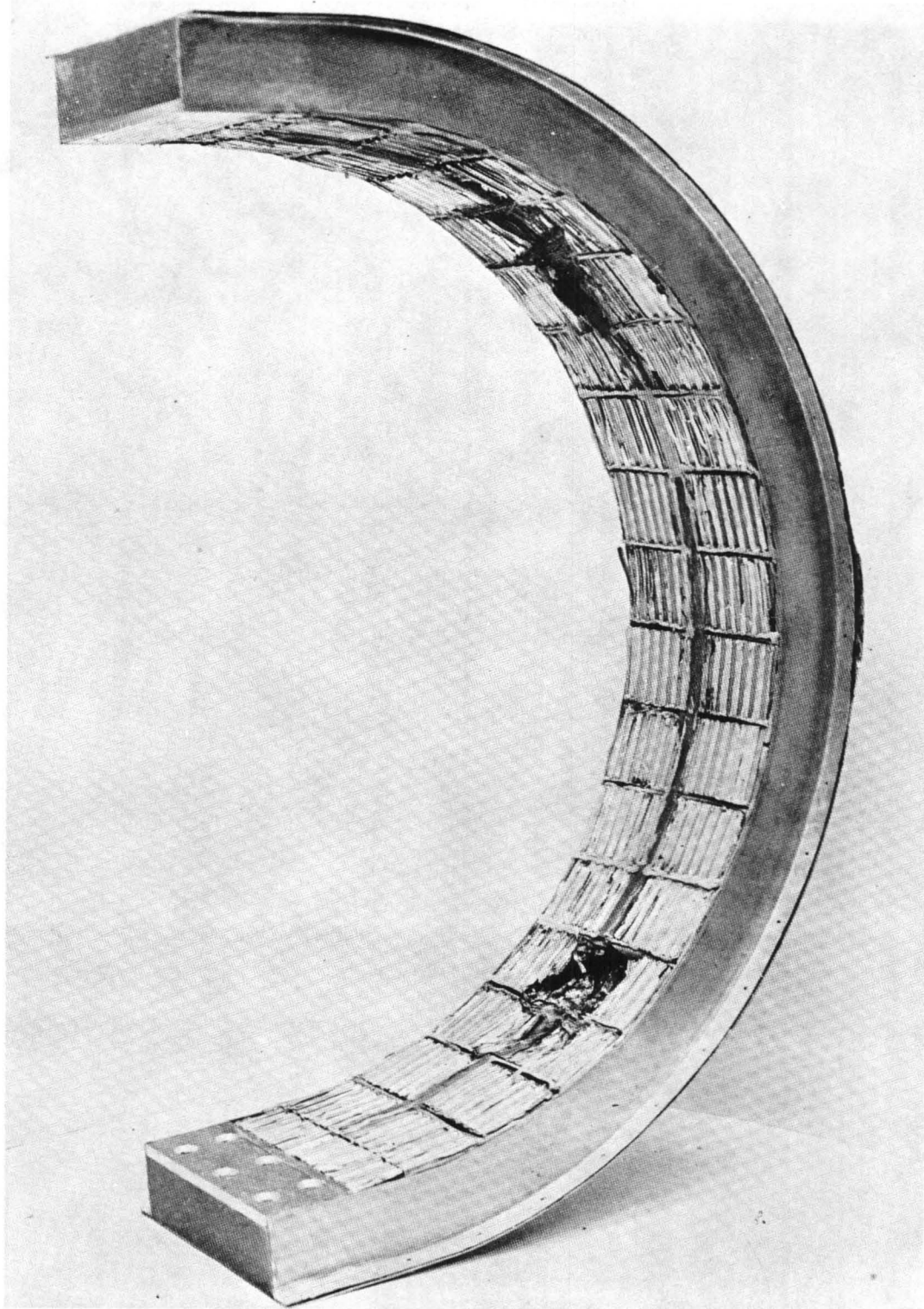


Figure 29. Impact Side of Transverse Honeycomb Target.

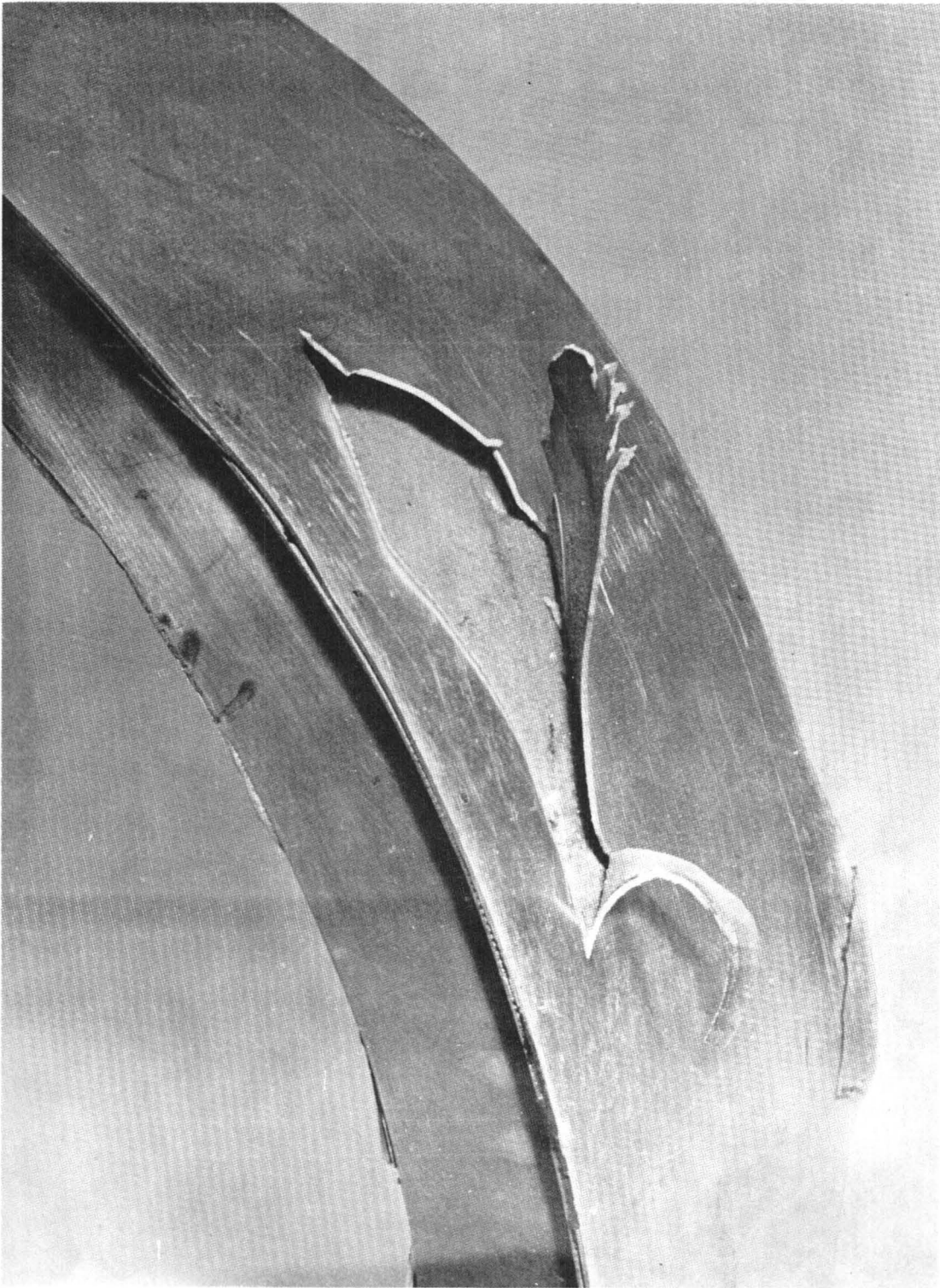


Figure 30. Typical Exit Side - Penetration of Transverse Honeycomb Target.

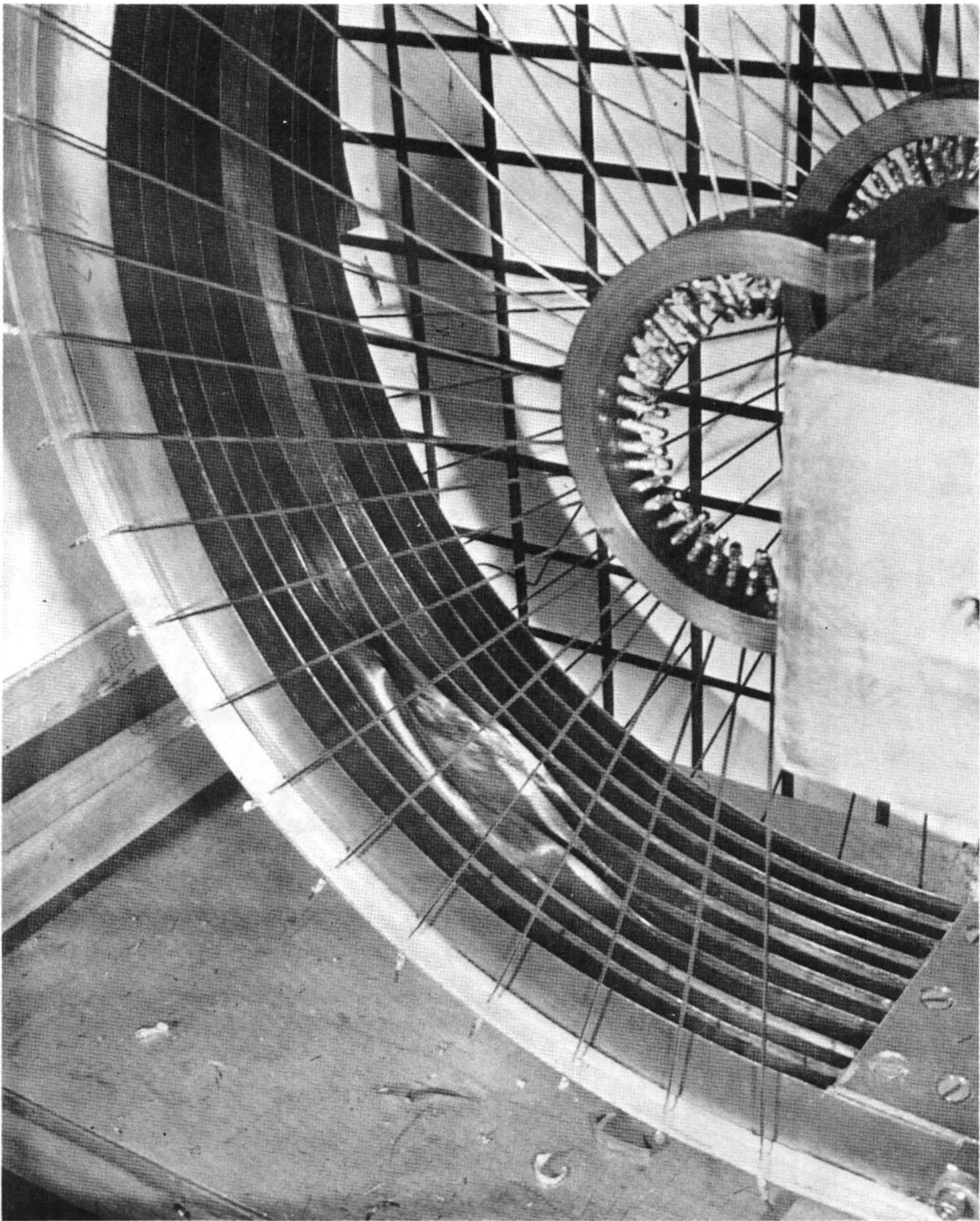


Figure 31. Impact Side of Titanium Finned Target after Impact of a Superhybrid Projectile.

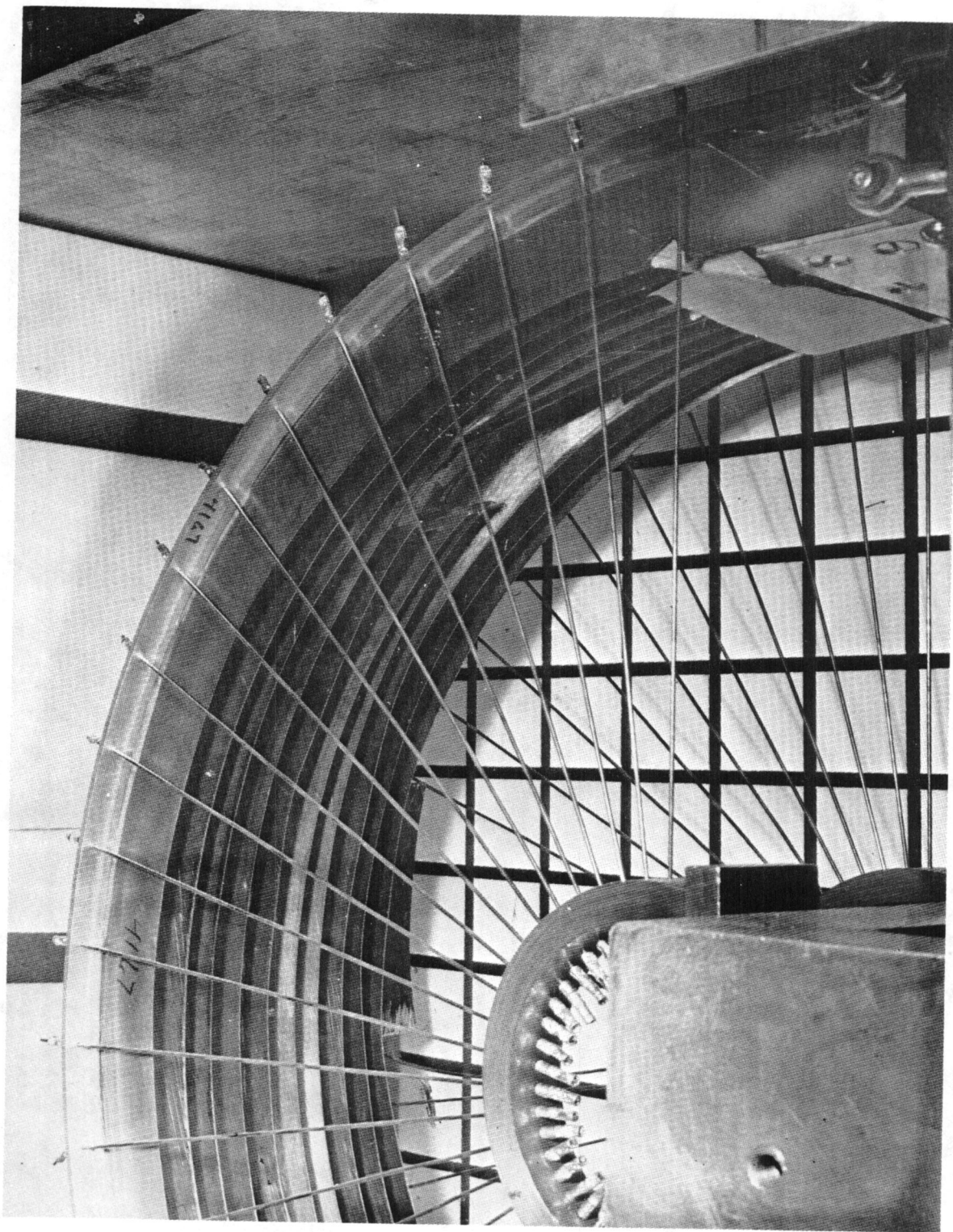


Figure 32. Titanium Projectile Contained by Titanium Finned Target.

Test 11

The target for this test was the long-finned Kevlar design whose only major difference from the titanium finned design used for Tests 9 and 10 was that its fins were fabricated from 1.4×10^{-3} m (0.054 in.)-thick Kevlar/epoxy laminate.

A titanium blade projectile impacted the structure at a speed of about 286.5 m/sec (940 ft/sec) and typical orientation and location. It cut clearly through three fins and tore completely through the aluminum backing ring. In the process, the blade trajectory curved downward and into the ring as it usually does. Exiting the structure at considerable velocity, it struck the rigid urethane foam back, penetrating it by the combined action of directly knifing the edges and crushing the block. The crushing occurred because of the rotation of the broad surface of the blade against the surface of the block.

The behavior of this structure is in marked contrast to that of the titanium finned specimen tested in Test 10. In the present case, the blade was prevented from rotating into a flat orientation relative to the curve contour of the structure, because the Kevlar/epoxy laminate, its epoxy matrix being so strong, gave way too easily to the blade's shearing action. Failure to let the blade orient as desired, coupled with failure to slow the blade sufficiently in the process, resulted in very severe projectile edge striking conditions.

Test 12

This test utilized the same targets as Test 11, but this time a super-hybrid projectile was used. The projectile impacted the target at a velocity of 286.5 m/sec (940 ft/sec) and cut cleanly through three fins and proceeded to fragment as it impinged against the backing ring. The blade was cut into several strips approximately equal in width to the fin spacing. Apart from the cutting of its fins, no further visible damage was sustained by the structure.

Test 13

A titanium blade projectile was impacted at a velocity of about 286.5 m/sec (940 ft/sec) against a finned aluminum structure. The blade initially interacted with the fins in a manner similar to that of the previously tested finned titanium structure. The projectile trajectory was not, however, bent sufficiently during the process to engage the backing ring in a flat attitude; and as a result, it sliced cleanly through the backing ring at considerable velocity. As shown in Figure 33, the blade sliced through three central fins, bending the interior parts of the cut fins as it passed over them on its way through the backing plate.

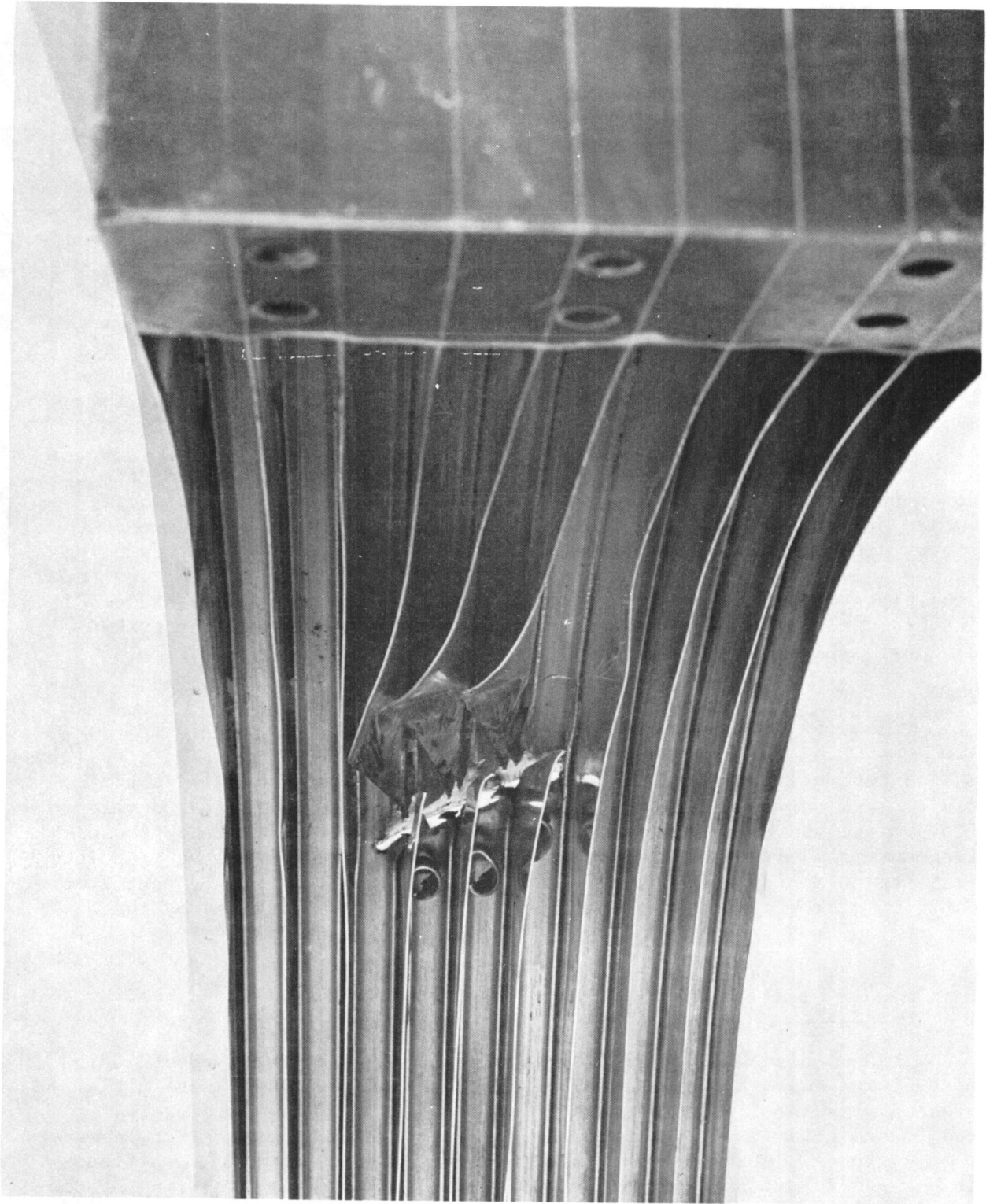


Figure 33. Penetration of Aluminum Finned Target.

It is evident that the aluminum fins demonstrated considerably less resistance to the blade action than the titanium fins. This may be because of the greater shear strength of 6Al-4V titanium relative to 2024 T-3 aluminum. The exit side of the test specimen is shown in Figure 34.

Test 14

In order to demonstrate the expected desirable nesting and capturing qualities of the finned aluminum structure, this test was performed at a sufficiently lower velocity to avoid the penetration through the backing ring experienced in Test 13. A titanium blade was impacted at a speed of 231.6 m/sec (760 ft/sec) on the other side of the finned aluminum structure. The blade cut through three central fins in a manner similar to the fin-cutting of Test 13 except this time, the cut length was considerably greater. The appearance of the affected region was remarkably similar to that of the previous test demonstrating that the containment process and the testing technique itself are both highly reproducible. In this test, however, the blade did not significantly affect the backing ring. It produced no observable deformation of the exterior ring surface, and it did not contact the interior at all. Instead, it came to rest after becoming nested deep into the structure. Later, as expected, the blade fell out of its nested position and was found resting directly below.

Test 15

A titanium blade projectile was impacted at a velocity of about 286.5 m/sec (940 ft/sec) against the short-finned Kevlar structure. The blade cut through the usual set of three central fins less cleanly than the titanium blade used against the long (thin)-finned Kevlar structure in Test 11. The blade was captured by the structure and remained with it. The final nesting condition was poor, but good nesting behavior was not expected of this specimen because of its relatively shallow depth.

The overall performance of this structure was impressive. Despite weighing 8.5% less than the long-finned Kevlar specimen of Test 11, it resisted penetration whereas the other had been penetrated at considerable velocity.

The specimen success can be attributed to the use of fins that were more rugged because they were twice as thick - 2.8×10^{-3} m versus 1.4×10^{-3} m (0.11 in. versus 0.054 in.). Unlike the long fins of the other structure, these fins were not cut clearly and showed evidence of having resisted high bearing pressure due to blade action. As a result, the forward portion of the blade may have been bent (as the recovered blades show) and/or rotated during early engagement. Either effect would act to decrease the severity of subsequent interactions. In fact, after cutting through the fins, the blade impacted heavily against the backing ring and deeply dented it locally. Yet, the overall roundness of the structure remained excellent.

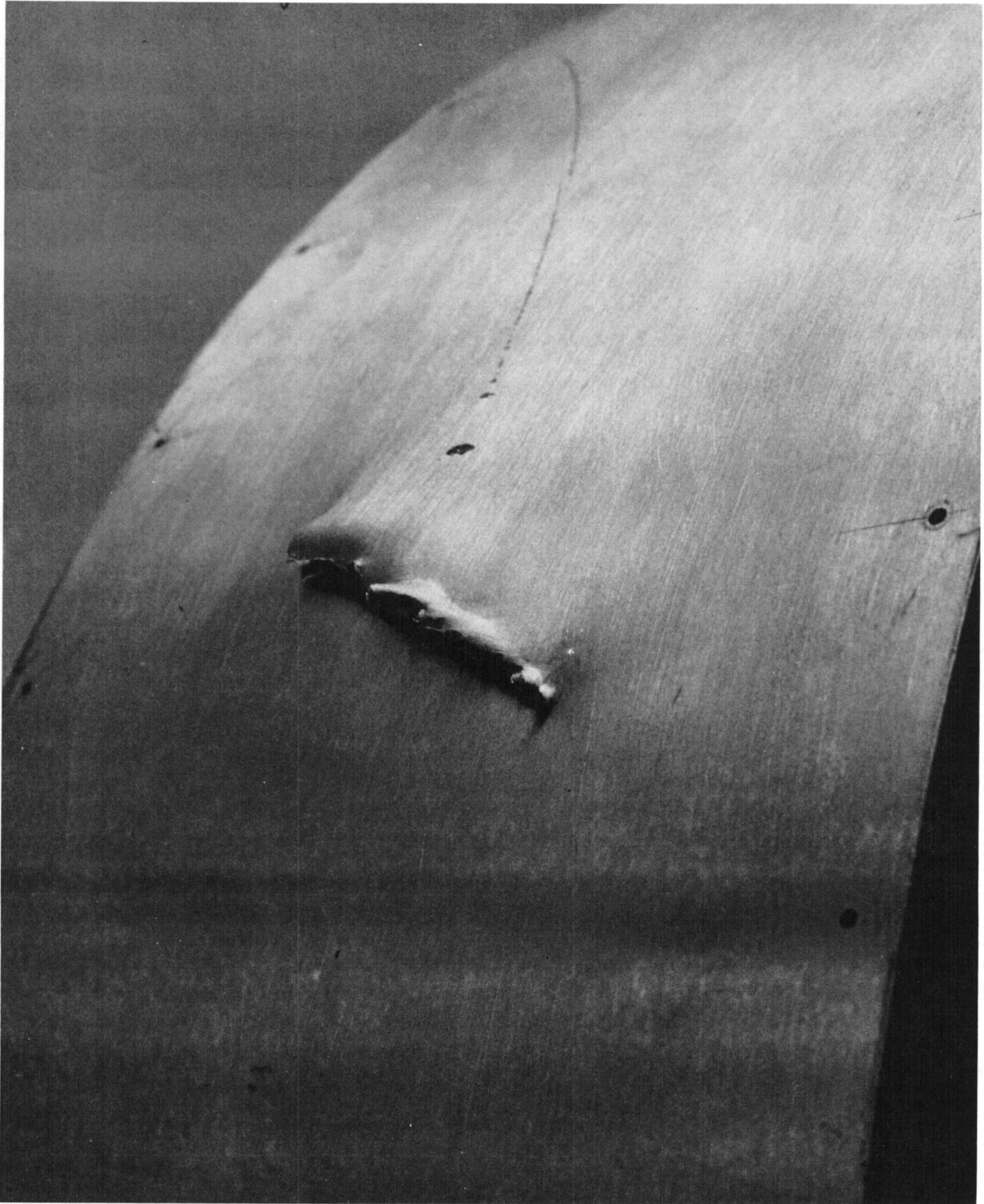


Figure 34. Exit Side - Aluminum Finned Target - Test 13.

Test 16

A superhybrid blade was impacted against the unused quadrant of the short-finned Kevlar structure at a velocity of about 286.5 m/sec (940 ft/sec). The initial interaction is quite similar to that of Test 15 with three central fins cut and "machined" away locally. During this time, the blade apparently fragmented; and as a result, the structure sustained no damage beyond the initially affected region. As it had with the other finned structures, the superhybrid blade was neatly cut into strips by adjacent fins; and the resulting fragments became deeply nested within the spaces between fins and retained there. Figure 35 shows the containment structure as it appeared after Tests 15 and 16. The titanium projectile impacted the structure on the right-hand side (note bulge in back plate) and the superhybrid projectile, on the left side.

Test 17 through 20

The last four tests all involved specimen designs utilizing a double wall metallic structure with a woven Kevlar belt interposed between the walls over their entire length. Two specimens were used: one for Tests 17 and 18, and the other for Tests 19 and 20. For each specimen the inner walls were of stainless steel (AMS4037) sheet, 3.8×10^{-3} m (0.015 in.) thick. The walls were separated by two boundary strips of plastic composite material along their width edges. The specimens differed in the number of Kevlar cloth plies utilized in the belt and hence, also differed in the corresponding thickness required for accommodating them between the metallic walls. These tests were performed with very high energy index values. In Tests 17 and 20, the blade was captured and in Tests 18 and 19, the blade was retained within the Kevlar cloth after breaking through the metallic walls of the specimen. Overall deformation resistance exhibited by the specimens was good to excellent. Excellent consistency in performance was obtained among these tests. All tests were conducted using titanium projectiles.

In Test 17, the target contained 11 plies of dry Kevlar cloth and was impacted at 235.6 m/sec (773 ft/sec). Figures 36 and 37 show the blade deeply embedded in the structure. The blade cut through the inner metallic skin and produced a moderate local bulge in the outer skin (Figure 38). The ring is moderately out-of-round in the vicinity of the final blade position. No support spokes were broken (nor in Tests 18 and 19).

This target was then turned upside down and Test 18 was conducted with a projectile velocity of 289 m/sec (948 ft/sec). Figures 39 and 40 show that the blade cut cleanly through the inner skin and burst through the outer skin, carrying with it a large amount of Kevlar cloth. Overall deformation of the inner skin was slight and overall roundness excellent. In Figure 40 the blade is shown protruding from the Kevlar cloth in which it was retained after rupturing the outer skin (Figure 41). The large amount of Kevlar cloth removed from the ring interior is not representative of the behavior of a circumferentially continuous belt; for in this test, the cloth pulled away from its attachment to the end of the specimen as it had in Test 6. The very high energy applied in this test is especially noteworthy.

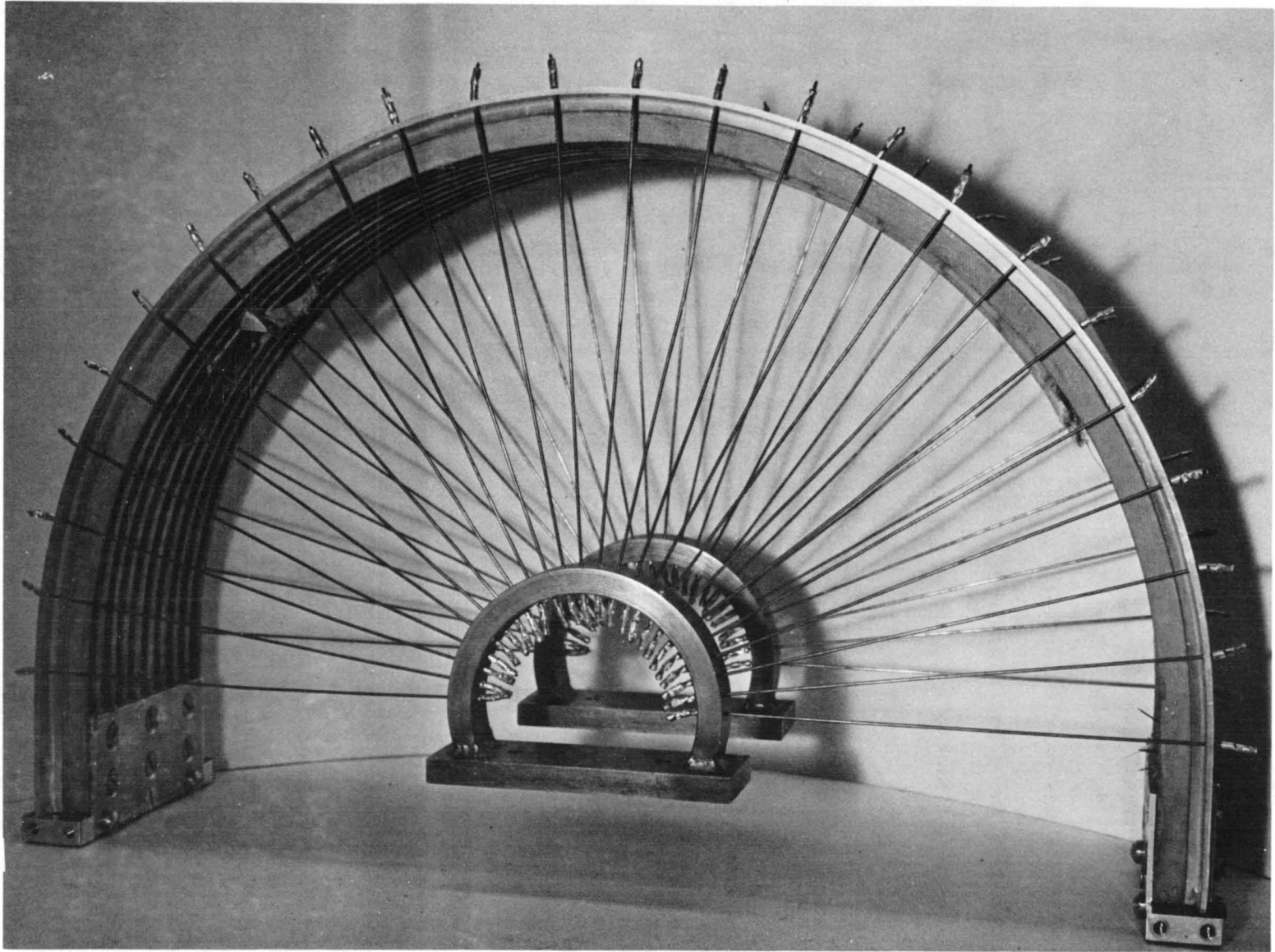


Figure 35. Short-Finned Kevlar Target After Impact.

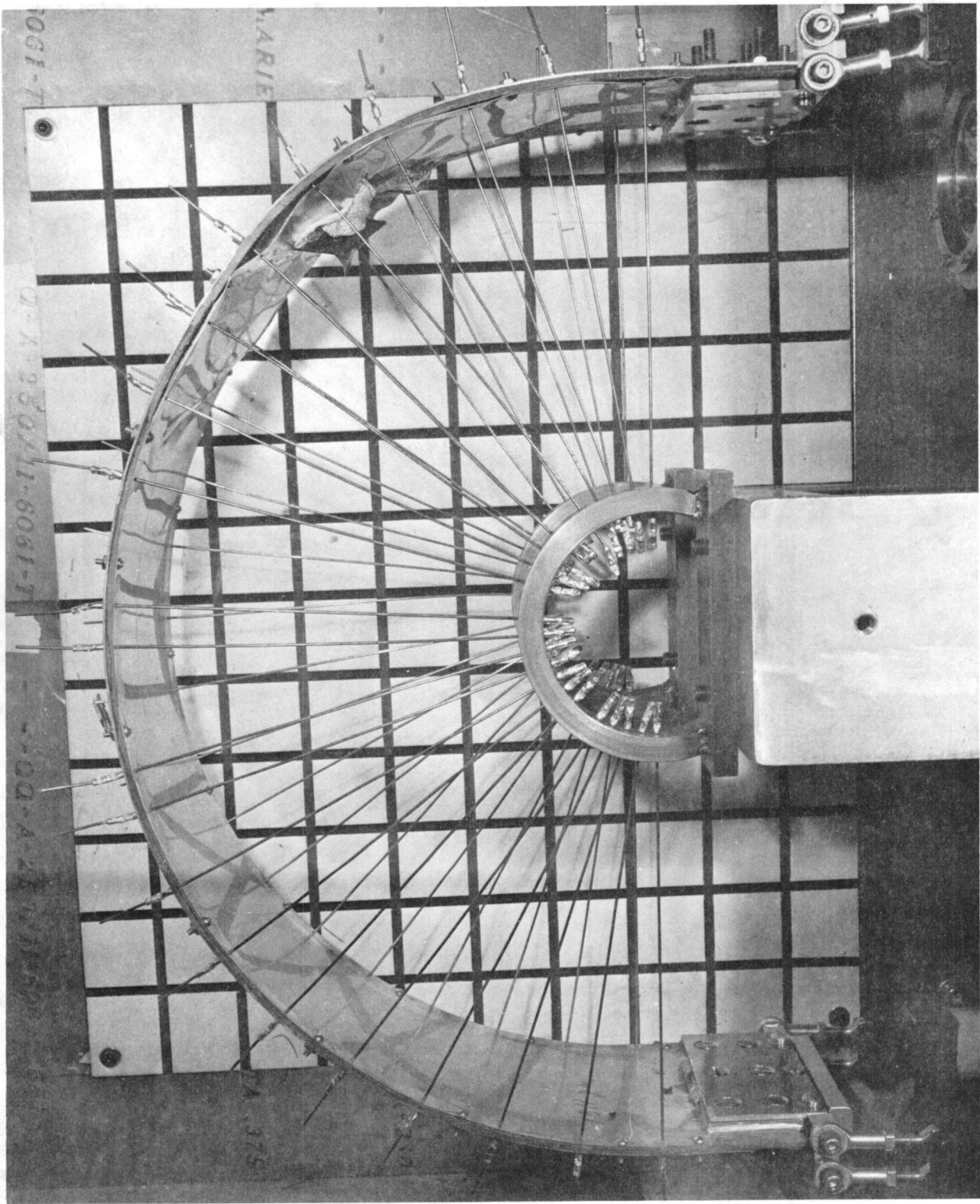


Figure 36. Test 17 - Side View.

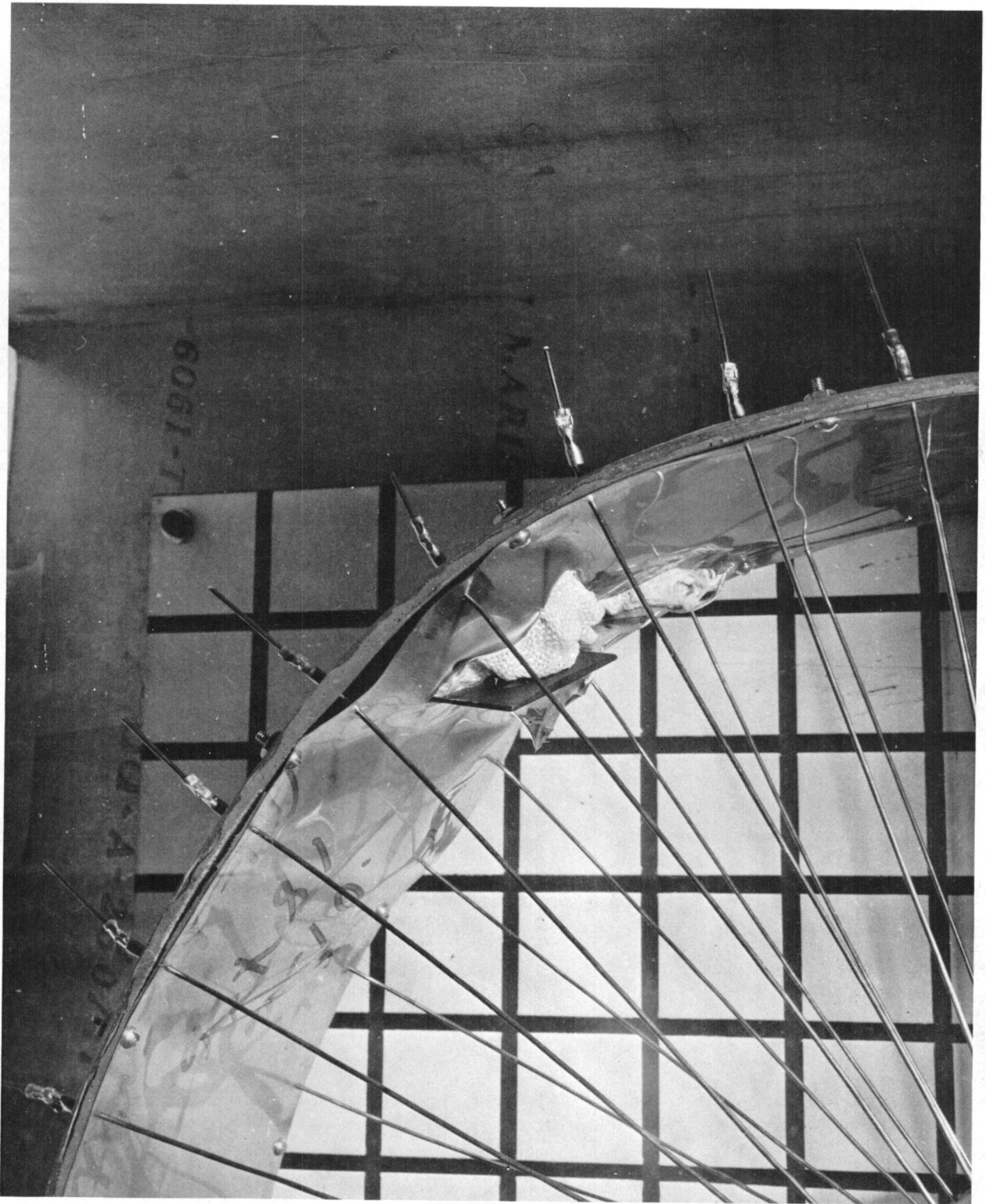


Figure 37. Test 17 - Interior Closeup.

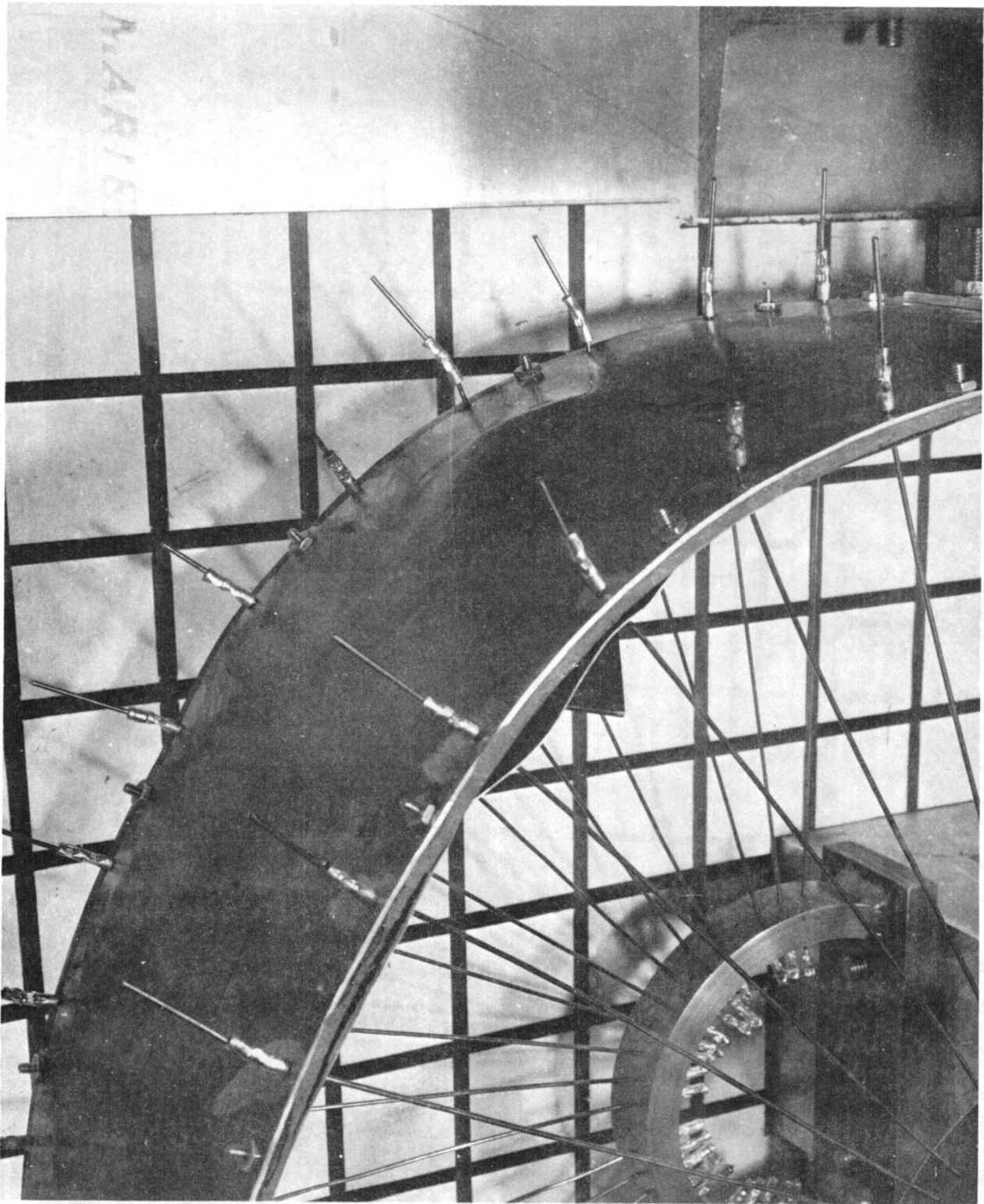


Figure 38. Test 17 - Exterior Closeup.

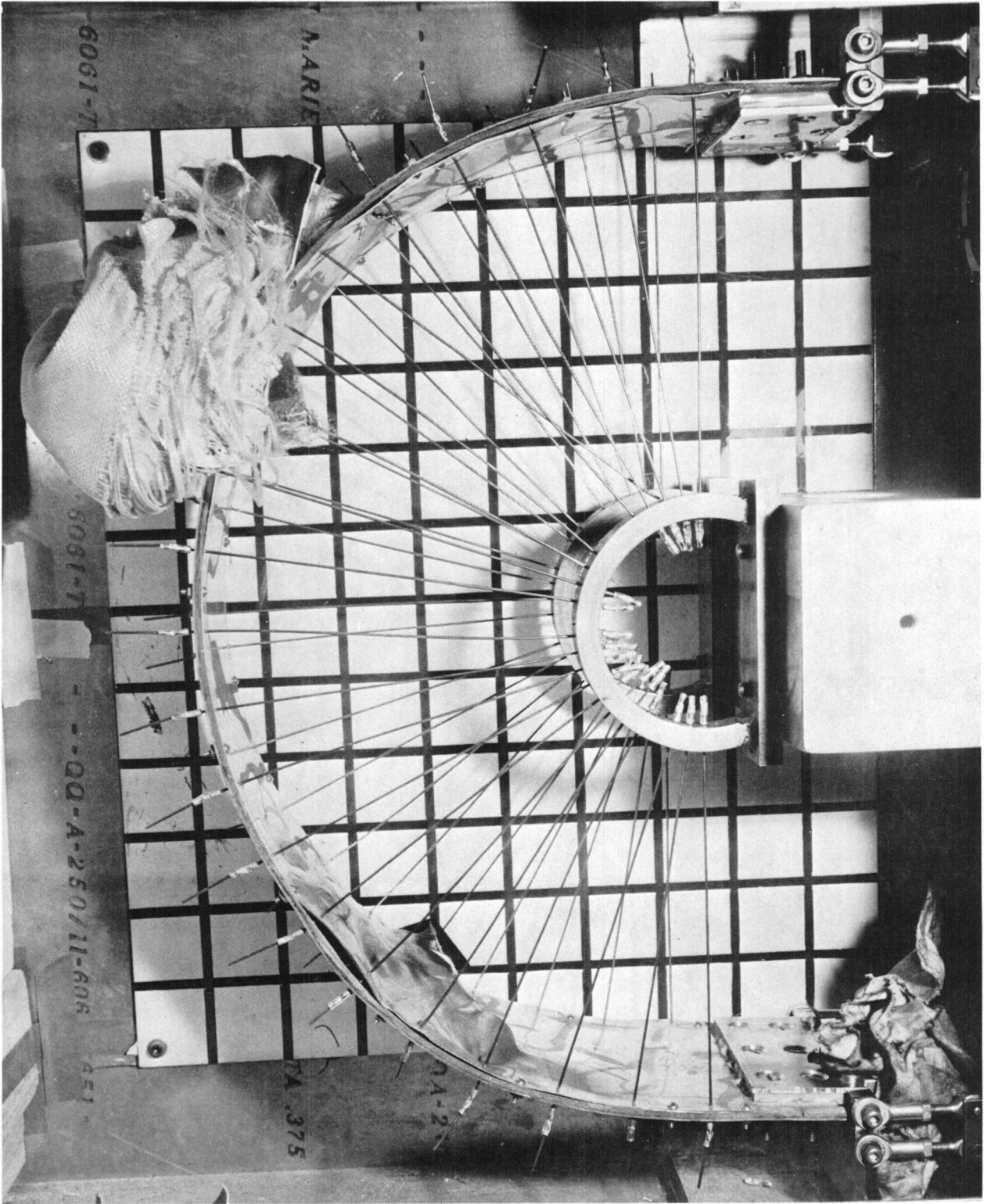


Figure 39. Test 18 - Side View.

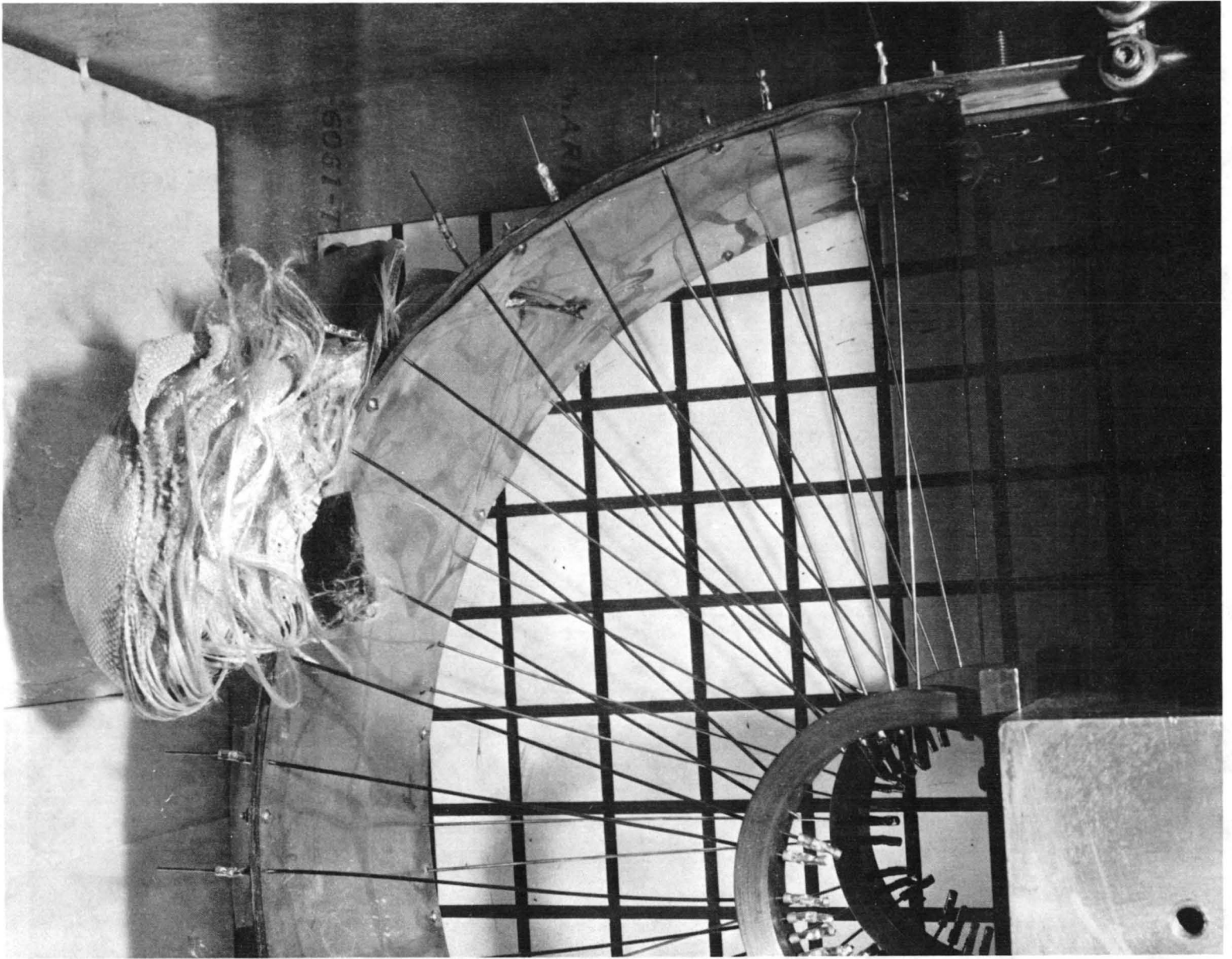


Figure 40. Test 18 - Interior Closeup.



Figure 41. Test 18 - Exterior Closeup.

For Tests 19 and 20 the target was of the same concept except that only seven plies of dry Kevlar cloth were used. In Test 19 the impacting velocity was 235.9 m/sec (774 ft/sec). The behavior of this specimen was very similar in all respects to that of the specimen tested in Test 18 which was impacted at a much higher velocity. Figure 42 shows the retained position of the blade within the Kevlar cloth. Comparison with the results of Test 18 bears out the great effectiveness of using dry Kevlar cloth, since the two specimens, both successful, differed only in their number of cloth plies.

For Test 20, the same target was impacted at 223.1 m/sec (732 ft/sec) which resulted in approximately the same energy index as that of Test 17. The captured position of the blade is shown in Figures 43 and 44. The outer skin was ruptured locally; but as shown in Figure 45, the Kevlar cloth was relatively undisturbed and was not cut. The ring's resultant out-of-roundness was moderate but noticeably more pronounced than that of Test 17. This was accompanied by the failure of three support spokes.

It is significant that, in the two cases (Tests 17 and 20) in which the blade was retained by the structure, a moderate out-of-roundness resulted; whereas, when the blade grossly perforated the structure (being retained externally to it within the Kevlar cloth), the ring remained round. The difference in behavior suggests that the Kevlar cloth was the principal agent for absorbing the impact, especially for Tests 18 and 19. The cloth decelerated the blade over a much longer distance keeping the forces applied to the structure lower than those reached in Tests 17 and 20 despite originally higher energy values.

The overall small thickness employed in the specimens of Tests 17 through 20 did not permit good nesting capability. Demonstration of this function was not the principal aim of these tests, but rather, determination of the effectiveness of the Kevlar woven ply construction for lightweight containment. It was evident, however, that good nesting could be achieved by incorporating a relatively low resistance nesting structure between the inner facing and the Kevlar layers.

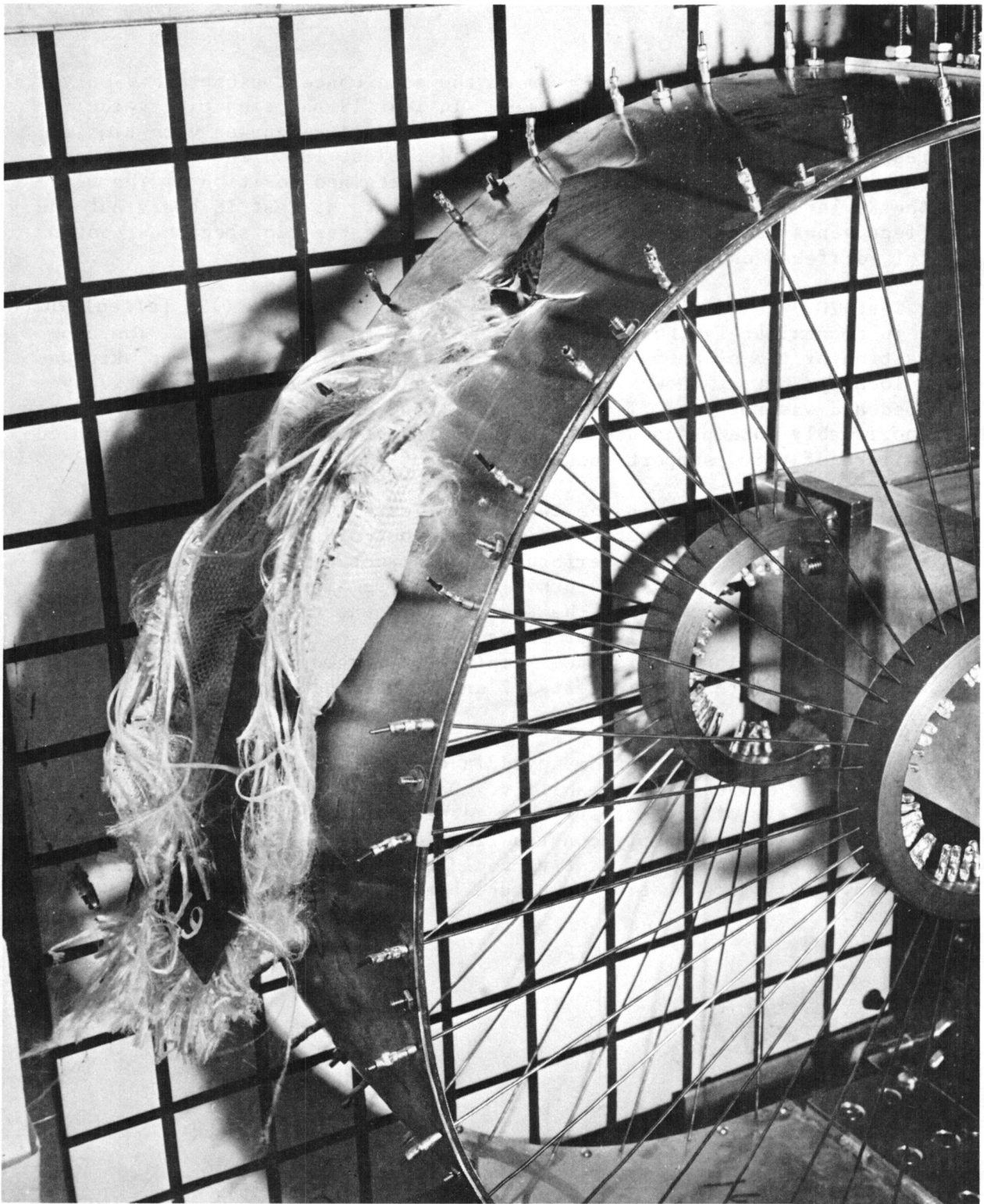


Figure 42. Test 19 - Exterior Closeup.

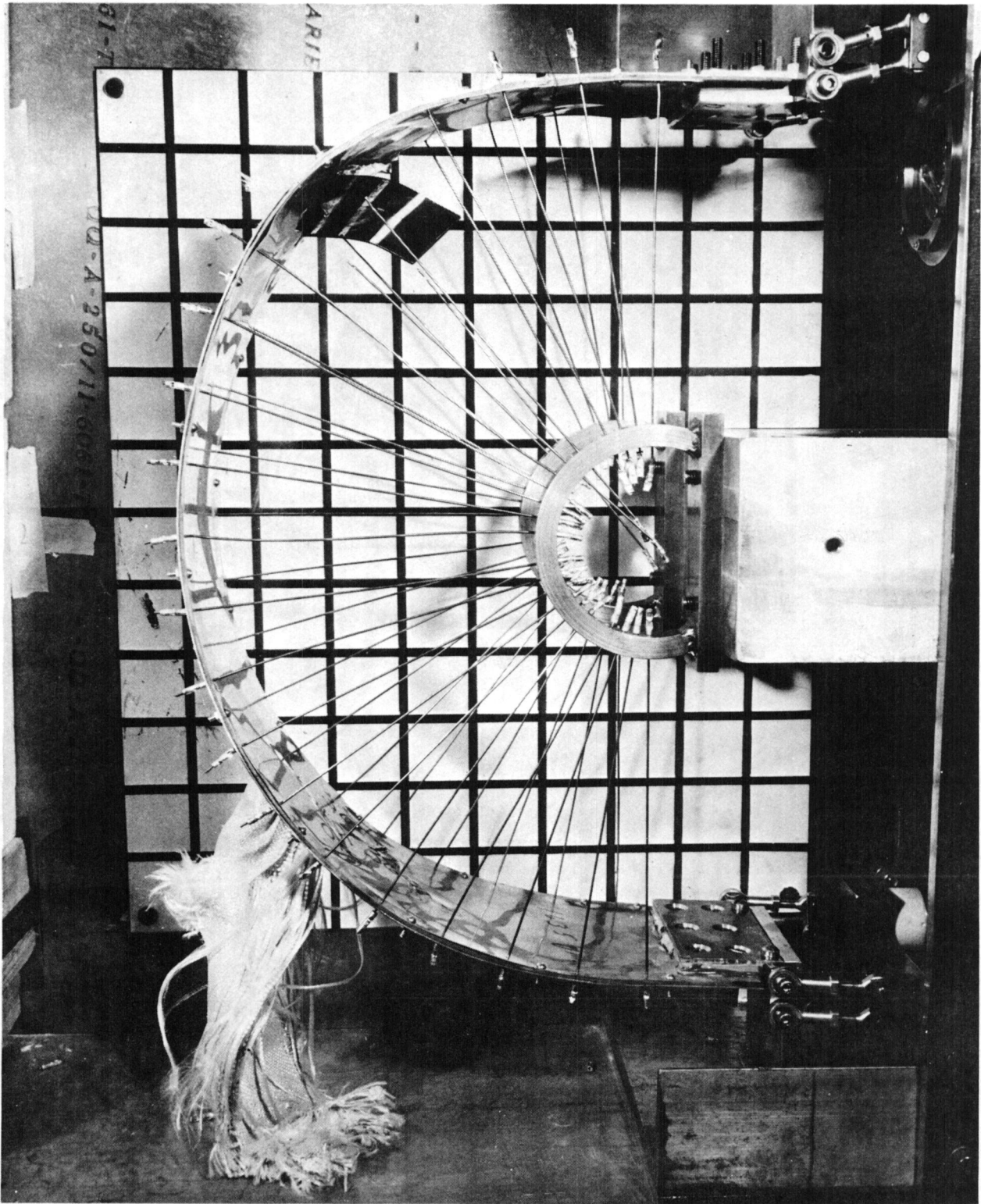


Figure 43. Test 20 - Side View.

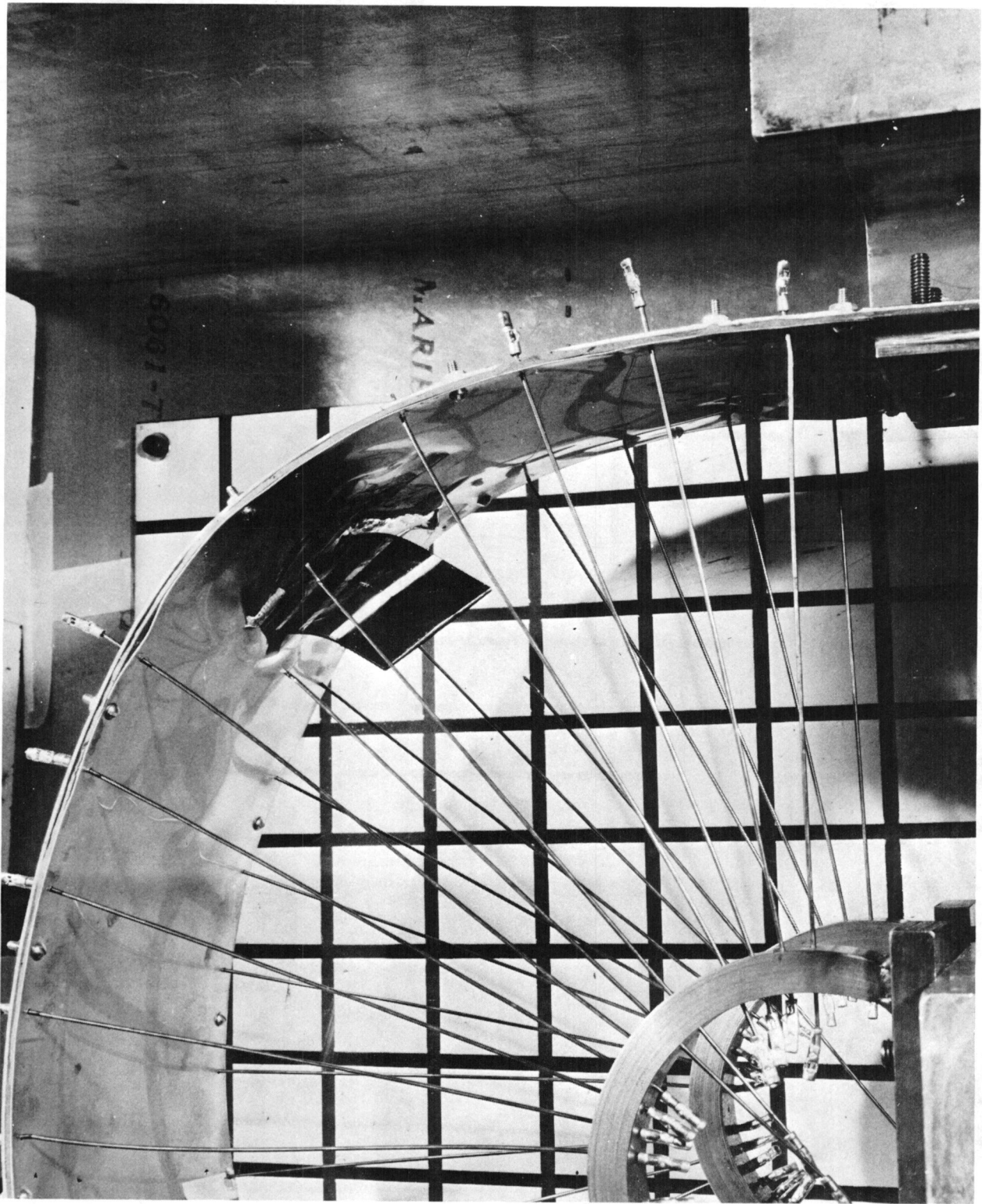


Figure 44. Test 20 - Interior Closeup.

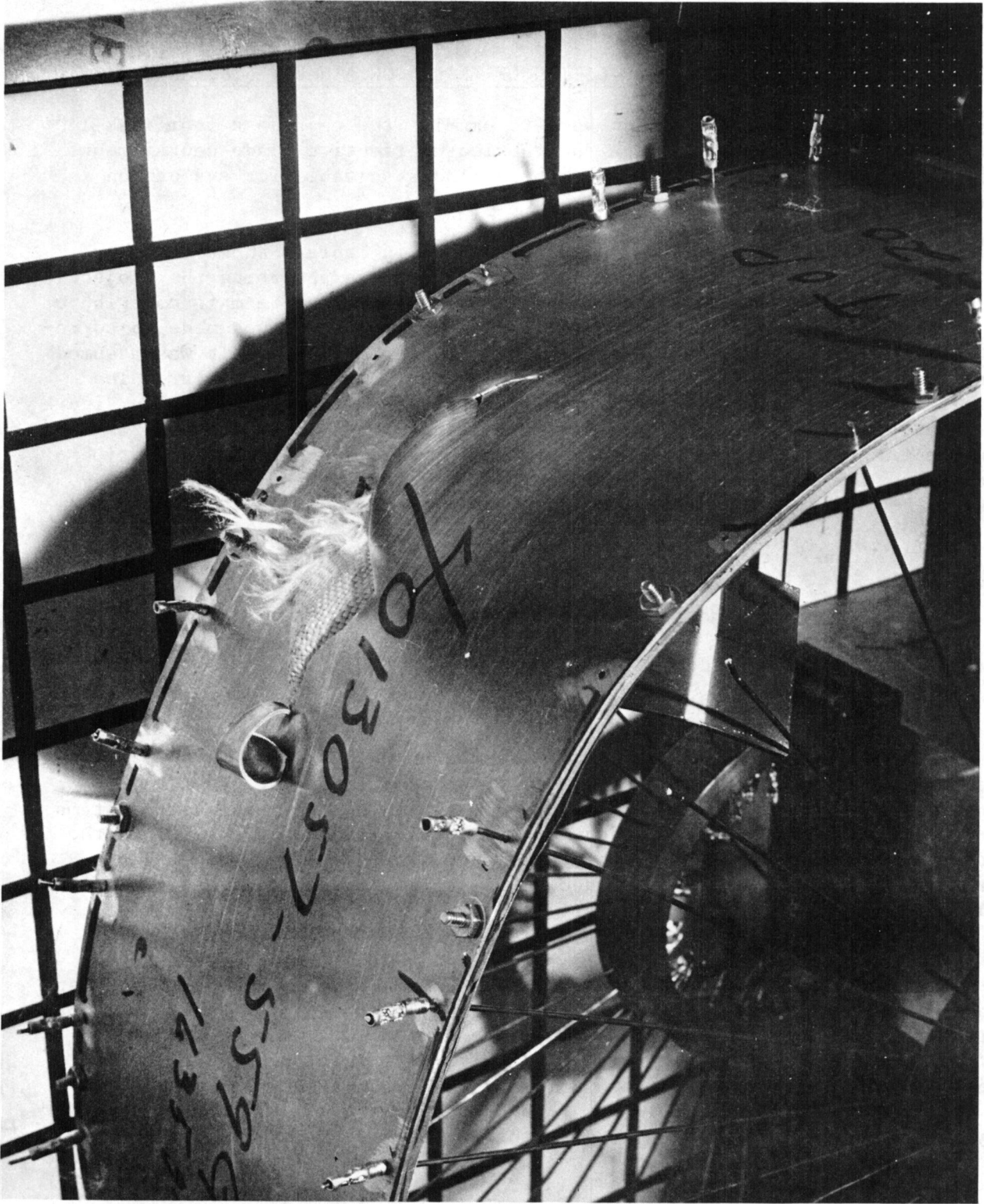


Figure 45. Test 20 - Exterior Closeup.

4.3 TASK III - DESIGN AND FABRICATION OF BLADE CONTAINMENT SYSTEMS

The objectives of this task were to examine the test data from Task II and, based on these data, design and fabricate effective blade containment systems for both titanium and superhybrid blades suitable for evaluation in a rotating disk test facility.

An examination of the test data summarized in Table I shows that the metal-faced/Kevlar designs were the most efficient in absorbing the projectile energy per unit weight of the containment system. Since the main contributor to the containment process is the Kevlar cloth, an attempt was made to correlate the Kevlar thickness with absorption of kinetic energy. It was assumed that the entire energy of the projectile was absorbed by the Kevlar. The results of Tests 5, 6, and 17 through 20 were then plotted as shown in Figure 46. Several likely-looking curves were faired through these data and a least-squares curve fit was performed for several typical expressions. The type of expression which seemed to best fit these curves was of the form $t = K(E)^n$, where:

t = thickness of Kevlar required for threshold containment

K = an arbitrary constant

E = kinetic energy

n = an arbitrary exponent

For most of the faired curves, the exponent n was very near to 0.5. Since the current state-of-the-art for metal containment cases involves the expression $t = K\sqrt{E}$, it was decided to use the same equation for the Kevlar systems by just using a constant, K , which matches the Kevlar test data. Since the two lower-right-hand points in Figure 46 were from tests that had exhibited marginal containment, it was decided to select a constant that best fits the remaining four data points. This resulted in the equation $t = 0.00341 \sqrt{E}$.

Since both titanium and superhybrid blades were to be released in the rotating rig tests, it was necessary to design containment rings of different thicknesses to account for the lighter weight (and thus lower energy) of the superhybrid blade. The same containment design concept was, however, used for both designs. This design consists basically of a thin steel inner liner, a number of plies of dry Kevlar cloth, and an aluminum backplate to hold the Kevlar in place. One variation of this concept was also designed in which a layer of honeycomb was placed between the inner steel liner and the dry Kevlar cloth. This feature was intended to provide a resting area out of the flow-path for the released airfoil. The depth of the honeycomb was based on that required to hide a TF34 airfoil section if it is oriented in its minimum projected profile position. Since this core had little structural function, it was chosen to be a relatively light 33.6 kg/m^3 (2.1 lb/ft^3) aluminum Flexcore. A schematic of the basic containment systems is shown in Figure 47.

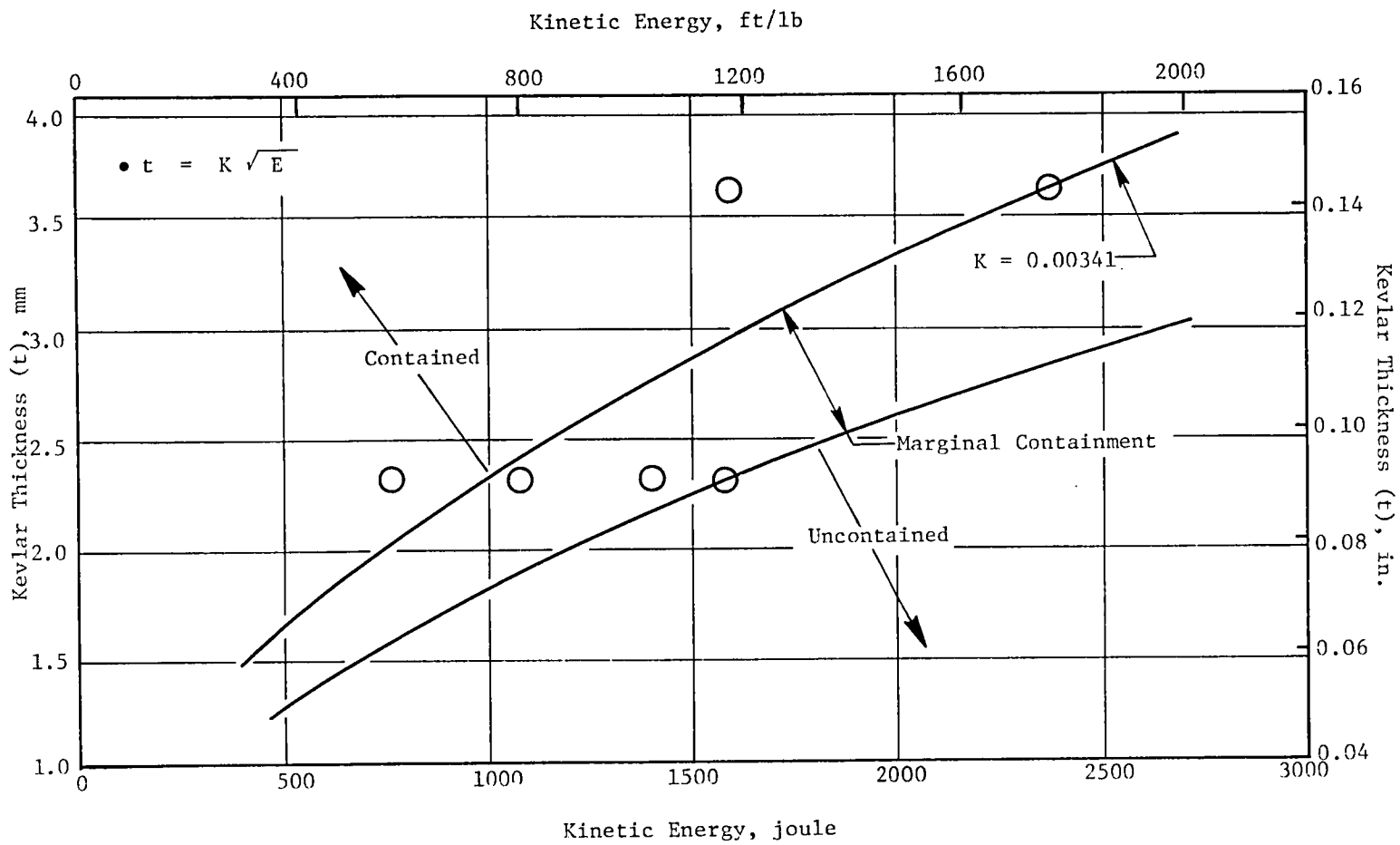


Figure 46. Thickness of Kevlar Required Versus Kinetic Energy Gas Gun Data.

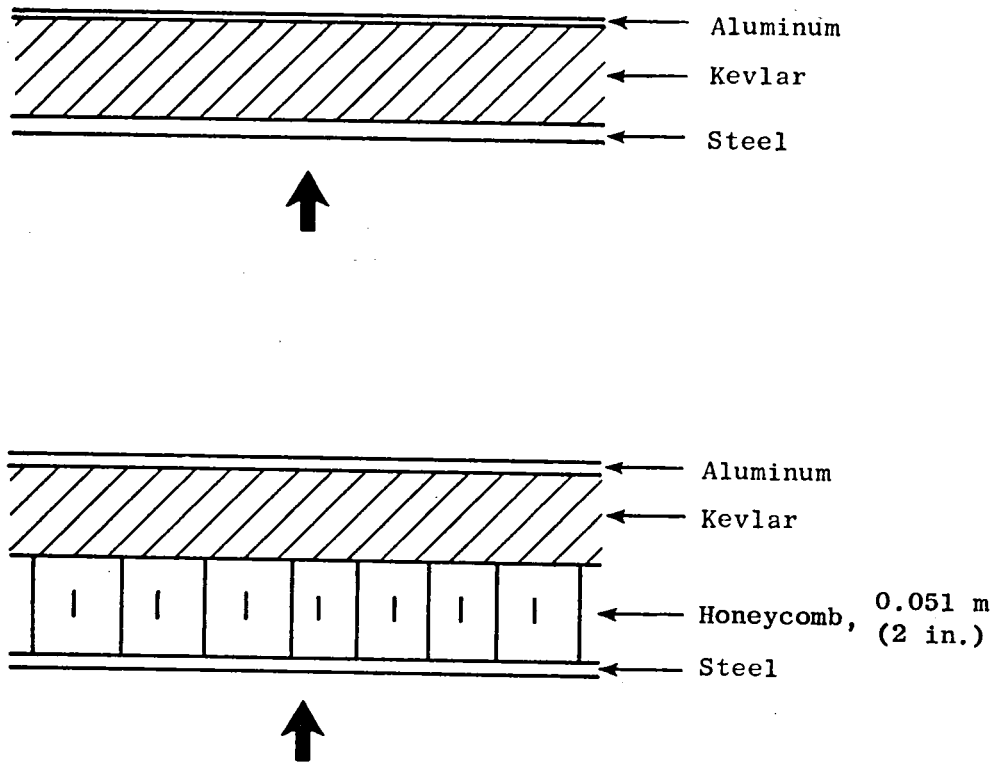


Figure 47. Steel/Kevlar Containment Concepts.

The amounts of Kevlar required to contain the titanium and superhybrid airfoils were calculated using the data presented in Figure 46. Based on these calculations, 22 plies of Kevlar cloth were assigned to each of the systems that would be providing threshold containment for the superhybrid blades, and 29 each to the containment systems for titanium blades. Each ply had a thickness of 3.3×10^{-4} m (0.013 in.). Since neither the steel liner nor the aluminum backplate contributes significantly to the containment process, they were arbitrarily chosen and were made as thin as was judged practical for manufacture and handling: steel liner, 5.1×10^{-4} m (0.020 in.) thick; aluminum backplates, 8.1×10^{-4} m (.032 in.) thick.

Based on just the basic containment (not including end and side attachments), the systems designed are lighter by 32% to 40% (depending on the use of honeycomb) compared to a steel containment ring designed to resist the same impact. These weight savings cannot be fully attained in practice, since the systems must be attached to other hardware and perform functions other than pure containment. This problem is discussed in somewhat more detail in Section 4.5.3.

4.4 TASK IV - TEST EVALUATION OF BLADE CONTAINMENT SYSTEMS

The objective of Task IV was to evaluate, through rotating rig tests, the fan blade containment systems selected from the Task II results and fabricated during Task III.

Although the subscale projectile tests are adequate for evaluating the relative containment potential of various structural configurations and are useful in determining the energy involved, the final proof of containment adequacy and determination of the penetration threshold must be performed in a rotating rig facility that more accurately simulates actual engine conditions.

In order to actually demonstrate such systems, it is necessary to choose a specific blade/rotor design against which to evaluate the designs. To choose a very large fan design, such as the CF6, would be very expensive in terms of containment structure costs, blade cost, and test cost. However, it is feasible to conduct the testing using a similar, but somewhat smaller, blade/rotor configuration which has characteristics similar to the large fan but is more convenient to test. Therefore, the blade/rotor configuration which was selected for the rotating evaluation of the containment designs was the TF34 first-stage fan. Its 1.1 m (44 in.) tip diameter makes this choice particularly convenient, for the fan is large enough to permit meaningful testing yet can be operated without requiring extensive modification to existing facilities.

4.4.1 Test Facility Description

An existing whirligig test facility consisting of a basic TF39 fan package was modified to adapt to a TF34 fan disk and to allow mounting of the containment shrouds.

This structure consists of a TF39 fan frame with the No. 1 and No. 2 bearing and sump systems and slave Stage 1 shrouding. With the exception of the slave Stage 1 shroud, the entire vehicle is soft-mounted.

The slave shroud with an inside diameter of 2.3 m (92 in.) is mounted to the ground. It is constructed of steel and serves as the mounting fixture for the containment shrouds being tested.

An environment chamber, or bell jar, is attached to the fan case. This provides the capability of operating in a helium atmosphere in order to reduce horsepower requirements and temperature buildup. The chamber also provides high-speed photographic capability and additional debris containment.

Witness plates are incorporated into the test facility to allow estimation of the residual energy of any fragments that defeat the containment system. The blade impact condition is established three ways: (1) by monitoring the rotor speed, (2) by determining the blade impacting weight by measuring blade specimen weight before and after test (subtracting the weight of the posttest retained blade root from the weight of the total blade specimen), and (3) by studying high-speed motion picture records of the impact. An automatic trip system is used to permit a continuous rapid acceleration. This eliminates the need to stabilize speed at the release point. This rapid acceleration reduces the time at speed and the heat/temperature buildup. The trip system consists simply of a revolution counter with two built-in relay "trips." The first trip is set such that, with the drive at maximum acceleration rate, the blade is released at a point established by prior checkout. The second trip is set to shut the drive system down to prevent excessive vehicle damage and/or overspeed. To achieve the maximum acceleration rate, the drive is operated at maximum-rated motor current.

In order to control the impact point of the blade specimen relative to the containment shroud, the explosive charge is detonated in a rotor speed at a circumferential position that will permit the blade to impact in the containment shroud preselected target location. In addition, the camera and lights are activated to catch the event. An electronic "black box" called the whirligig triggering system, designed and built to satisfy these requirements, is utilized. It uses a very precious "clock" to permit timing the detonation of the explosive charge. This timing can be varied and is set to allow time for the flash bulbs to reach full brilliance and account for the angular position of the blade relative to a 1/rev indicator on the rotor.

The basic test setup and assembly of the soft-mounted test vehicle are shown in Figure 48.

The blade specimens are released at the airfoil root by an explosive charge. By precise timing, two blade specimens 180° apart can be released together. Rotor imbalance is thus minimized, and two specimen tests are accomplished in a single whirligig test operation. Each 360° containment shroud is constructed as two 180° segments to provide two combinations of containment design in each 360° shroud, minimizing the number of physical spins in the whirligig facility.

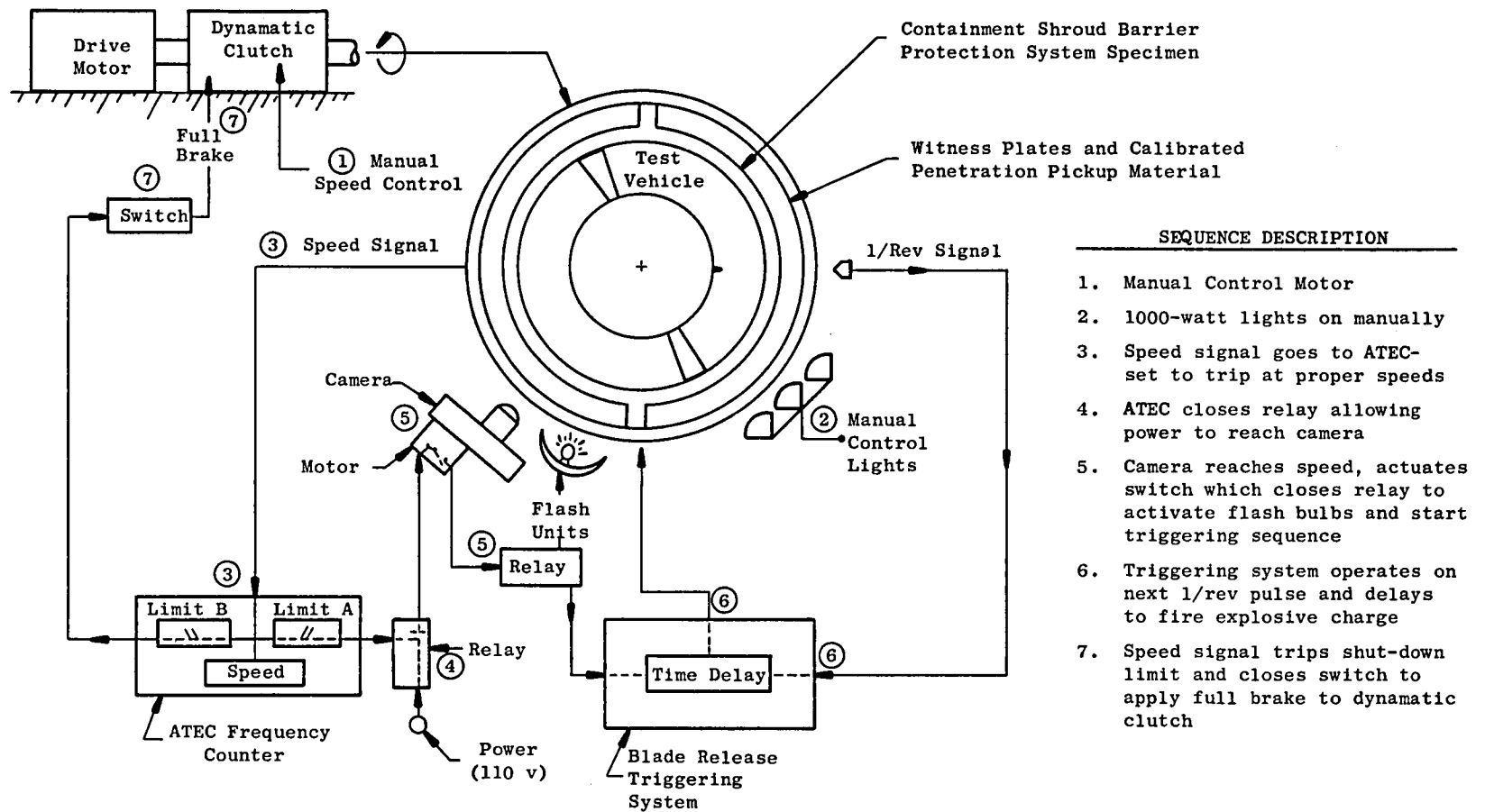


Figure 48. Basic Whirligig Test Setup.

Two types of blades were used in the rotating tests. One was the standard titanium TF34 blade (Figure 49) which embodies typical current fan blade design practices. The other was a superhybrid blade (Figure 50) consisting of a titanium pinned root and leading edge spar, a graphite/epoxy shell, and a titanium foil outer covering. This configuration was intended to represent potential future blade construction.

4.4.2 Test Results

The four rotating tests yielded eight data points: four for the titanium blades, four for the superhybrid. The original test plan is shown in Table III. Since 5400 rpm is the maximum capability of the test rig when the TF34 rotor is installed, it was decided to alter this test plan and run Tests 1 and 3 at 5000 rpm instead of at the 5400 rpm maximum. This change provided the option of running Tests 2 and 4 at higher energy levels than Tests 1 and 3. Based on the results of the revised Test 1, the entire test plan was revised to the version shown in Table III. The revision was prompted by the service interaction anticipated between any following blades and those casings which had no honeycomb nesting area. A description of the test results is given below, along with the rationale for the selection of the test parameters chosen for Tests 2, 3, and 4.

Test 1

Test 1 was run in accordance with the revised test plan shown in Table III. The 180° containment cases were mounted in the way shown schematically in Figure 51.

Two superhybrid test blades were mounted 180° apart in a standard TF34 disk. Three standard TF34 titanium blades were mounted behind each test blade, making a total of eight blades in the rotor. The test blades were to be simultaneously released by explosive charges so that one blade would impact each containment system. Three cameras were used to record the event. Both test blades had the standard TF34 titanium root section and platform. Above the platform, the blades consisted of a titanium leading edge spar and a graphite/glass/epoxy shell. Over the entire airfoil section was bonded an 8×10^{-5} m (0.003 in.) titanium foil. The weight of the released airfoil was calculated to be 0.35 kg (0.77 lb) with a c.g. radius of 0.4087 m (16.09 in.). At the intended release speed of 5000 rpm, this would result in a per-blade kinetic energy of roughly 8100 J (6000 ft-lb). The containment systems were designed to provide threshold containment. Penetration of the aluminum backsheet would be acceptable as long as the energy of all loose objects would be completely dissipated.

At 5000 rpm, one of the two charges on each blade fired at the proper circumferential location. Although the composite portions of the blades left quickly, neither spar was completely severed. One spar separated on the second revolution and the other on the sixth revolution after it interacted with Kevlar that was being pulled into the right side of the flowpath by the blades. Both spars went into the right containment half. As Kevlar continued to be pulled out of the right-hand containment system, its interaction

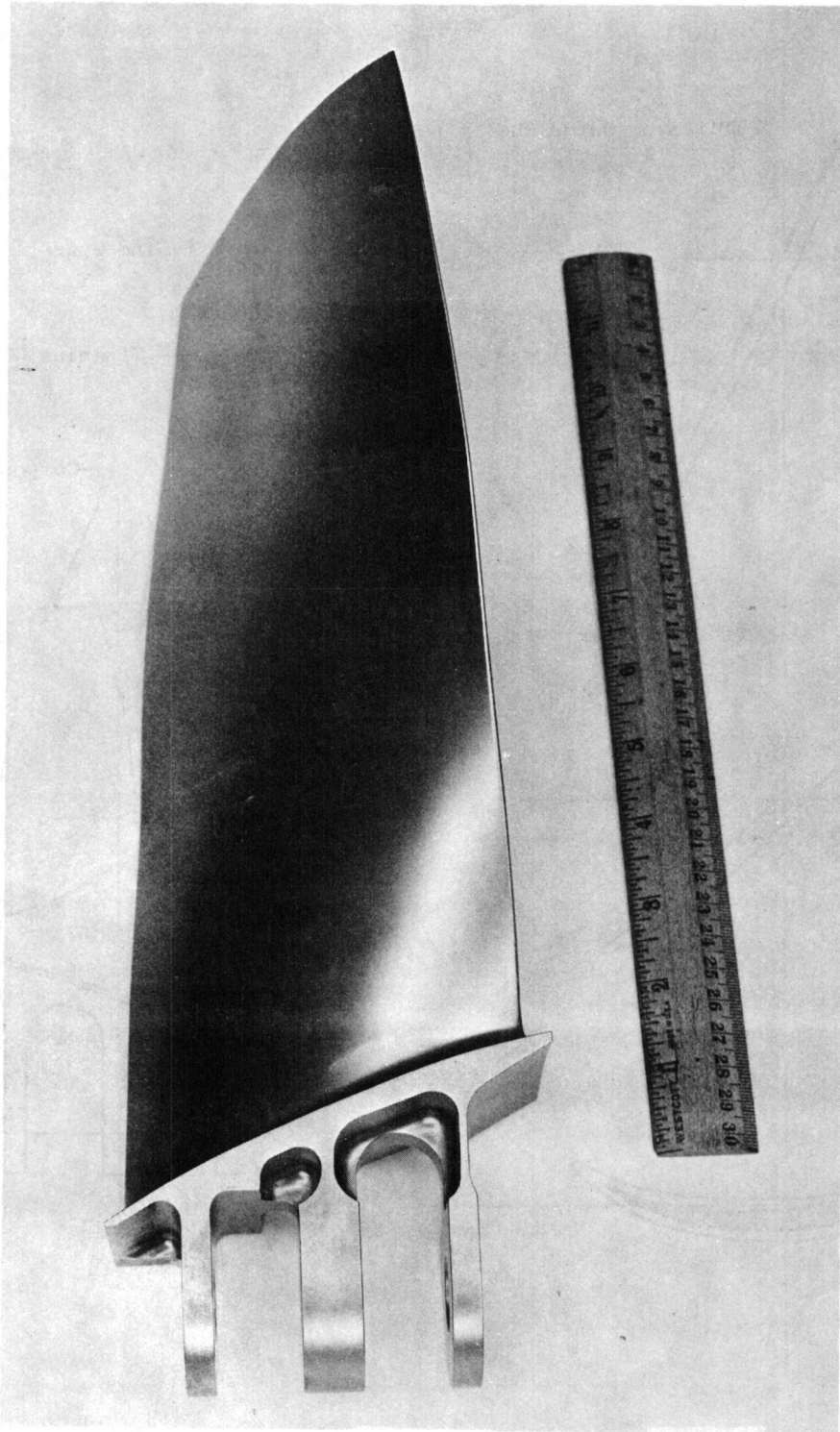


Figure 49. TF34 Titanium Blade.

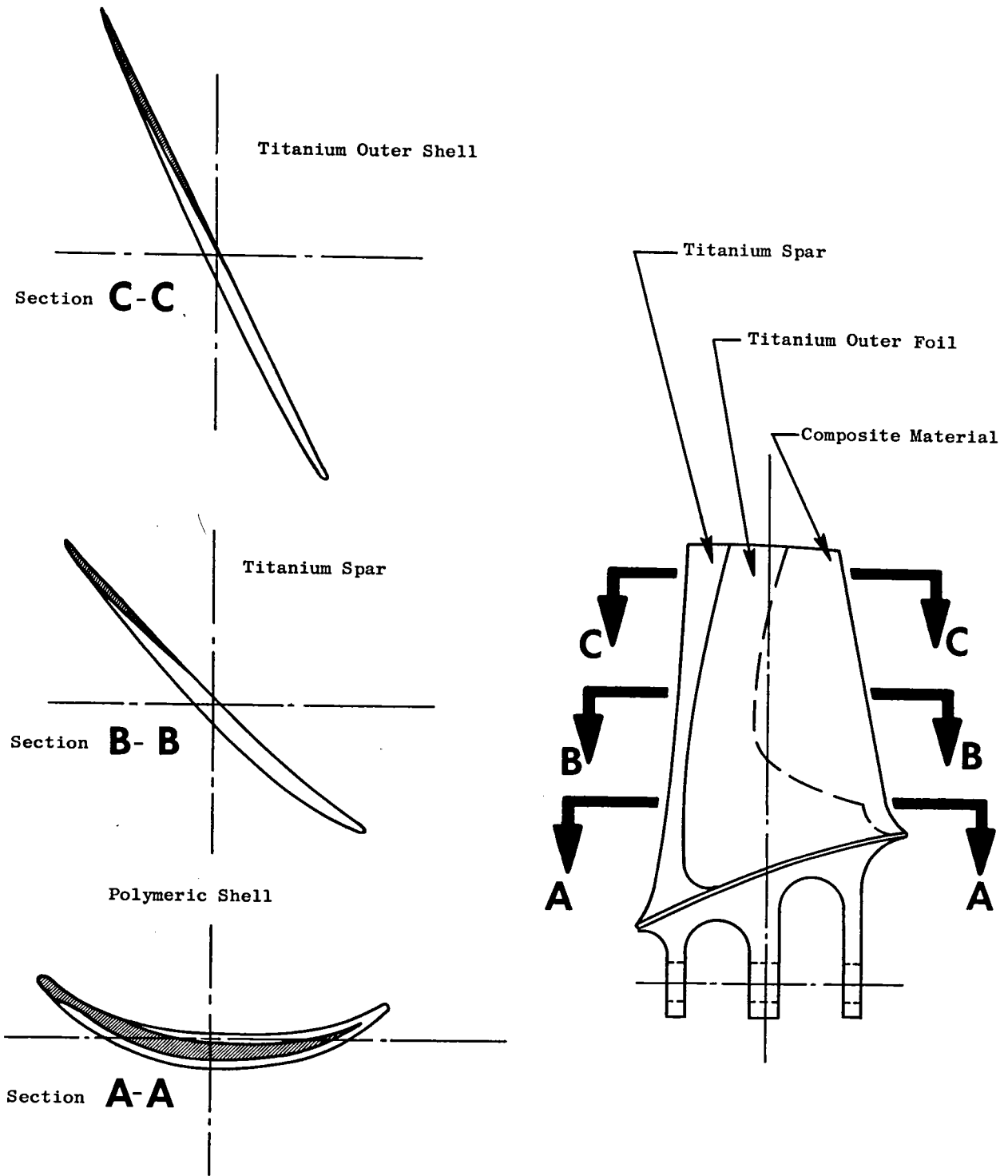


Figure 50. TF34 Superhybrid Titanium Composite TiCom Blade.

Table III. Planned Tests.

<u>Test No.</u>	<u>Left Half</u>	<u>Right Half</u>	<u>No. of Kevlar Plies</u>	<u>With Honeycomb</u>	<u>Without Honeycomb</u>	<u>Fan Speed, rpm</u>	<u>Type of Blade</u>
1	X		22	X		5000	Composite Superhybrid (TiCom)
		X	22		X	5000	Composite Superhybrid (TiCom)
2	X		22	X		TBD	Composite Superhybrid (TiCom)
		X	22		X	TBD	Composite Superhybrid (TiCom)
3	X		29	X		5000	Titanium
		X	29		X	5000	Titanium
4	X		29	X		TBD	Titanium
		X	29		X	TBD	Titanium

5.1 m (2 in.) of
 33.6 kg/m^3 (2.1 lb/ft^3)
Aluminum Honeycomb

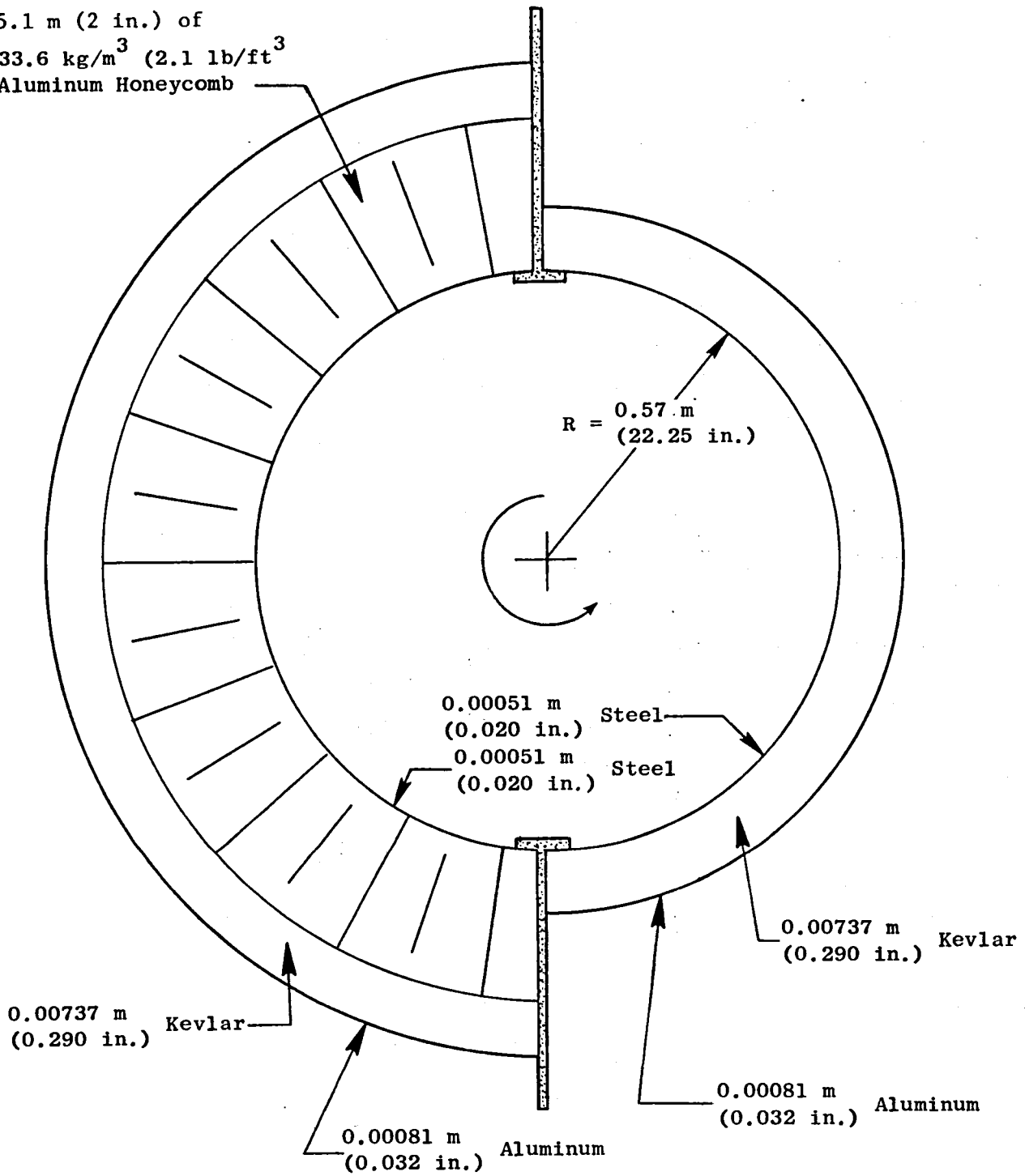


Figure 51. Composite Containment System - Rotating Test 1.

with the remaining titanium TF34 blades became severe enough to fracture one of these blades at its root. This blade, weighing 0.59 kg (1.3 lb), entered the center of the as-yet-undamaged, left-hand containment system at 4630 rpm and was contained. Its calculated energy of 11,970 J (8830 ft-lb) was well above the calculated containment threshold capability. All of the titanium projectiles punctured the steel front sheet and locally ruptured the aluminum outer wall as Kevlar bunched up ahead of the projectiles. There were no marks on the witness plates behind the containment rig. The two casings are shown in Figure 52 as they appeared after being removed from the test rig. The outer wall of the honeycomb casing is shown in more detail in Figure 53.

Test 1 graphically demonstrated two very important requirements for containment concepts of this type. First, it is now clear that a nesting area, or at least some separation between the flowpath and the dry Kevlar, is required to prevent the Kevlar from interacting with the remaining rotor blades. Second, a rigid backsheet must be bonded to the honeycomb not only to provide casing stiffness but to prevent the dry Kevlar from falling into the flowpath when a blade impact removes some of the honeycomb that is holding it in place. As previously mentioned, the results of Test 1 led the remainder of the test plan to be modified to the conditions shown in Table IV.

Test 2

Setup for Test 2 was identical to that for Test 1 except that there were no following blades. This was done to isolate the containment process and provide a good comparison with the gas gun tests. The test setup is shown in Figure 54. The containment casings can be identified by the dark axial stripes. Upon release, both composite shells separated from the spars and were contained. The spars remained attached for several revolutions because, again, only one cutting charge went off on each blade. This occurred despite pregrooving of the spars and attempts to improve the connection between the detonator and shaped charge. Upon release, the spar that hit the right side (the side with no honeycomb) was stopped (Figure 55) and rebounded back into the flowpath. The other spar hit the left side (Figure 56), sliced through the 0.05 m (2 in.) thick honeycomb, interacted with the Kevlar, and stopped within its own length, completely nested outside the flowpath. Figure 57 depicts both casings after removal from the facility.

Test 3

The third rotating test was conducted on a lightweight Kevlar containment system that utilized all-titanium blades. The basic containment system was similar to those of tests previously conducted except that more Kevlar was used to account for the greater energy of the titanium blade. In addition, based on the results of Test 1, two plies of Kevlar/epoxy were bonded to the back of the 0.05 m (2 in.) thick honeycomb separating the 5.1×10^{-4} m (0.020 in.) steel face from the 29 plies of dry Kevlar. This was done to increase the casing stiffness and keep the casing round after impact. Four following titanium blades were mounted behind each of the two test blades.

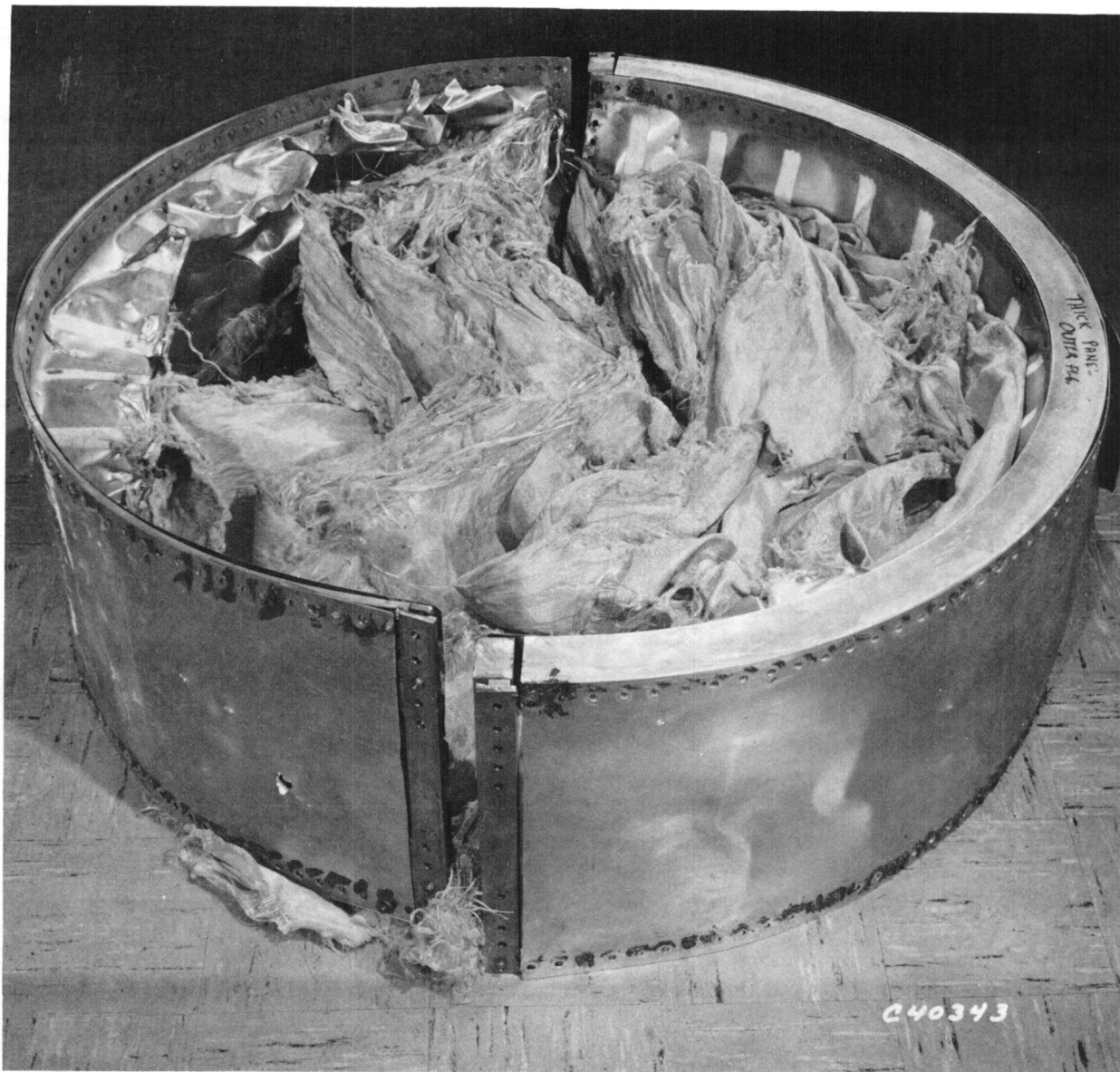


Figure 52. Composite Casings Following Rotating Test 1.

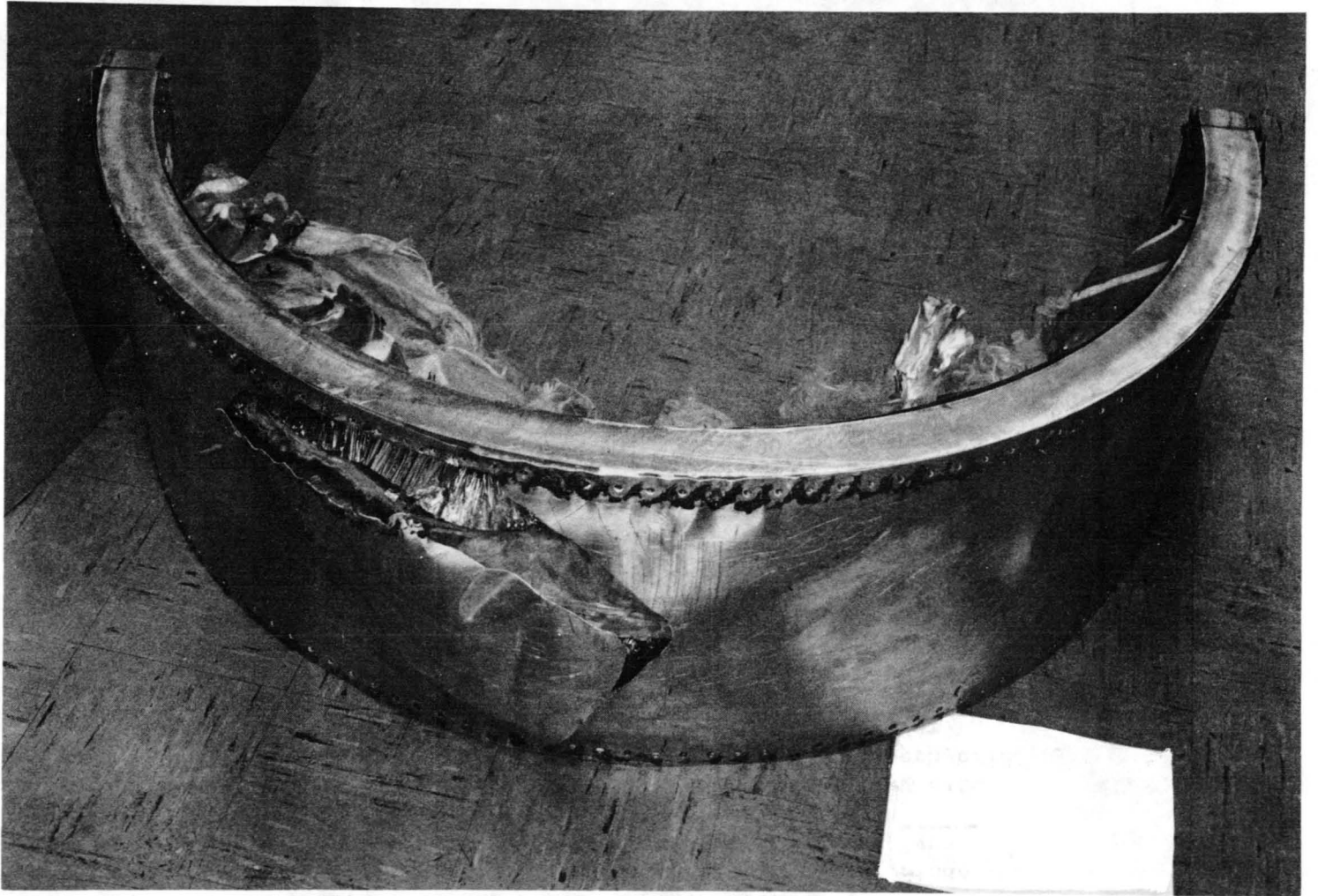


Figure 53. Honeycomb Casing Showing Outer Wall Following Rotating Test 1.

Table IV. Revised Test Plan.

<u>Test No.</u>	<u>Left Half</u>	<u>Right Half</u>	<u>No. of Kevlar Plies</u>	<u>With Honeycomb</u>	<u>Without Honeycomb</u>	<u>Fan Speed, rpm</u>	<u>Blade Type</u>
1	X		22	X		5000	Composite Superhybrid (TiCom)
		X	22		X	5000	Composite Superhybrid (TiCom)
2	X		22	X		5000	Composite Superhybrid (TiCom)
		X	22		X	5000	Composite Superhybrid (TiCom)
3	X		29	X		5000	Titanium
		X	29	X		5000	Titanium
4	X		29		X	5000	Titanium
		X	29		X	5000	Titanium

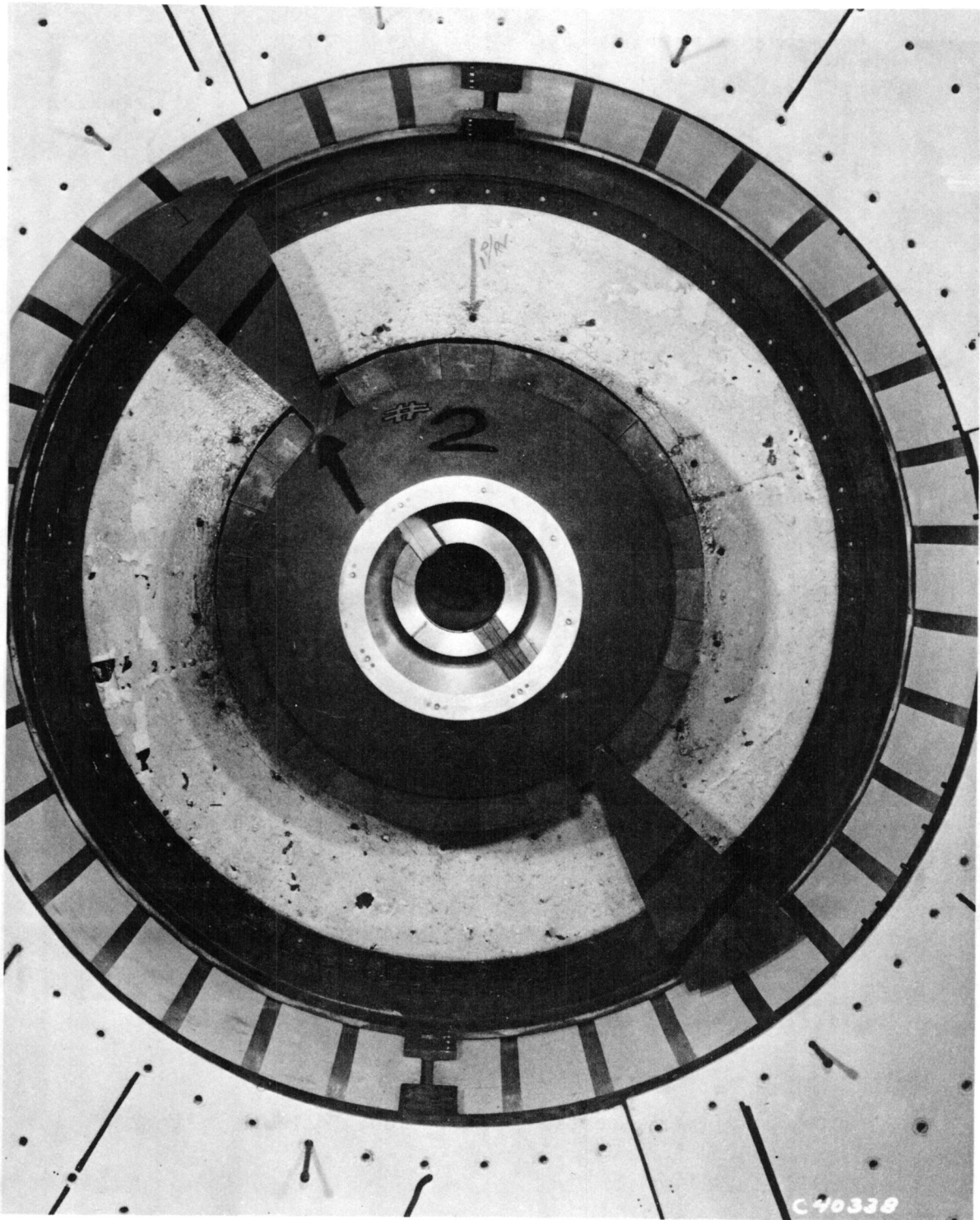


Figure 54. Composite Containment System - Test 2, Before Test.

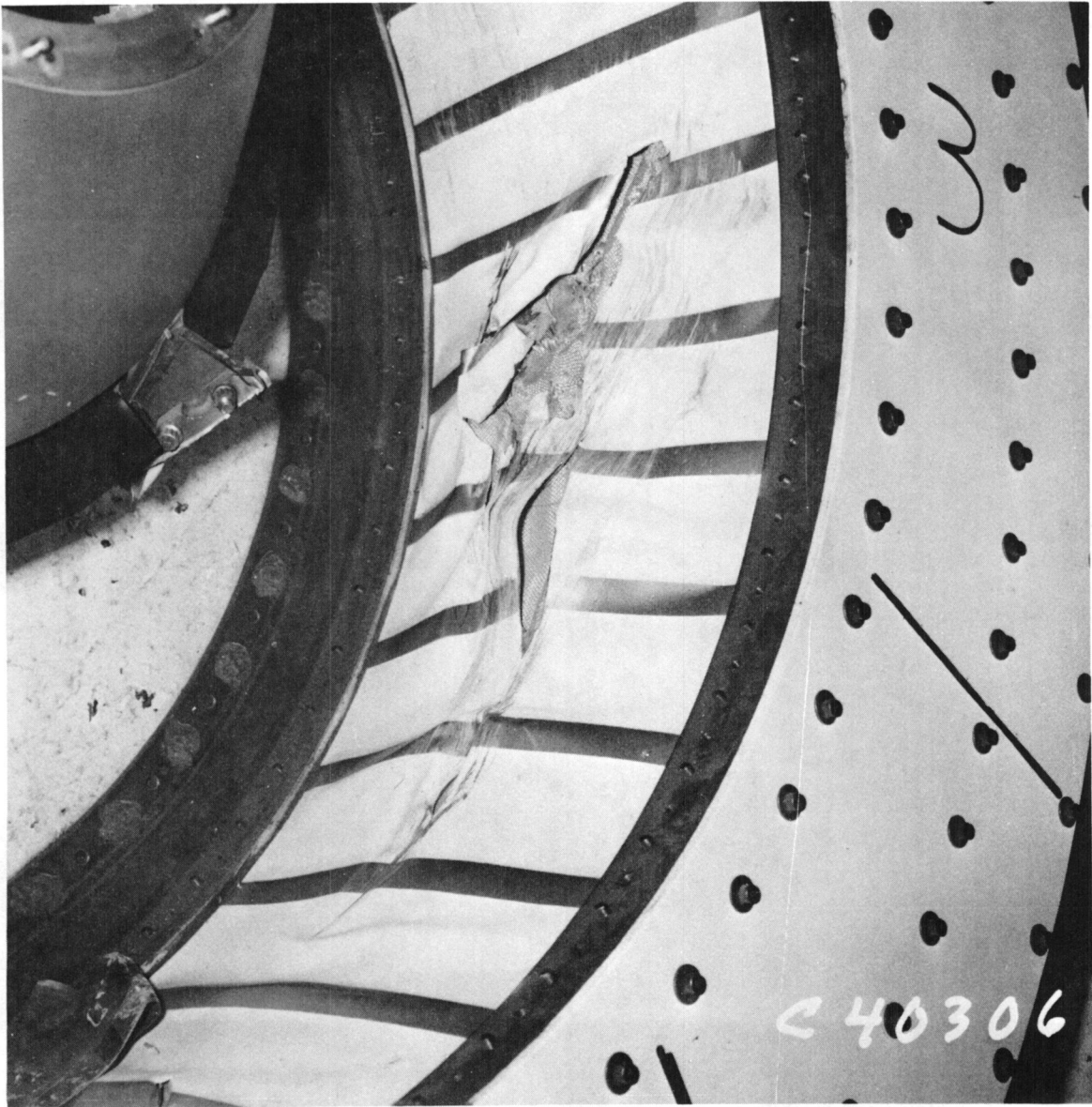


Figure 55. Impact Location, Right Side, Following Test 2.

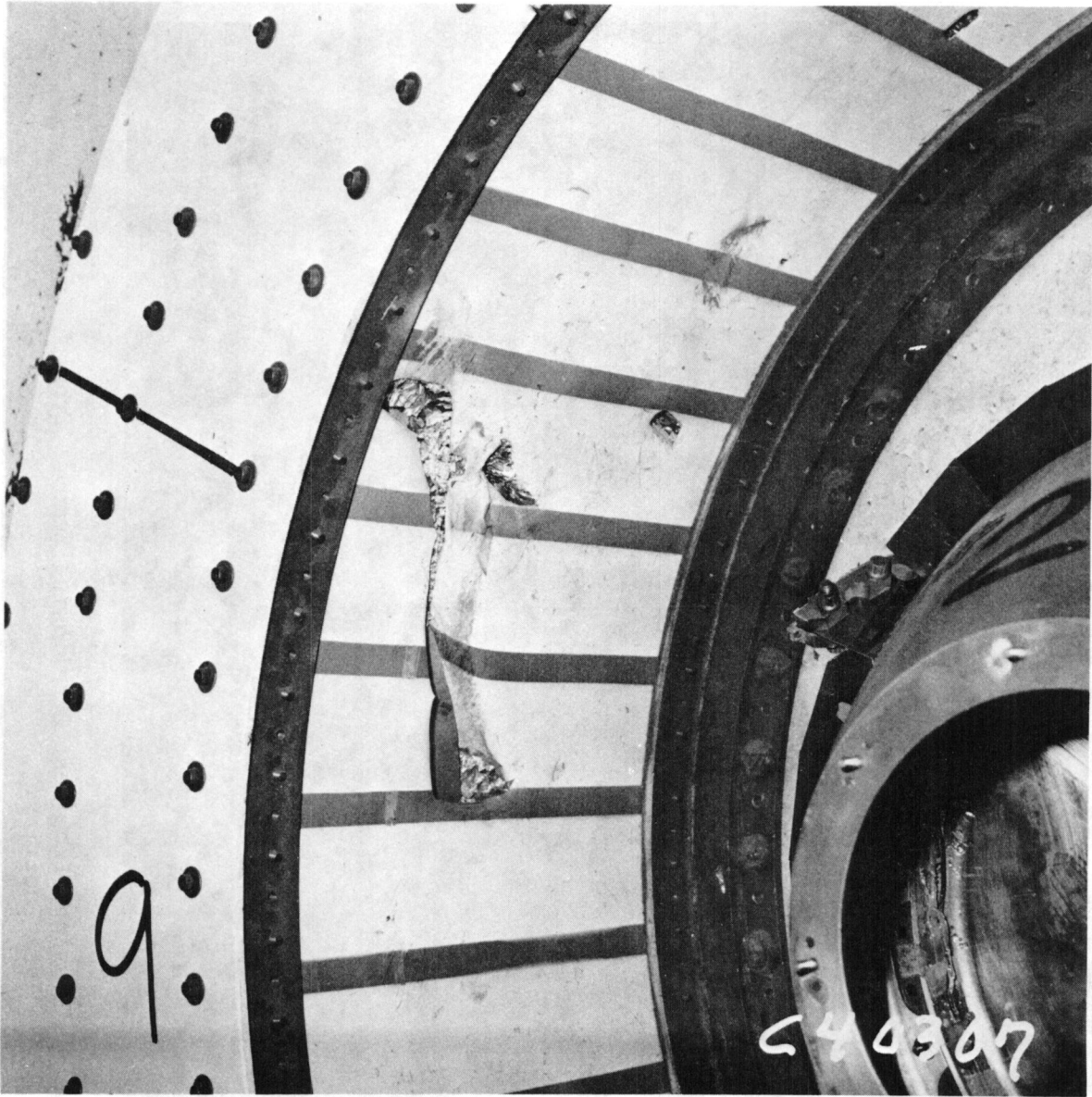


Figure 56. Impact Location, Left Side, Following Test 2.



Figure 57. Casings From Test 2 Following Removal From Test Facility.

The blades were released at the root at 5000 rpm. This resulted in a c.g. energy of 13,970 J (10,300 ft/lb) for each blade. The blades penetrated the steel facing and tore the honeycomb. The two plies of Kevlar/epoxy were cut but were not significantly penetrated. The blades were both completely nested in the honeycomb area (Figure 58) and were stopped. The casing remained round; very little of the precured Kevlar/epoxy becoming exposed in the flowpath on one side. Following blades suffered minor damage. The first two following blades had about 1 inch of their leading edge tips bent over. The remainder of the blades suffered no apparent damage. The rotor deceleration was very smooth and the rotor could be turned freely by hand. Casing interaction with the rotor was minimal. This test was considered to be extremely successful.

A closeup of one of the cases is shown in Figure 59. The honeycomb was scraped off the precured Kevlar/epoxy in the area of impact and shoved ahead of the blade. The high-speed movies taken during the test show that the root of the released blade contacted the following blade at about its midspan. This contact rotated the released blade root so that the blade went into the containment system root first. The portion of the blade visible in Figure 59 is, therefore, the trailing edge tip. The rest of the blade is buried in the nesting area.

One of the 180° containment rings tested was disassembled for more detailed examination. Figure 60 shows the containment ring with the steel inner liner (plus some honeycomb) removed. The smooth surface visible on the left side is the precured Kevlar/epoxy. It is apparent from the condition of this surface that the bond (which was merely wet resin) between this material and the core was very poor. The somewhat ragged-looking material in the impact area is torn Kevlar/epoxy. This area can be seen more clearly in Figure 61 where the remainder of the honeycomb has been removed. The precured Kevlar/epoxy has been peeled back in Figure 62 to show the first layer of dry Kevlar. This layer was torn slightly but evidenced relatively little damage.

Since the first dry Kevlar layer (of 29 layers) was damaged so little, it was apparent that the Kevlar thickness required for providing threshold containment had been conservatively calculated from the gas gun tests.

Test 4

Neither of the two remaining prefabricated containment systems built for this test series had provisions for blade nestings. It was expected, therefore, based on the results of Test 1, that any following blades would interact extensively with the dry Kevlar cloth. To limit this interaction and prevent damage to the test rig, only one following blade was mounted behind each test blade for this test. The test setup is shown in Figure 63. The main purpose of this test was to demonstrate, on a one-to-one basis, the advantages of nesting the blade, as demonstrated in Test 3, over the non-nested configuration of this test. Except for the nesting feature, these containment systems were the same as for Test 3.



Figure 58. Composite Containment System Following Impact Test 3.

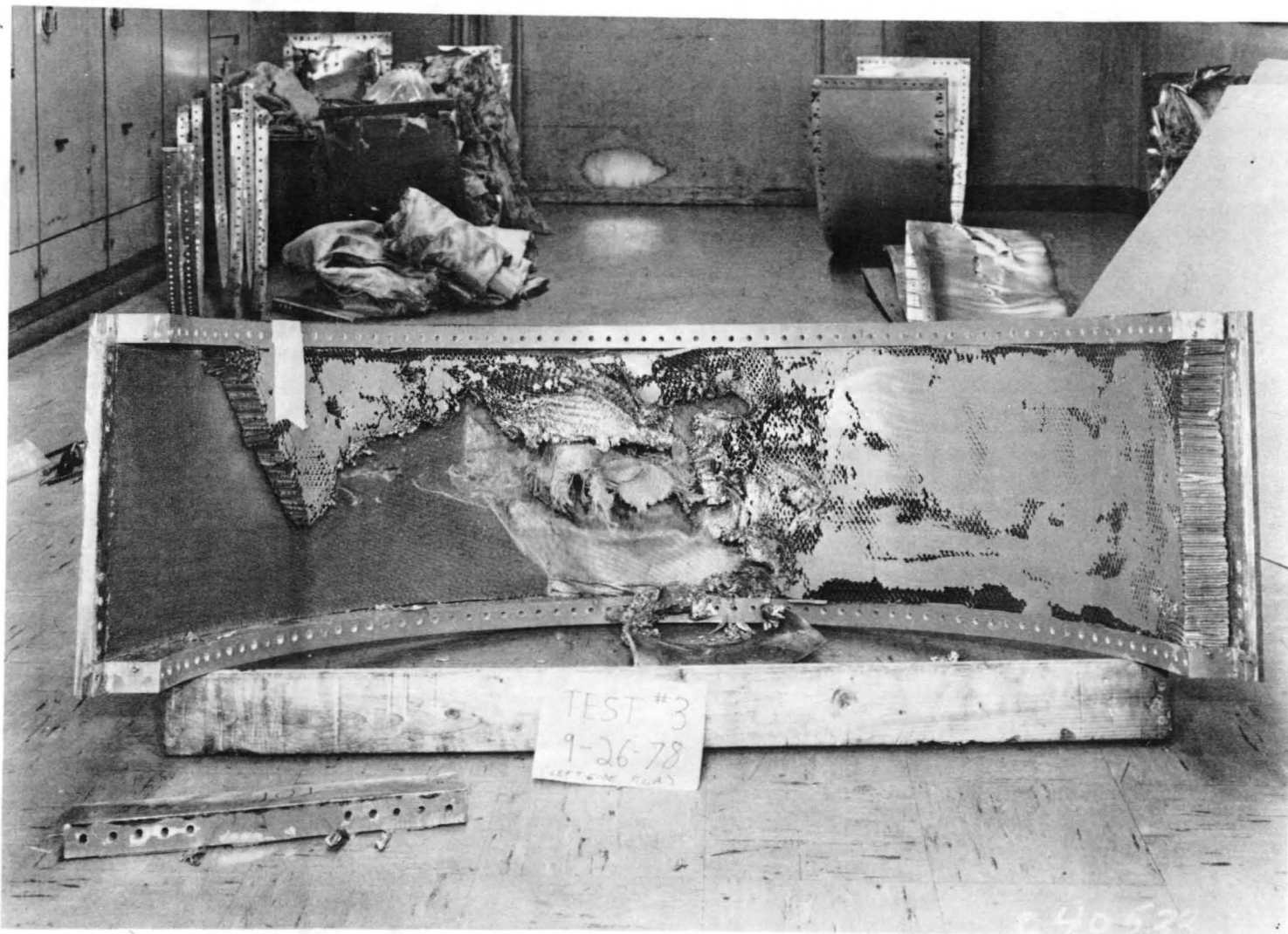


Figure 59. Impact Location Showing Nested Blade - Test 3.

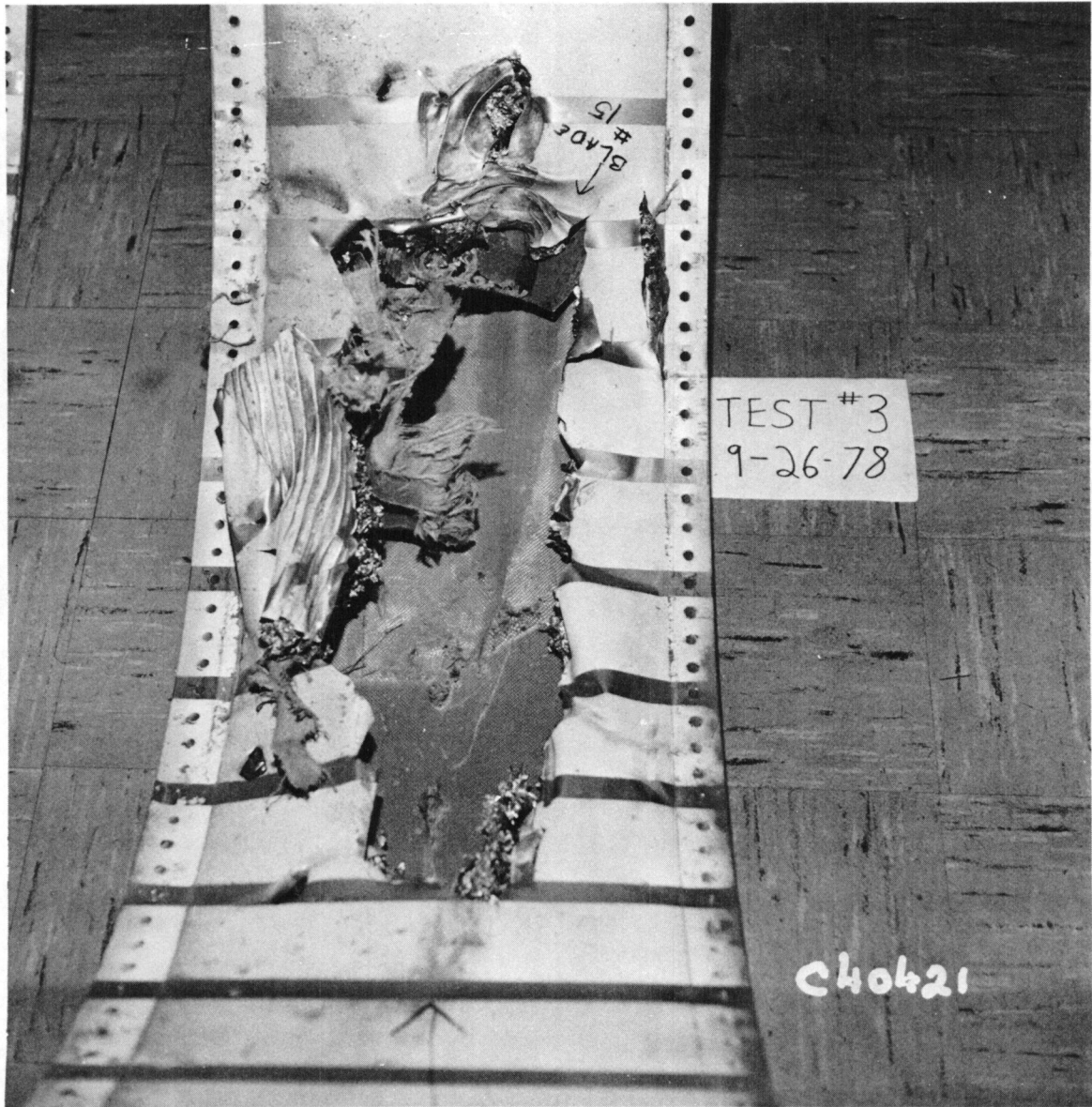


Figure 60. Containment Half-Ring With Steel Inner Liner Removed Following Test 3.

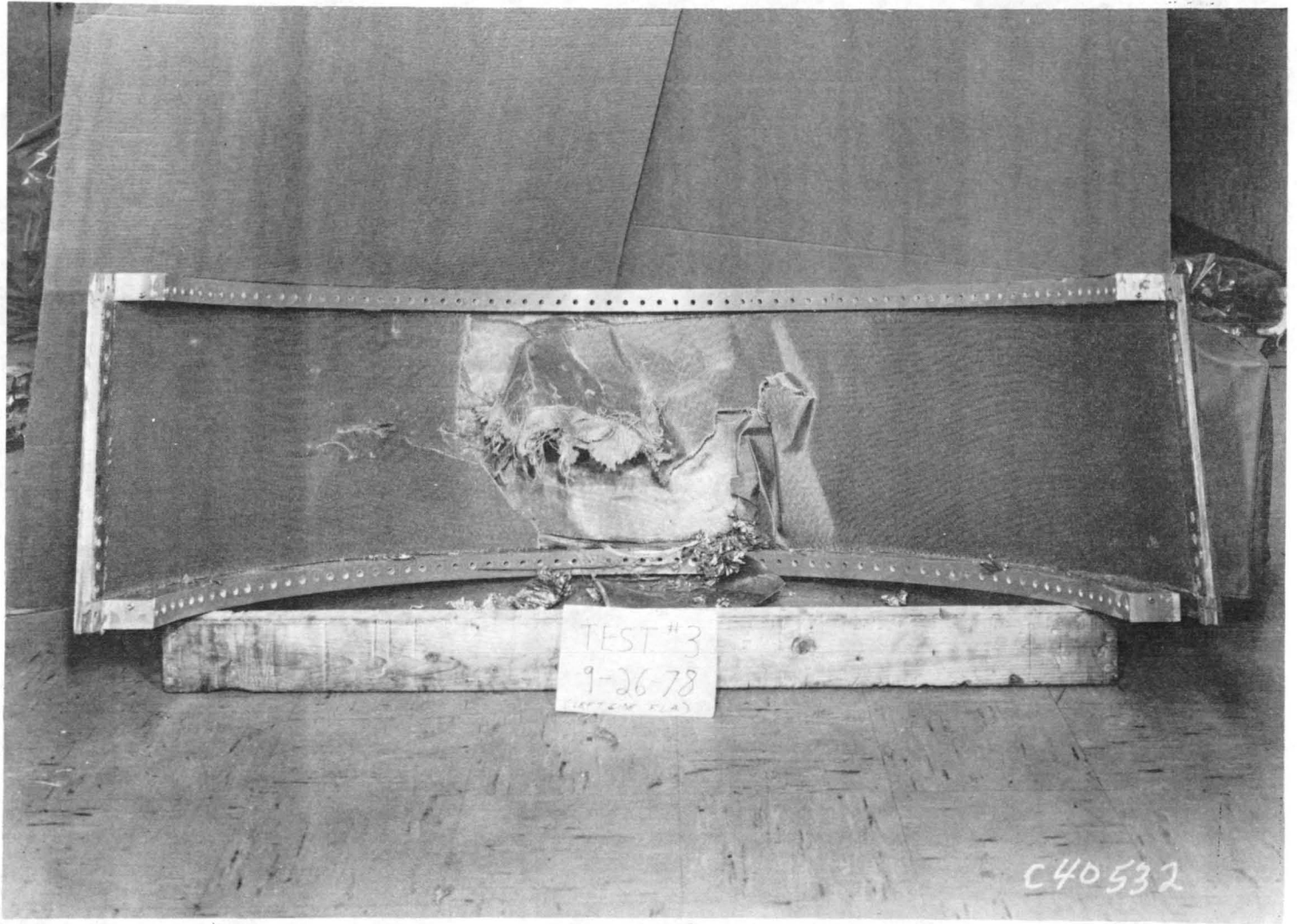


Figure 61. Test Part with Honeycomb Removed Showing
Precured Kevlar/Epoxy.

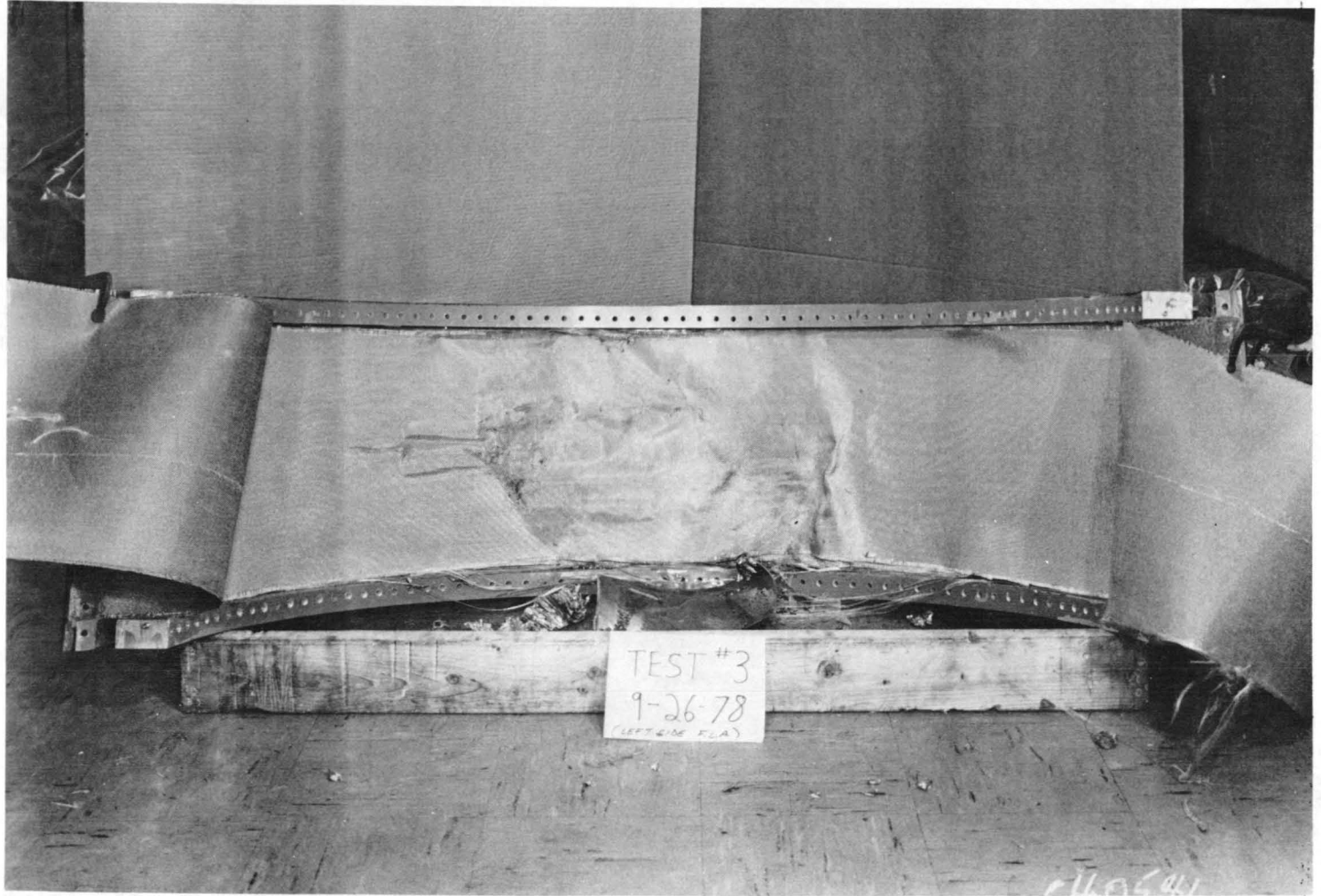


Figure 62. Test Part Showing Dry Kevlar with Precured Kevlar/Epoxy Peeled Back.



Figure 63. Whirligig Test Setup Before Test 4.

The test blades released as planned and went into the containment system, pushing the dry Kevlar cloth through the aluminum but not actually failing the Kevlar. There was no apparent interaction with the blade immediately following the test blade on each side. The test blades then rebounded from the containment system and were struck by the blades that were following the opposite released blade; severe interaction ensued. The Kevlar cloth was then dragged into the flowpath by the following blades, causing an interaction severe enough to fail the titanium blades at the base of the airfoil. One of these blades went into the containment system that had little Kevlar left in it, went through the system, and impacted the first 1.3×10^{-3} m (0.050 in.) steel witness plate. The witness plate was scarred but not penetrated. The Kevlar in the flowpath wrapped itself around the shaft, causing a very rapid deceleration. The condition of the containment casings after the test is shown in Figure 64. Test demonstrated the need for a nesting area in these types of containment systems.

This completed the testing portion of the program.

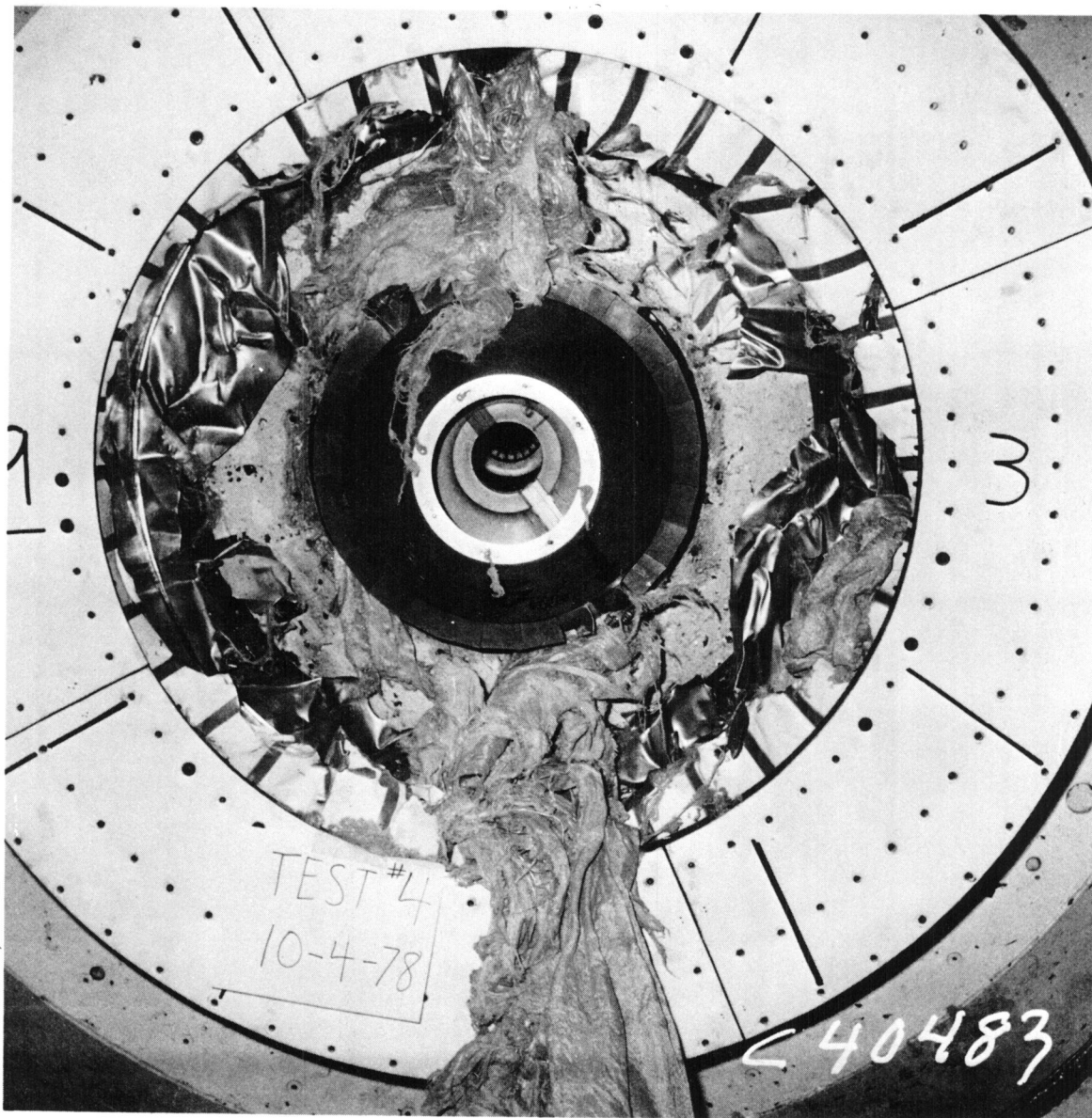


Figure 64. Containment Test 4 Following Impact.

4.5 TASK V - FORMULATION OF BLADE CONTAINMENT SYSTEMS REQUIREMENTS

The objective of this task was to correlate the test results in Tasks II and IV with the analysis developed under Task I. In addition, a design criterion was established which, along with the test data generated by the program, was used to produce a preliminary design of a full-scale CF6-size containment system.

4.5.1 Correlation of Test Results with Analysis

As it presently exists, the analysis discussed in Section 4.1 uses assumed constant values of the structural resistances σ_{t_n} , σ_{r_n} , and σ_{l_n} and of friction coefficients. Although these values may be based on the actual materials and construction of the structure, in general, the actual resistances for a given construction are not known. This is because of the highly dynamic material effects, extreme material strain levels, and three-dimensional stress states involved in the containment process. Ordinary stress-strain data and strength of materials theory cannot be effectively applied in most instances.

Effective average values of σ_{t_n} , σ_{r_n} , and σ_{l_n} and their associated friction coefficients may be estimated, however, by coupling experimental data obtained from gas gun and whirling tests with analysis results in the manner described previously. Experimental data include the observed x , y , θ , ϕ , \dot{x} , \dot{y} , $\dot{\theta}$, and $\dot{\phi}$ blade interaction values that can be measured from quality, high-speed motion photographs. Additional data, obtained from examination of the impacted structure, include blade path through the containment structure, depth of nesting, final x , y , θ , and ϕ positions of the captured blade, and, for those tests in which the blade breaks through the structure, the cutting angle and location of the perforation. An outstanding feature of the gas gun test technique is that there is absolutely no obscuration of the photographic field of view during the containment event. This is due to the fact that the propelling gases used to accelerate the blade projectile remain completely sealed in the gun. Hence, the blade and structure motions can be observed from the very start of the containment process.

The analysis was applied to model some of the gas gun and rotating tests performed under the present program. Results are presented that were obtained from the analysis of Test 10 (Table V) which involved a finned titanium structure that was impacted by a titanium blade projectile. For the analysis, the structure was modeled with three annular sections, each of which has resistances σ_T , σ_R , and σ_L and friction coefficients μ assigned according to its material, dimensions, and anticipated interaction mechanisms. Data are given in Table V.

The ring sections No. 1, 2, and 3 correspond to the fins, fin channel support region, and backing ring. The material resistance values are representative of interaction mechanisms for the various sections. Blade data correspond to a Task II titanium type projectile and are: weight, 0.0584 kg (0.1287 lb); length, 0.127 m (5.00 in.); width, 0.0508 m (2.00 in.); mass moments

Table V. Containment Structure Input Data for Run 10.

<u>Ring Section Number</u>	<u>Radius m (in.)</u>	<u>σ_T N/m² (psi)</u>	<u>σ_R N/m² (psi)</u>	<u>σ_L N/m² (psi)</u>	<u>μ</u>
1	0.2769 (10.90)	$15,000 \times 10^3$ (2200)	$25,000 \times 10^3$ (3600)	$3,800 \times 10^3$ (550)	0
2	0.3131 (12.33)	138,000 (20,000)	50,000 (7200)	69,000 (10,000)	0
3	0.3198 (12.59)	186,000 (27,000)	186,000 (27,000)	186,000 (27,000)	0
	0.3226 (12.70)				

of inertia (relative to the center of mass): J_n (axis normal to blade face) = $1.0 \times 10^{-4} \text{ J-sec}^2$ ($9.1 \times 10^{-4} \text{ lb-in.-sec}^2$), J_z (about blade stacking axis) = $1.1 \times 10^{-5} \text{ J-sec}^2$ ($9.78 \times 10^{-5} \text{ lb-in.-sec}^2$), and J_c (about chord axis) = $7.85 \times 10^{-5} \text{ J-sec}^2$ ($6.95 \times 10^{-4} \text{ lb-in.-sec}^2$). The initial conditions are: $\bar{V}_0 = 280 \text{ m/sec}$ (920 ft/sec), $\theta = -76.73^\circ$, $\phi = 120^\circ$, $\dot{\theta} = 0$, $\dot{\phi} = 0$, and g (distance between blade center of mass and center of containment structure radius) = 2.36 m (9.30 in.).

Figure 65 shows a 1/2-scale geometric plot of the blade in relation to the containment structure for various time points during the containment process. The initial orientation is such that the trailing edge, base section corner of the blade makes initial contact with the structure at time point 3. The blade is seen to penetrate the finned region of the structure (bounded by R_1 and R_2) and develop a positive change in θ position with increasing time. By time point 23, the entire base section as well as the trailing edge, tip section corner of the blade has entered the structure. At time point 32, almost the entire blade is within the structure. During the subsequent time interval, the blade becomes buried deeper and deeper in the structure and comes to rest in the position corresponding to time point 60. At time point 32, the trailing edge, base section corner begins to enter the region of the structure where the fins are fastened to support ribs ($R_2 \leq r \leq R_3$) and remains there. The trailing edge, tip section enters this same annular space slightly after time point 38 and proceeds to cut through the backing ring ($R_3 \leq r \leq R_4$) just before the blade comes to rest.

Figure 66 shows corresponding plots of \bar{V} , θ , $\dot{\theta}$, ϕ , $\dot{\phi}$, and E versus time, where E is the total kinetic energy of the blade and the other quantities are as described in Figure 7. It is seen that θ (pitching motion) changes in a positive direction throughout the entire process until the blade comes to rest. Generally, ϕ (rolling motion) changes in the negative direction throughout. Both of these rotations correspond to the development by the blade of a flutter and hence, more nested orientation relative to the containment structure. The final energy of the blade at time-point 60 (the time limit preset in the computer run) is 0.272 J (2.41 lb-in.) compared with the initial energy of 2280 J ($2.02 \times 10^4 \text{ lb-in.}$).

Analytical data such as those shown in Figures 65 and 66 can be compared readily with gas gun test data. Examination of the high-speed photographs of Test 10 showed behavior that is basically similar to that indicated in Figure 65. The actual blade cut through the fins in the manner shown in the figure and came to rest in the flat (θ) orientation, positioning itself at the base of the fins. In the test, the blade traveled about one blade length further and had a flatter ϕ orientation in the rest position than is shown in Figure 65. This discrepancy would call for additional computer runs using values of σ and μ that differ from those utilized for this run. The runs would continue until the computer and experimental blade data were found to be in reasonable agreement. The final σ and μ values would then be adopted as representing the actual structure.

Time Pt.	Time (10^{-4} Sec)
3	0.2
9	0.8
17	1.6
23	2.2
28	2.7
32	3.1
38	3.7
44	4.3
60	5.3

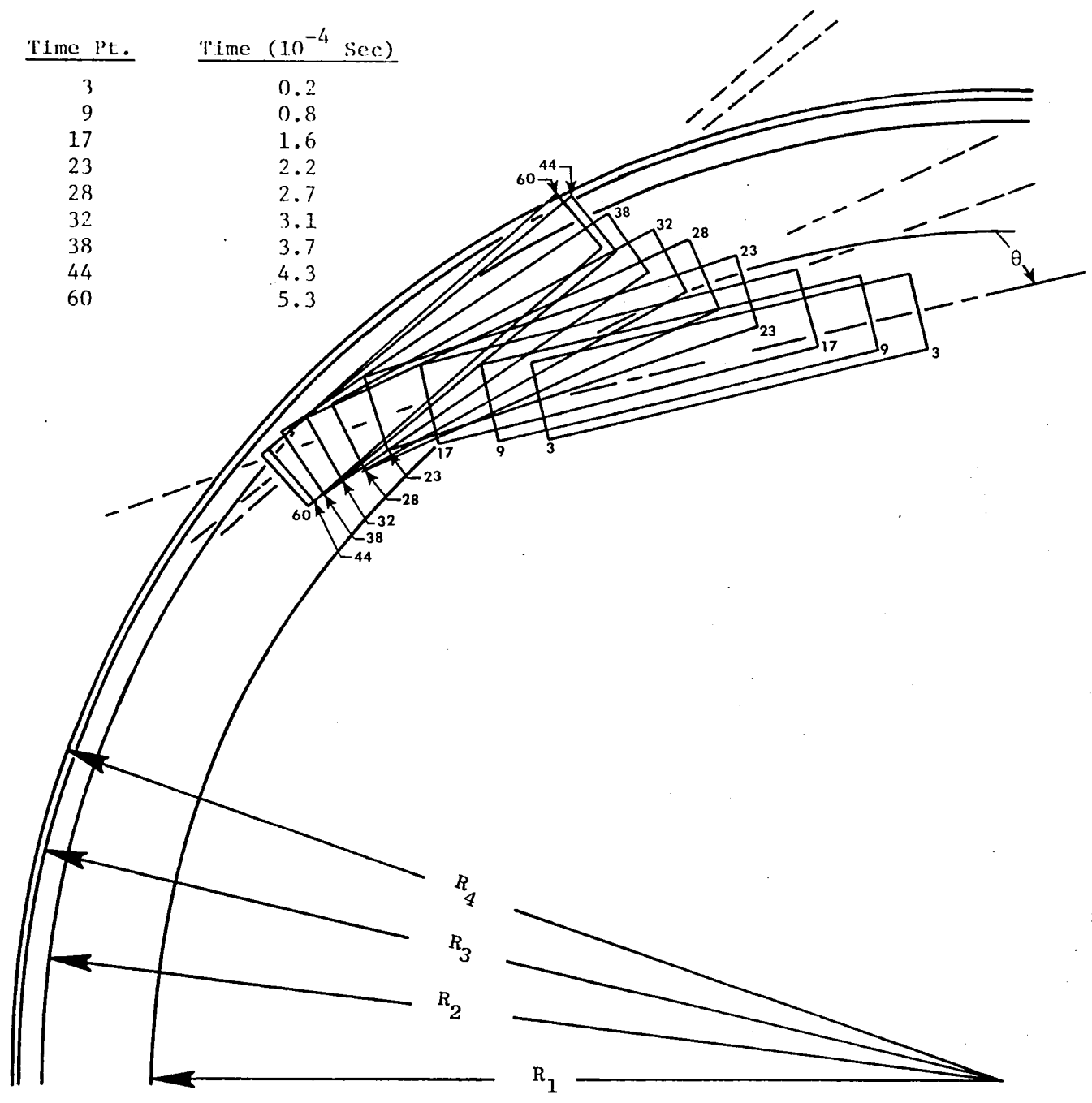


Figure 65. Calculated Interaction of a Task II Titanium Blade Projectile with a Finned-Type Containment Structure.

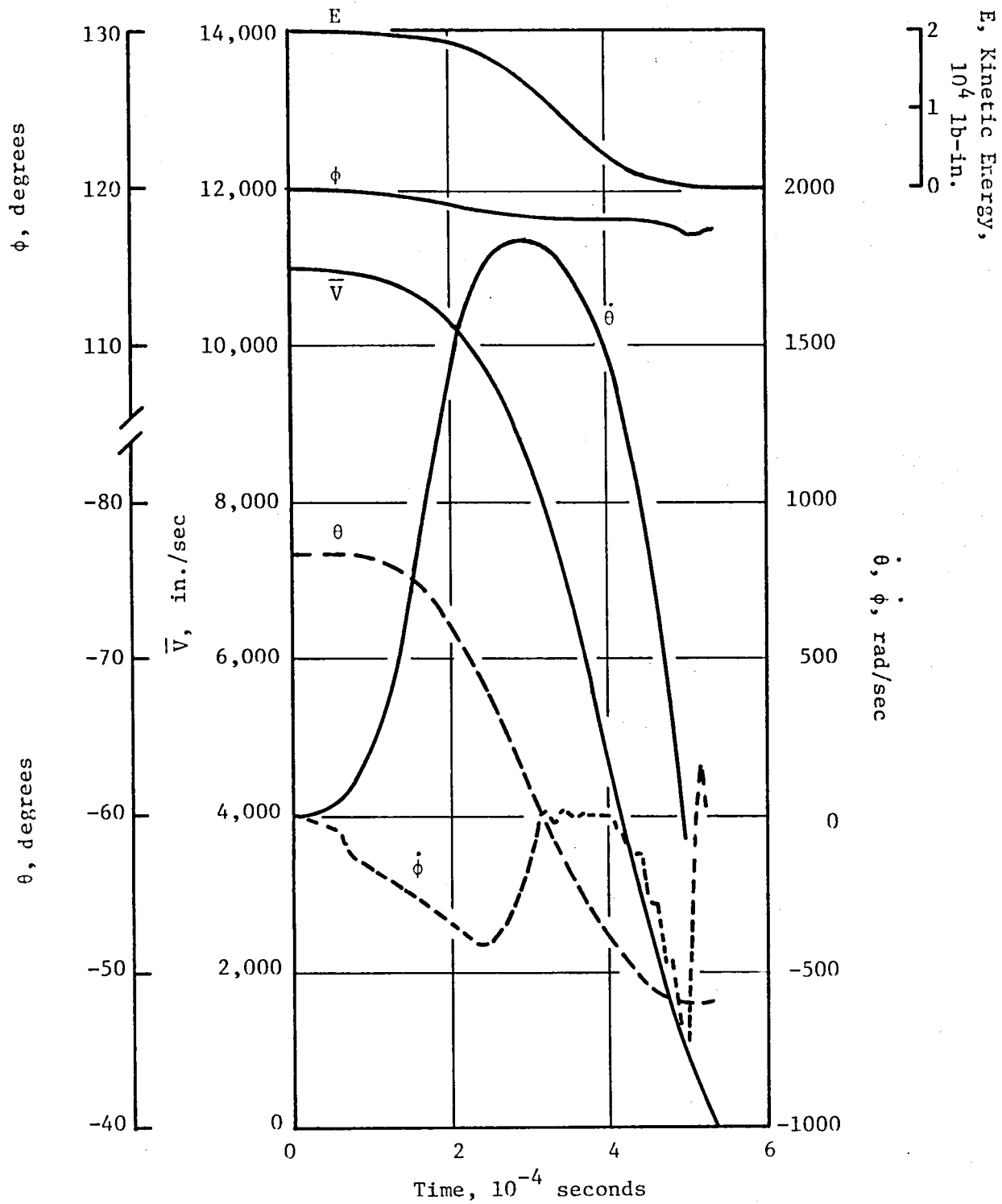


Figure 66. Calculated Blade Motion Parameters Corresponding to Figure 65.

The analysis was then applied to model rotating Test 3 using the results of the correlation analyses of gas gun Test 17. The model utilizes a rectangular-solid equivalent of a TF34 fan blade, having length, mass, and moments of inertia identical to the blades utilized in the test. The containment structure is divided into four annular sections with resistances and friction coefficients as shown in Table VI.

The initial conditions of the released blade, taken from the actual test, are: rotational speed, $\dot{\theta}_0 = 523.6$ rad/sec (5000 rpm); $\phi_0 = 0$; $\bar{V}_0 = 214$ m/sec (702 ft/sec); $\theta_0 = 0$, $\phi_0 = 30^\circ$ (representing 60° tip stagger angle), $g = 0.4087$ m (16.09 in.) (radius to blade c.g.); tip clearance = 6.3×10^{-3} m (0.25 in.).

Typical computed results are shown in Table VII and Figures 67 through 78. Figure 67 is a plot of the blade trajectory relative to the containment structure. The structure is represented by the inner (steel) liner 1, the honeycomb core 2, the Kevlar/epoxy composite outer face sheet of the honeycomb core 3, and the woven Kevlar region 4. The latter is considered to provide containment resistance throughout the entire region indicated in keeping with the overall deformation considered to be appropriate for the woven Kevlar plies. As the results will show, however, only the inner 30% of the assumed woven Kevlar material region was active in the containment process. The outer aluminum shell was not represented in the model due to the fact that a maximum of four material regions was available in the computer program.

The trajectory plot shows the blade at various positions each corresponding to particular time points (NT) after release (see Table VIII). The release position is shown at 12 o'clock (extreme right of figure). The blade is seen to cut through the inner metal liner and honeycomb core as it continues to move after release. In the process its angular velocity $\dot{\theta}$ (Figure 73) and center-of-mass linear velocity V (Figure 72) gradually decrease while the angular velocity $\dot{\phi}$ (Figure 74) about the blade Z axis and the angle ϕ (Figure 70) gradually increase. These effects increase in intensity as the blade cuts into the region occupied by the Kevlar cloth; and as it moves further, it develops a counter rotation speed $\dot{\theta}$, negative θ orientation (Figure 69), and larger ϕ orientation. These orientations and also linear translations bring the blade into an increasingly flat orientation with the containment structure, as it moves toward a nested position within the structure. As a result, the blade steadily loses angular and linear speeds; and finally, the total kinetic energy (Figure 71) is effectively dissipated. The entire process from blade release to complete arrest takes place in 3.04 millisecond.

Plots of the released blade position relative to those of eight unreleased rotor blades are shown for various times following blade release in Figures 75-78. This includes the forward adjacent blade and the seven following adjacent blades. Rotor rotation is shown counterclockwise. The leading and trailing edges of the blades are shown in solid and dashed lines, respectively, except for the released blade which is outlined entirely in solid lines and its exposed area cross hatched. The various circumferential regions of the containment structure are also shown.

Table VI. Containment Structure Analysis Input Data for Rotating Test 3.

<u>Ring Section Number</u>	<u>Material</u>	<u>Radius m (in.)</u>	<u>$N/m^2 \times 10^3$ (psi)</u>	<u>$N/m^2 \times 10^3$ (psi)</u>	<u>$N/m^2 \times 10^3$ (psi)</u>	
1	Stainless Steel Sheet	0.5652 (22.25)	830,000 (120,000)	830,000 (120,000)	830,000 (120,000)	(0.1)
2	Al. Honeycomb	0.5657 (22.27)	275 (40)	550 (80)	275 (40)	(0.1)
3	Kevlar/Epoxy Composite	0.6165 (24.27)	100,000 (15,000)	100,000 (15,000)	100,000 (15,000)	(0.1)
4	Woven Kevlar	0.6171 (24.295)	20,000 (3,000)	20,000 (3,000)	20,000 (3,000)	(0.1)

Table VII. Computed Blade Displacements and Velocities - TF34 Rotating Rig Test 3.

t	x	y	θ	ϕ	\dot{x}	\dot{y}	$\dot{\theta}$	$\dot{\phi}$	E
10^{-3} sec	m (in.)	m (in.)	degrees		m/sec (in. sec)		rad/sec		10^3 J (10^3 lb-in.)
0	0 (0)	0 (0)	0	30.0	214.0 (8425)	0 (0)	523.6	0	14.66 (129.7)
0.7	0.1461 (5.75)	0.00147 (0.058)	17.6	31.3	197.9 (7791)	4.28 (168)	263.9	174.2	12.13 (107.4)
1.2	0.2413 (8.50)	0.00295 (0.116)	22.2	40.0	177.0 (6957)	0.01 (-0.4)	-26.4	350.8	9.59 (84.6)
1.7	0.3178 (12.51)	0.00208 (0.082)	11.9	55.5	119.8 (4717)	-3.68 (-145)	-816.5	671.8	6.02 (53.9)
1.95	0.3447 (13.57)	0.00173 (0.068)	-0.7	58.9	98.2 (3867)	1.63 (64)	-811.7	292.3	4.55 (40.2)
2.20	0.03683 (14.50)	0.00229 (0.090)	-11.6	61.9	86.1 (3391)	1.30 (51)	-674.1	291.4	3.36 (29.1)
2.70	0.3988 (15.70)	0.00239 (0.094)	-26.2	64.6	38.5 (1517)	1.63 (64)	-244.4	88.5	0.60 (5.27)
3.03	0.4028 (15.86)	0.00460 (0.181)	-27.9	67.1	0.7 (28.6)	0.46 (-18.1)	3.4	-1.6	0.25 (2.2)

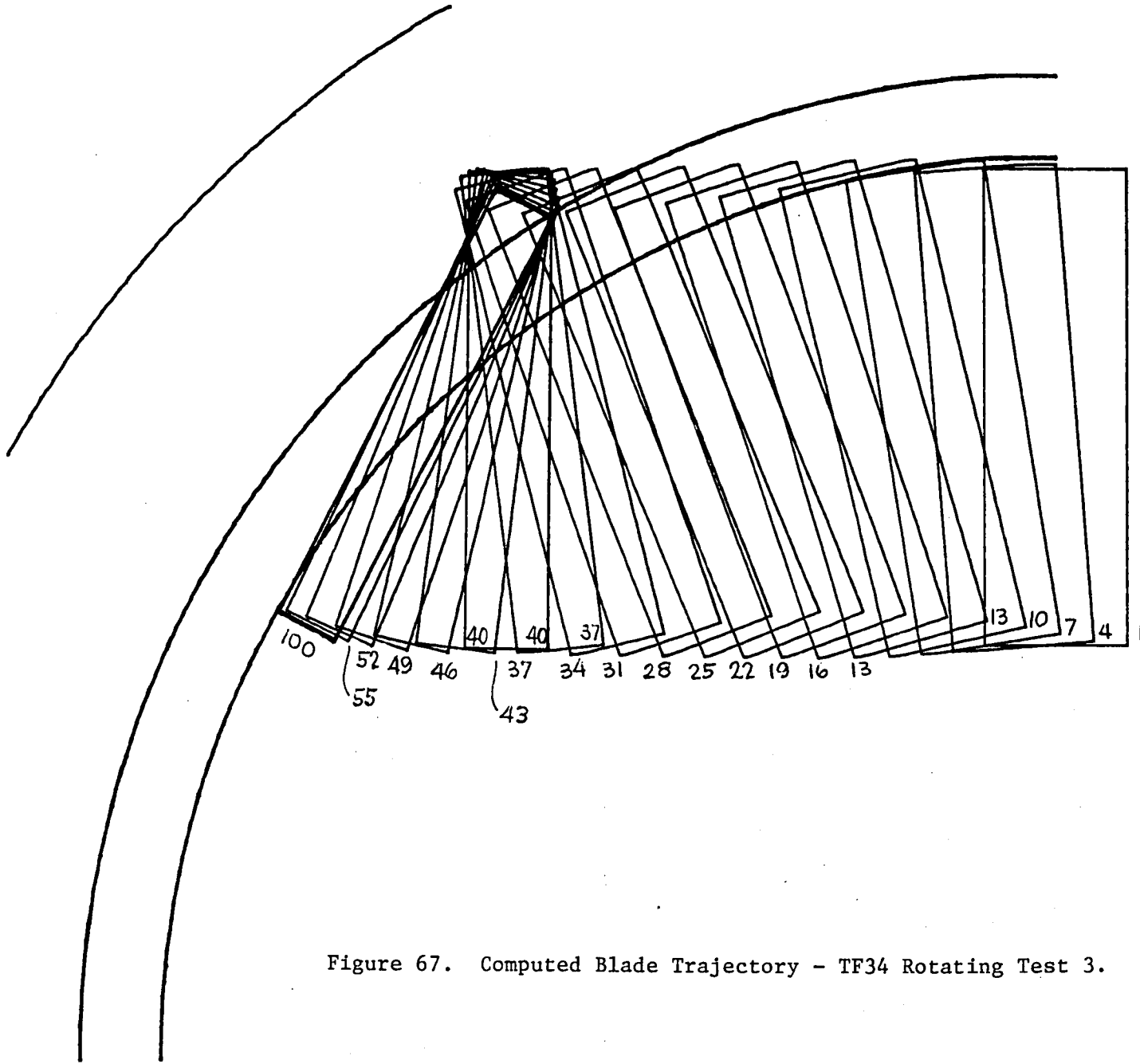


Figure 67. Computed Blade Trajectory - TF34 Rotating Test 3.

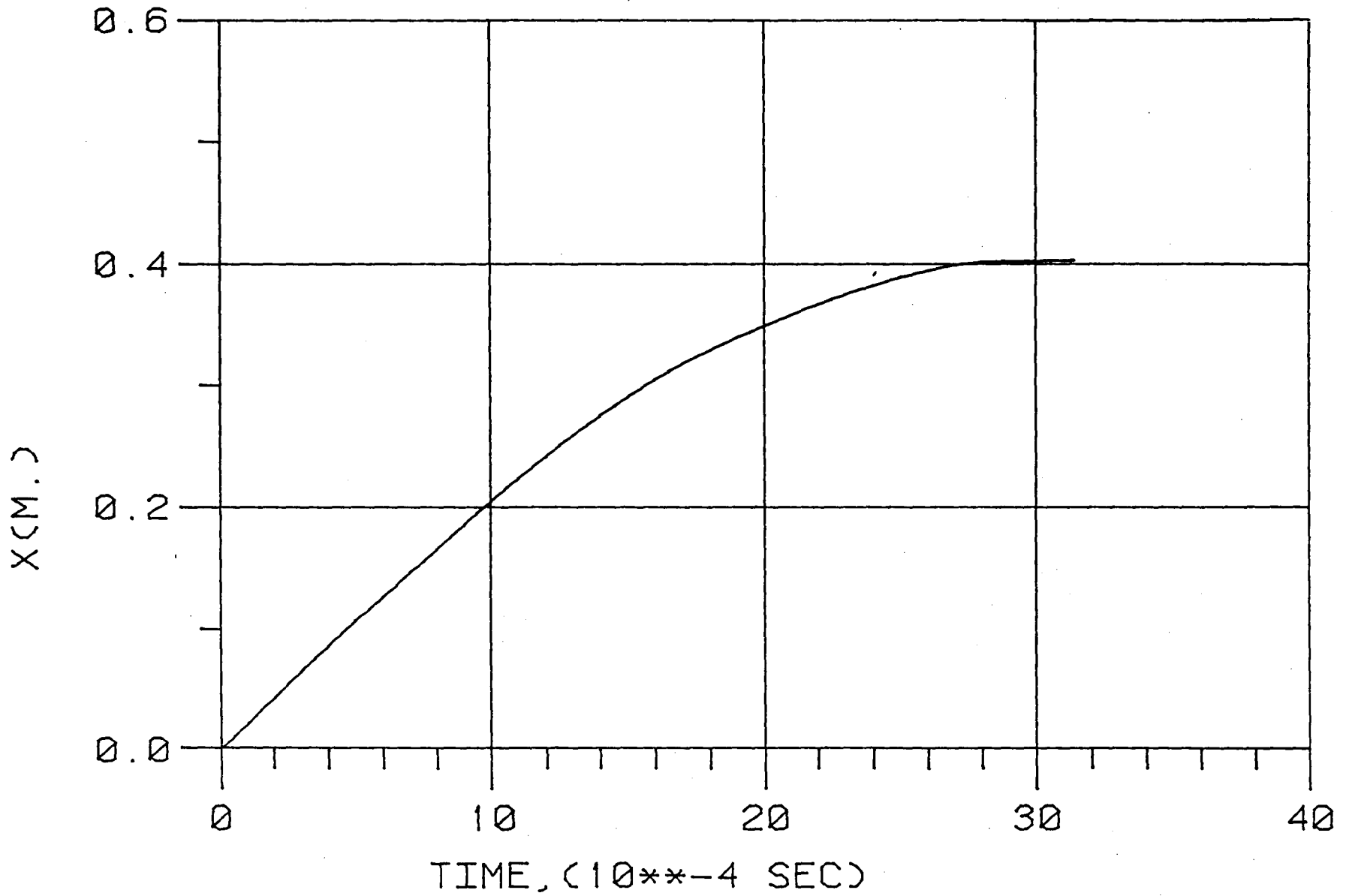


Figure 68. Computed Blade χ Displacement Versus Time - Rotating Test 3.

THETA (RAD)

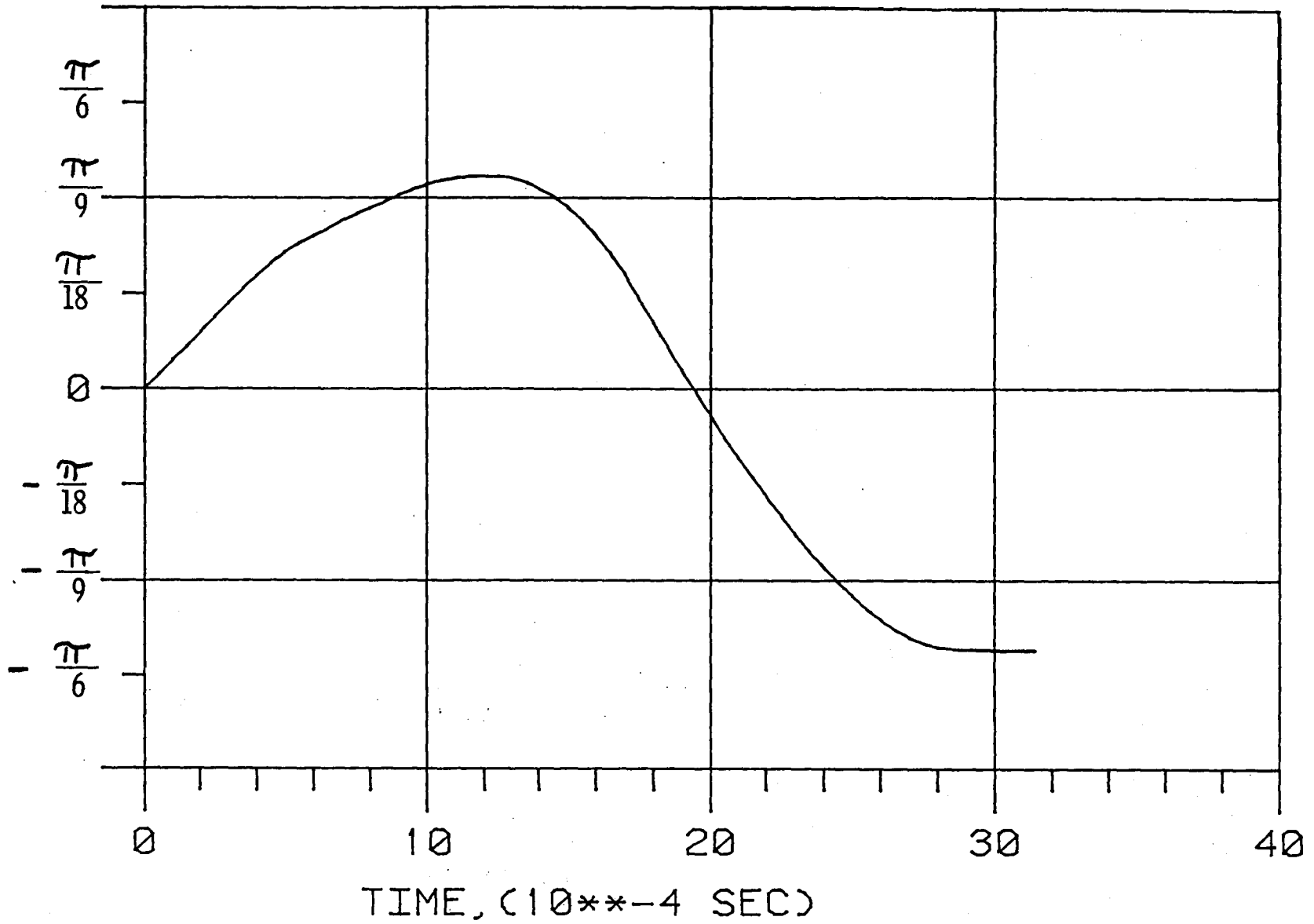


Figure 69. Computed Blade θ Displacement Versus Time - Rotating Test 3.

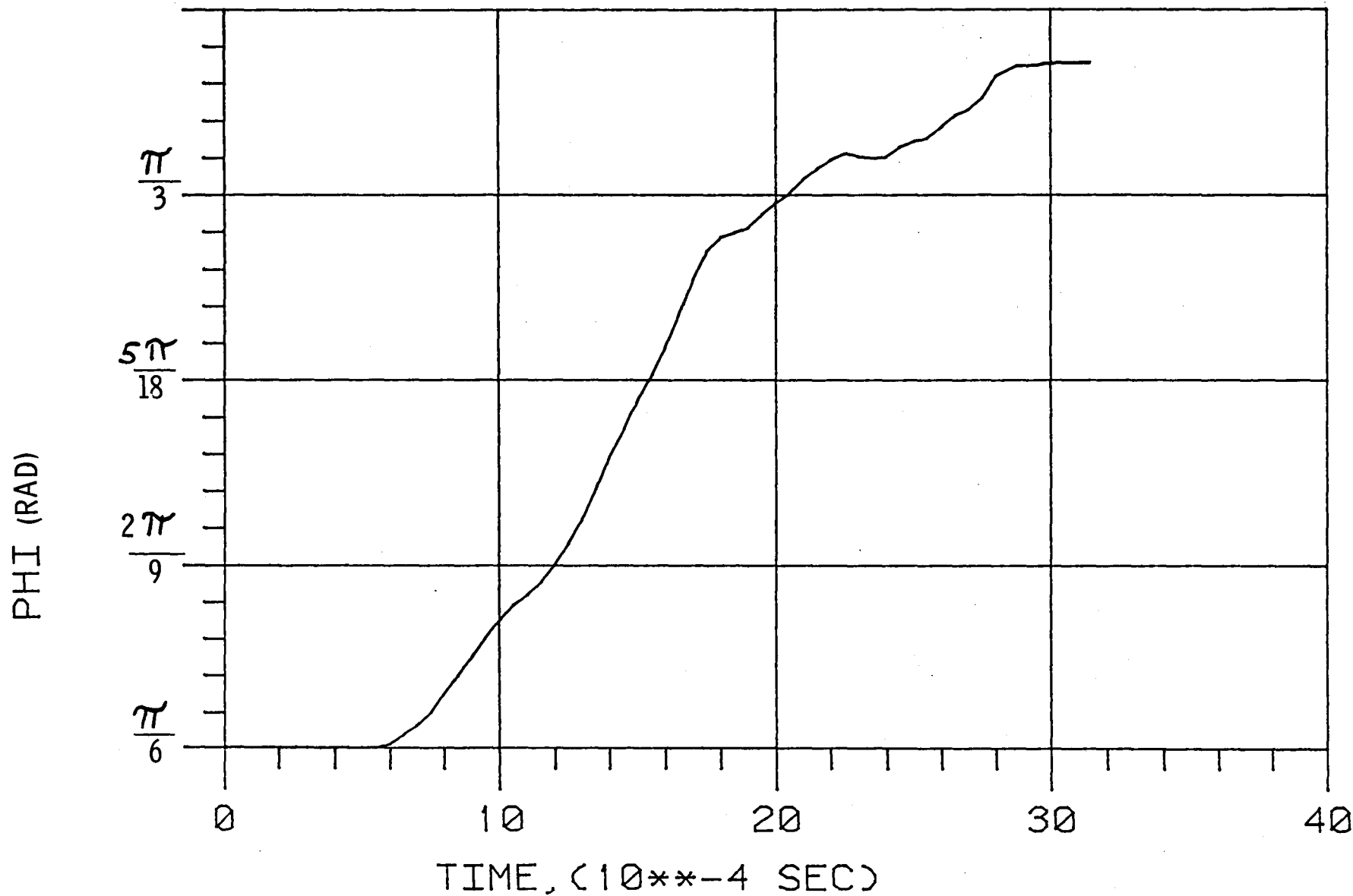


Figure 70. Computed Blade ϕ Displacement Versus Time - Rotating Test 3.

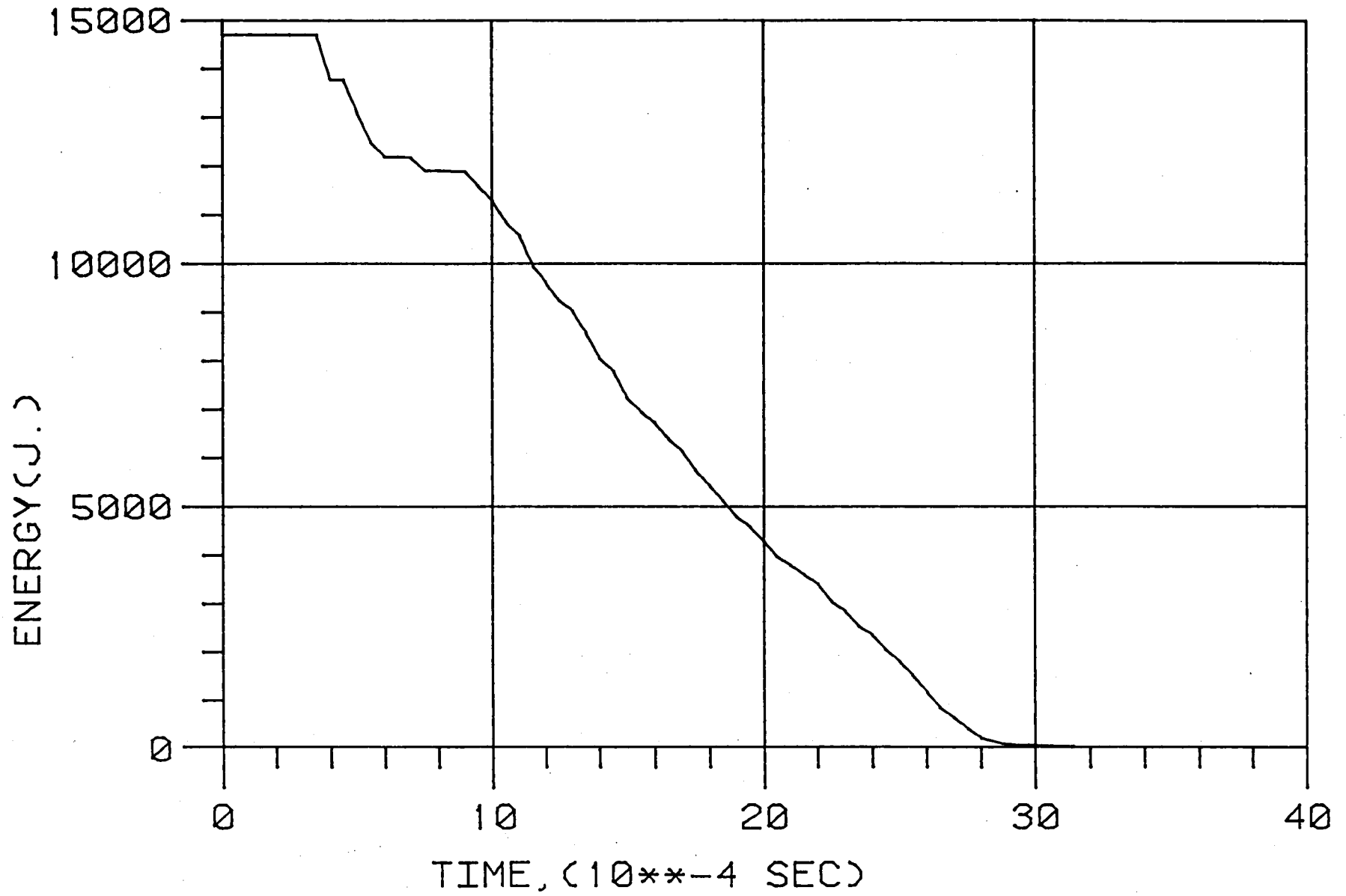


Figure 71. Computed Blade Kinetic Energy Vs. Time - Rotating Test 3.

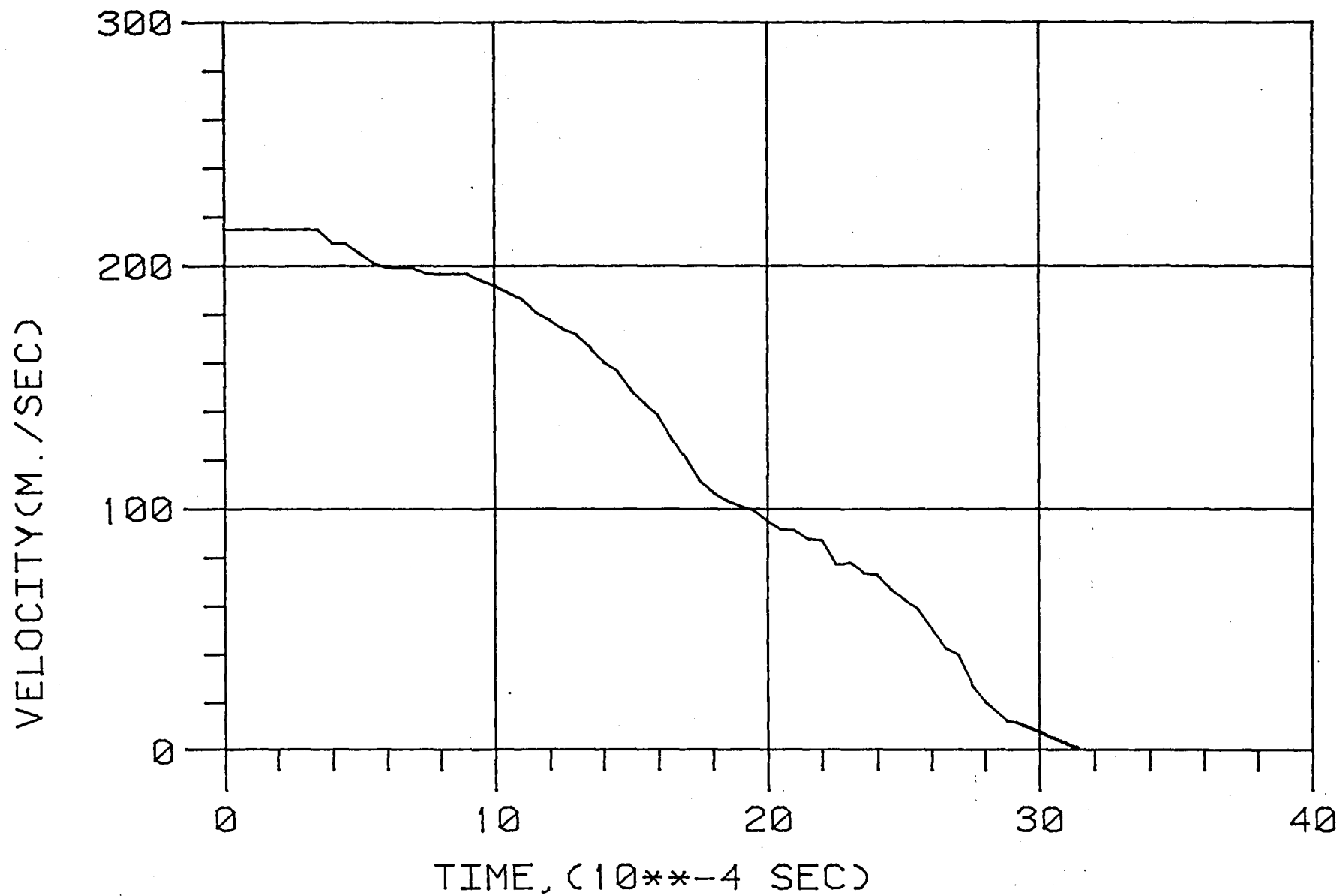


Figure 72. Computed Blade Velocity \bar{v} Vs. Time - Rotating Test 3.

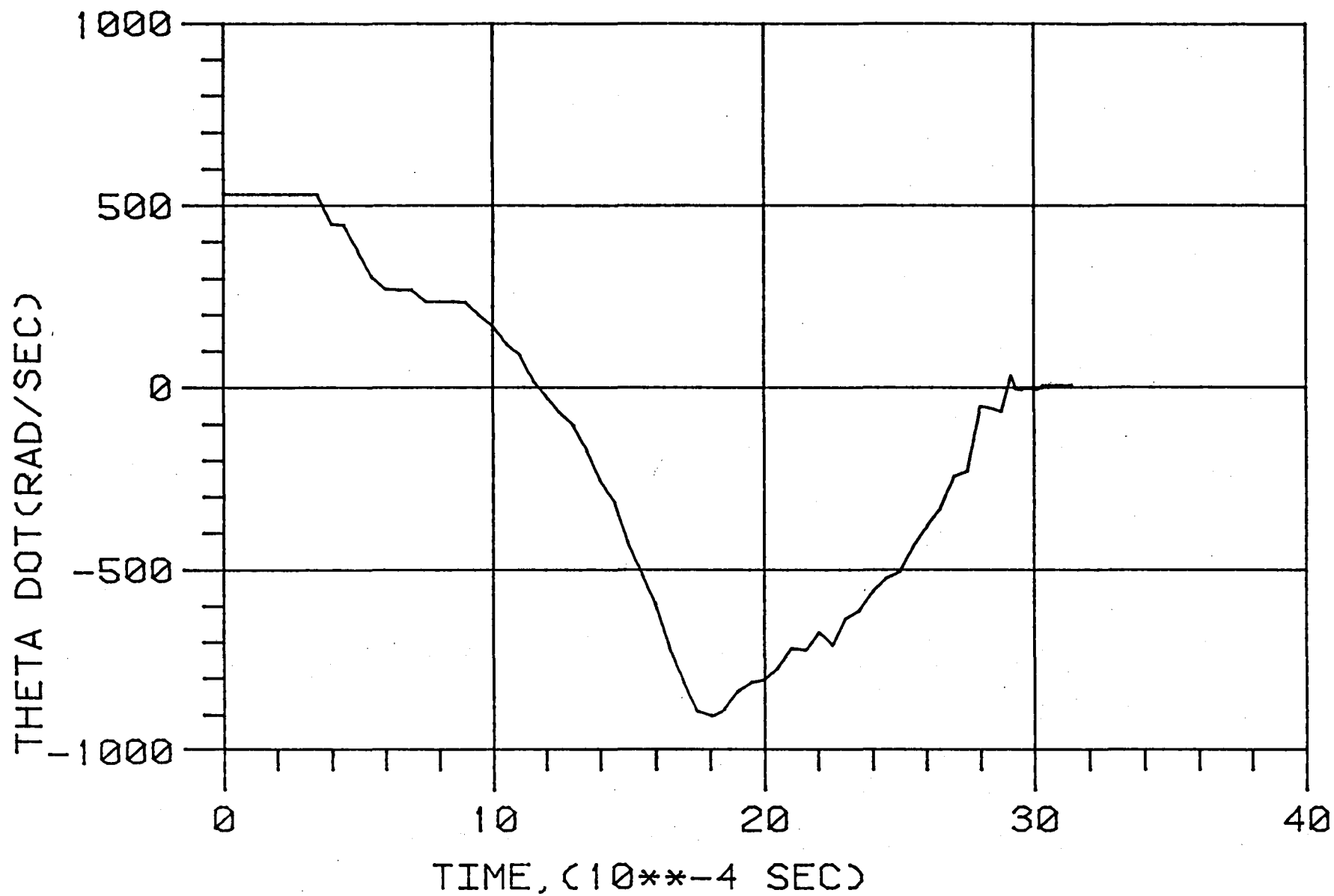


Figure 73. Computed Blade Velocity θ Vs. Time - Rotating Test 3.

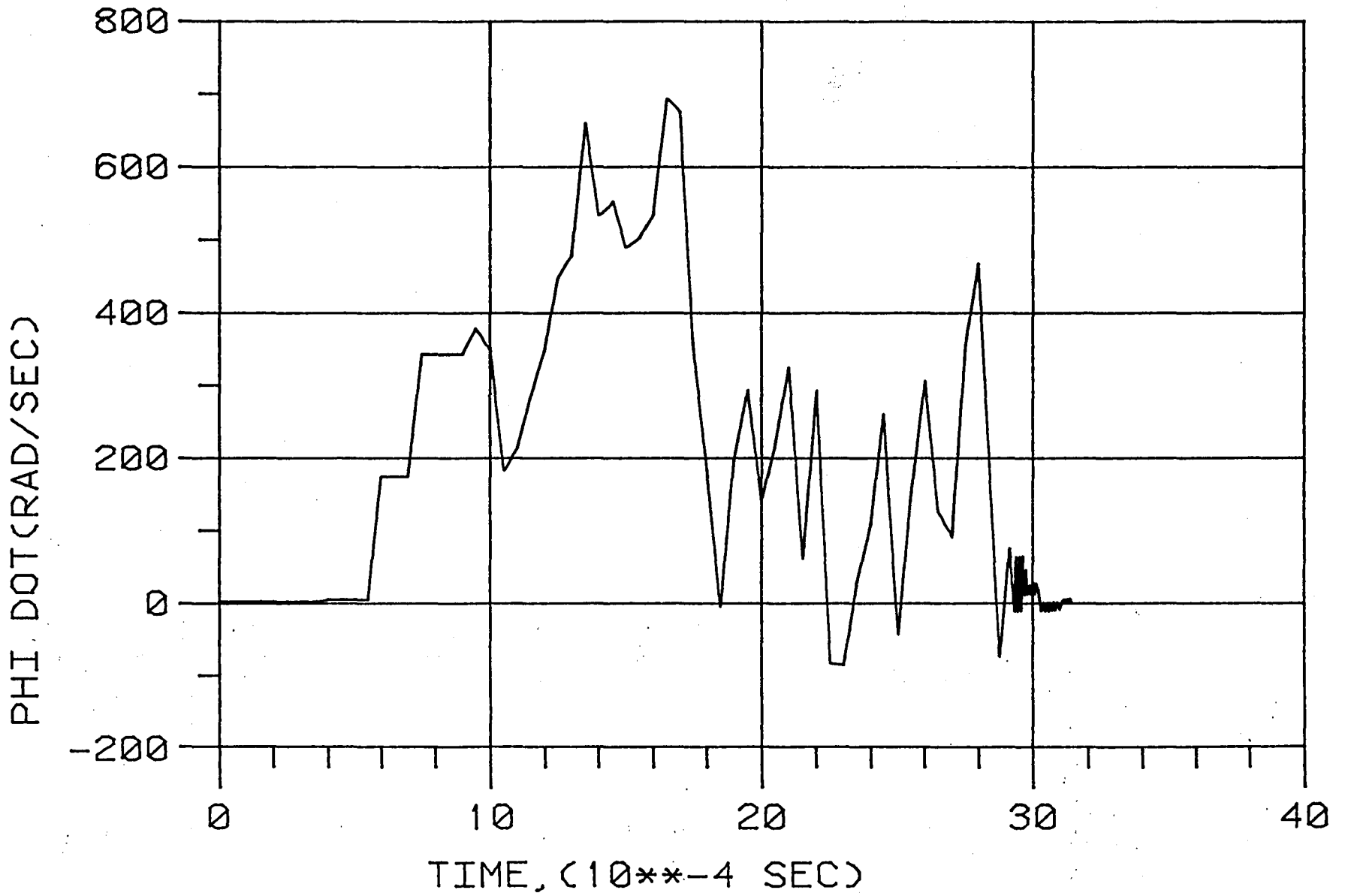


Figure 74. Computed Blade Velocity $\dot{\phi}$ Vs. Time - Rotating Test 3.

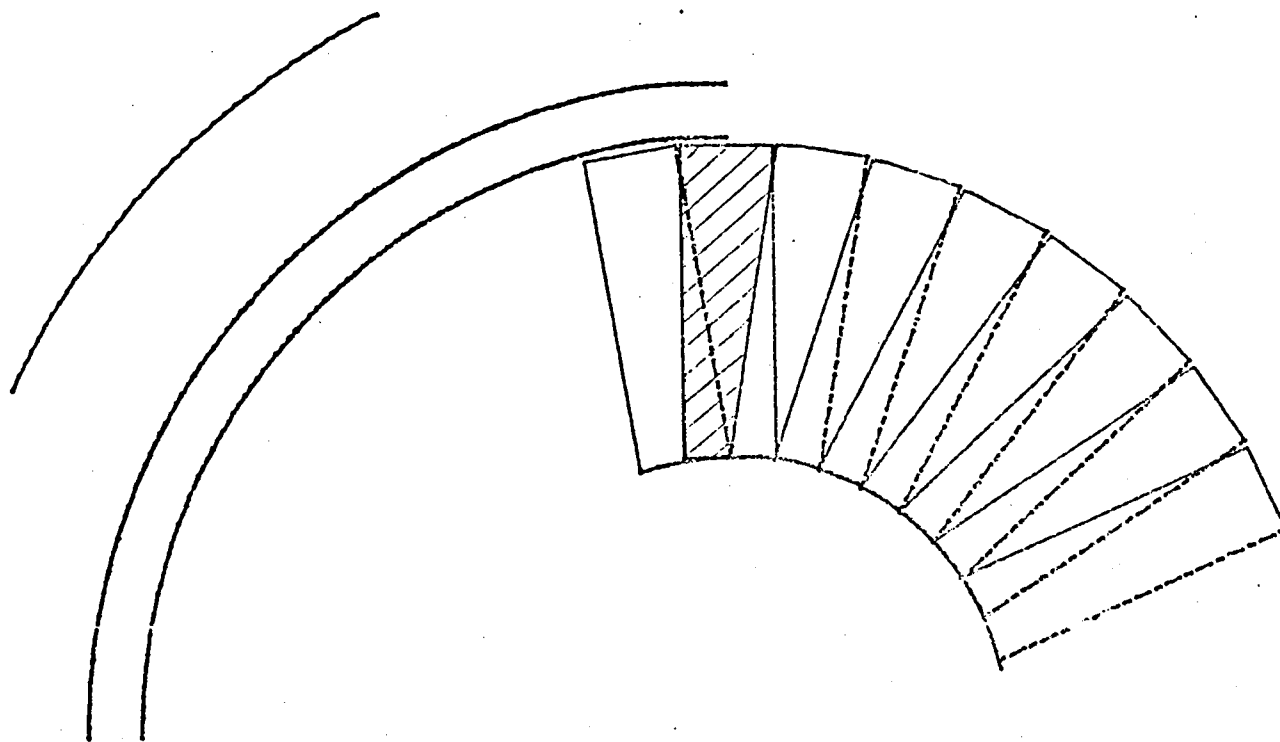


Figure 75. Computed Blade Relative Positions $T = 0$.

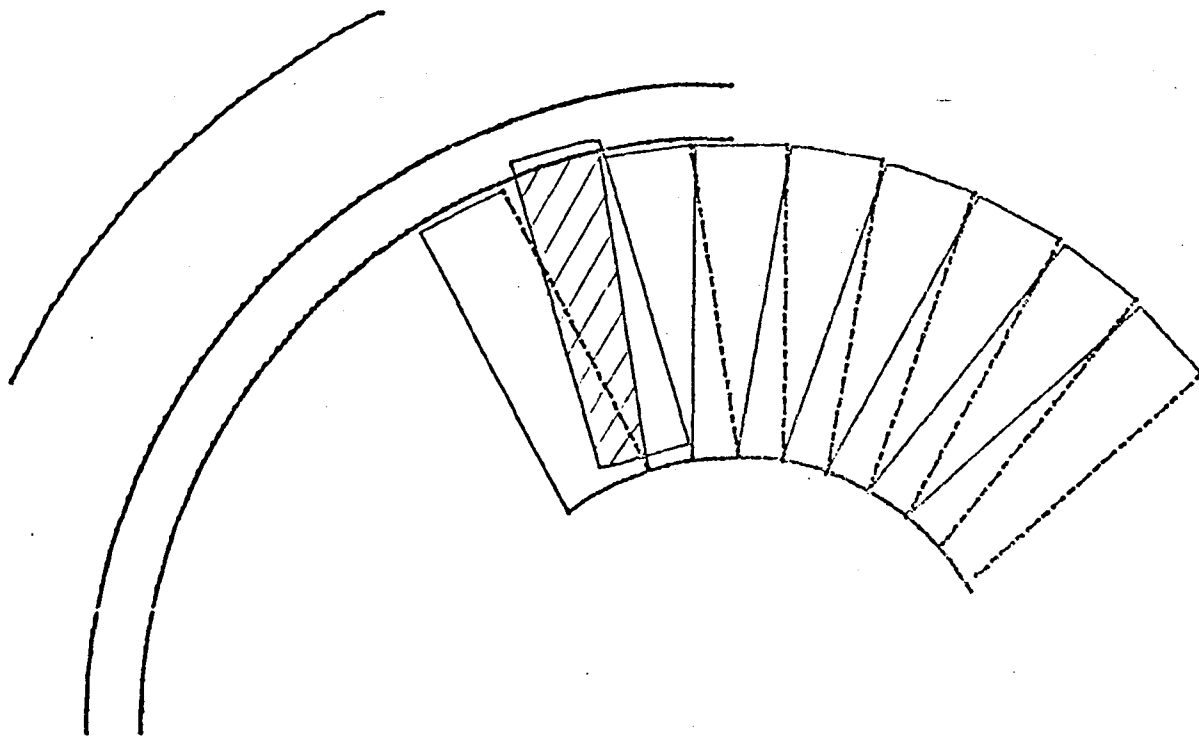


Figure 76. Computed Blade Relative Positions $T = 6 \times 10^{-4}$ Seconds.

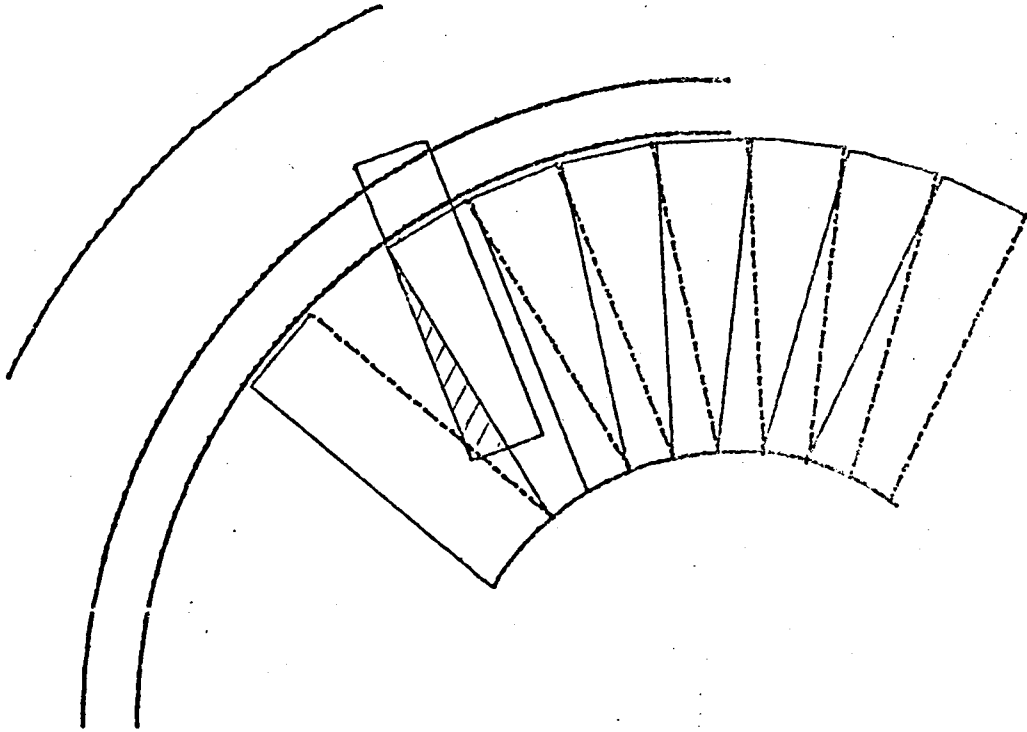


Figure 77. Computed Blade Relative Positions $T = 13.5 \times 10^{-4}$ Seconds.

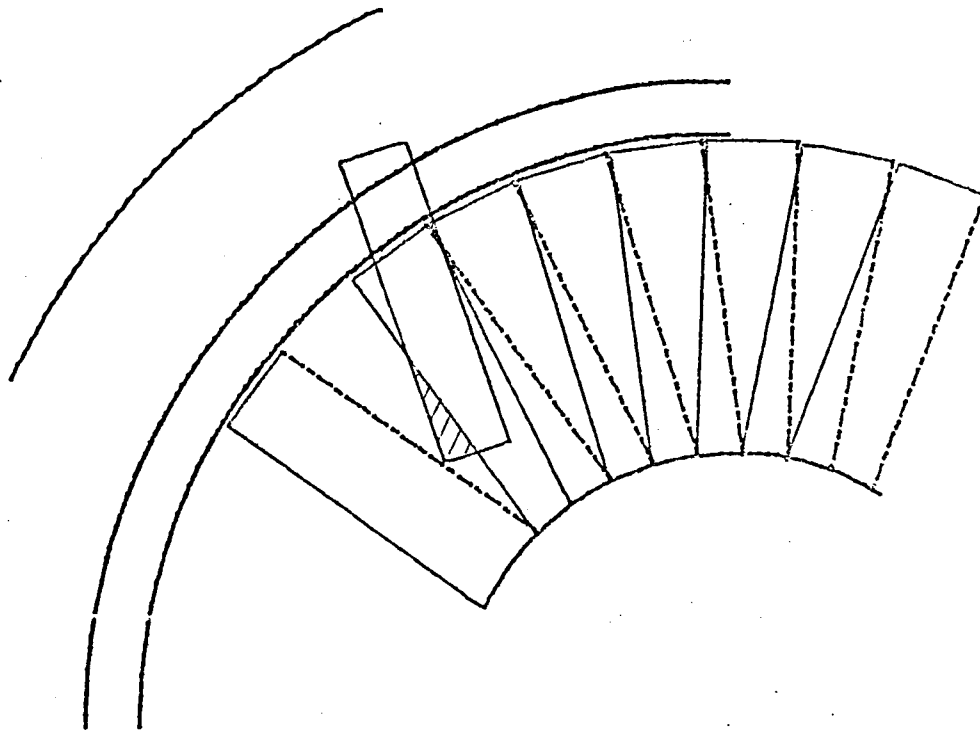


Figure 78. Computed Blade Relative Positions $T = 15 \times 10^{-4}$ Seconds.

Table VIII. Time Values (T) Corresponding to Time Points (NT) for TF34 Rotating Test 3 Trajectory Plot (Figure 67).

<u>NT</u>	<u>$10^{\frac{T}{4}}$ sec</u>	<u>NT</u>	<u>$10^{\frac{T}{4}}$ sec</u>	<u>NT</u>	<u>$10^{\frac{T}{4}}$ sec</u>
1	0	22	1.05	43	2.10
4	0.15	25	1.20	46	2.25
7	0.30	28	1.35	49	2.40
10	0.45	31	1.50	52	2.55
13	0.60	34	1.65	55	2.70
16	0.75	37	1.80	100	3.14
19	0.90	40	1.95		

Figure 75 shows the rotor at the instant of blade release ($t = 0$), the released blade occupying the 12 o'clock position. By $t = 0.6$ millisecond (Figure 76), the blade has been displaced slightly toward the following adjacent blade, especially in the tip region. In the subsequent time intervals, the released blade continues to approach closer to the adjacent following blade until by $t = 1.3$ millisecond (Figure 77) the two blades have already initiated contact with each other, contact occurring initially along the leading edge of the following blade and the convex surface in the leading edge region of the released blade. At initiation of contact, the released blade has rotational speeds $\dot{\theta} \sim -500$ rad/sec and $\dot{\phi} \sim +500$ rad/sec. The contact forces tend to decrease the magnitudes of $\dot{\theta}$ and $\dot{\phi}$ at the blade positions shown in Figure 77. This would tend to decrease the blade interference shown in Figure 78. At later times, the contact forces will act to increase $\dot{\theta}$ negatively and hence, aid development of a flatter orientation relative to the containment structure. As a result, due to the action of the following adjacent blade and subsequent blades, the released blade would be forced into a better final nested position than indicated in Figure 67.

4.5.2 Design Criteria Definition

The design criteria for the design of advanced containment systems may vary somewhat with engine and nacelle design, but in general the following factors should be considered in the design of any containment system:

Criteria Directly Concerned with Containment

1. Sufficient containment material must be provided to prevent escape of any released blade or blade fragment.
2. Containment capability must be provided both forward and aft of the rotor plane. The extent of containment material(s) will depend on the specific blade design involved and the blade/blade interaction characteristics.
3. A nesting area should be provided to allow any released blade, or fragment thereof, to be retained by the casing outside the rotor path. This requirement was vividly demonstrated by rotating Tests 3 and 4.
4. The containment structure should be designed to remain round in the areas away from the main impact area to reduce the blade/casing interaction of the remaining blades. This feature is also required to control the path of the released blade so that a controlled, predictable containment process can be achieved.

Containment System Criteria Which Involves Other Functions (Engine Design Dependent)

1. The containment system must be designed to hold an inlet on the engine despite the vibration and damage involved in a blade release.
2. The containment case must be stiff enough so that the actual frequencies of the case cannot be excited by the fan rotor.
3. The containment case may be required to provide assistance to the fan bearing system by acting as an external bearing for the rotor under the large unbalanced loads and oscillations that occur when a fan blade is released.
4. The system should be easily repairable when damaged by small FOD and blade fragments.

Criteria concerned with inlet retention, the effects of rotor unbalance, and the like were not investigated during this program. The criteria that were evaluated dealt with basic containment capability and with control and retention of the released blade. This testing allows the formulation of preliminary criteria for calculating the amount of dry Kevlar required to contain blade fragments of any given kinetic energy. The gas gun tests run on the Kevlar-filled systems indicated that the amount of Kevlar required could be estimated by $t = 0.00341 \sqrt{E}$ (reference Section 4.3). When the data from the higher-energy tests run in the rotating rig were examined, it appears that this equation was too conservative; for only a relatively small number of the Kevlar plies were damaged. Based on this assessment, it was decided to use the same equation form to calculate the amount of Kevlar required but to use a constant that would put the curve through the lowest data point of all the tests, both gas gun and rotating rig run on the dry Kevlar belt type of containment system. This resulted in $t = 0.002635 \sqrt{E}$. This curve and the pertinent data points are shown in Figure 79.

The tests performed under this program also demonstrate the need for controlling the released blade motion and nesting it away from the rotor path. Although it was apparent from these tests that there was significant deformation of the blade, allowing it to nest in a smaller depth of honeycomb than would be the case for an undeformed blade, there was not sufficient data generated to allow determination of a minimum required depth of honeycomb.

4.5.3 Full-Scale Containment System Evaluation

One of the objectives of this program was to extrapolate the data and project the design and weight savings for a full-scale, large turbofan engine. Another objective was to show that containing a composite or superhybrid blade is much less difficult than containing a titanium blade, and hence is the preferred course. But with the difficulty encountered in releasing the superhybrid blades (the composite portion separating well before the titanium spar),

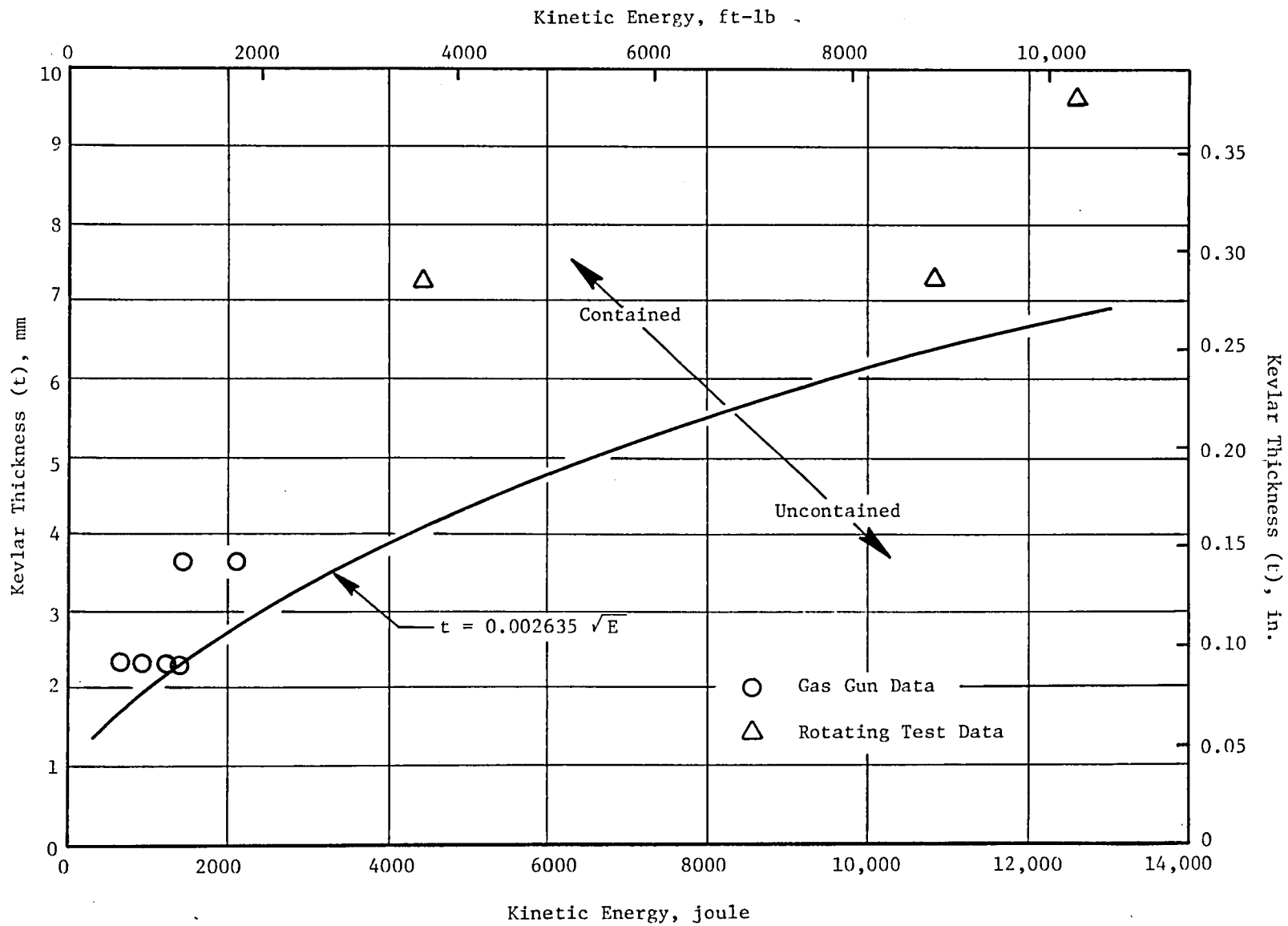


Figure 79. Thickness of Kevlar Versus Kinetic Energy - All Test Data.

the latter objective could not be attained. Nevertheless, it is clear that the main item to be contained would be not the composite shell, which did little damage, but the titanium spar. Since the design of these blade types is still evolving due to the bird impact requirement, the weight of this spar is difficult to estimate. But any containment system designed for use with composite- or superhybrid-type blades could be based on the spar weight and the equation for required Kevlar thickness presented in Section 4.5.2.

Sufficient data were generated, however, to permit a preliminary design of an advanced containment system for a titanium-bladed rotor. The CF6-50 containment ring was chosen as the current state-of-the-art baseline. This is a ribbed steel ring, as shown in Figure 80, and weighs 220.0 kg (486 lb). Using the information obtained during the rotating rig tests of this program, the advanced design shown in Figure 81 was developed. This design provides a nesting and tracking control area shown to be necessary by these tests. It also provides a steel surface next to the blades to resist minor damage and to provide external bearing support for a fan unbalanced by loss of a blade. The amount of Kevlar required was calculated by $t = 0.002645 \sqrt{E}$. The c.g. kinetic energy of a CF6-50 blade is 211,536 J (156,000 ft-lb). Therefore, the Kevlar required was 0.0264 m (1.04 in.). The total advanced containment system, which also provides inlet support and adequate casing stiffness, weighs approximately 181.4 kg (400 lb), of which the dry Kevlar constitutes 63.5 kg (140 lb) or 35%. The total advanced system is, therefore, 38.5 kg (85 lb) lighter than the current containment system, a weight savings of 18%. If these concepts were to be applied to an engine installation during the initial design rather than as a retrofit, the advanced containment design could be even lighter for a total weight savings of from 30% to 40% while still fulfilling the required functions. It should be realized, however, that these designs are extrapolated at least an order of magnitude in energy level from the actual tests run during this program.

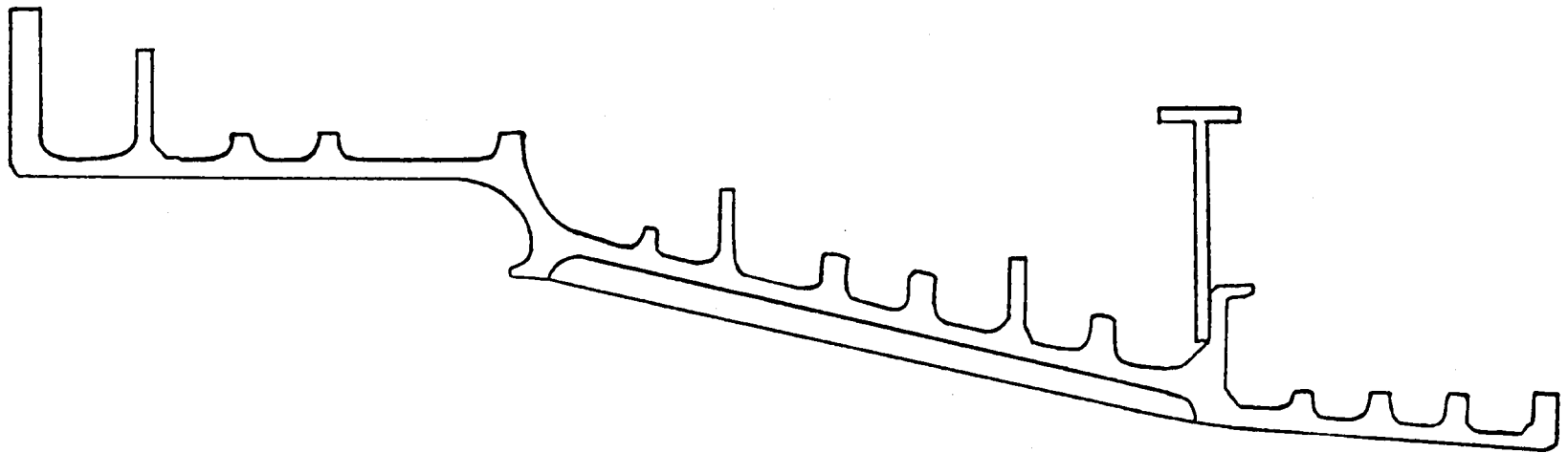


Figure 80. State-of-the-Art Steel Containment Ring.

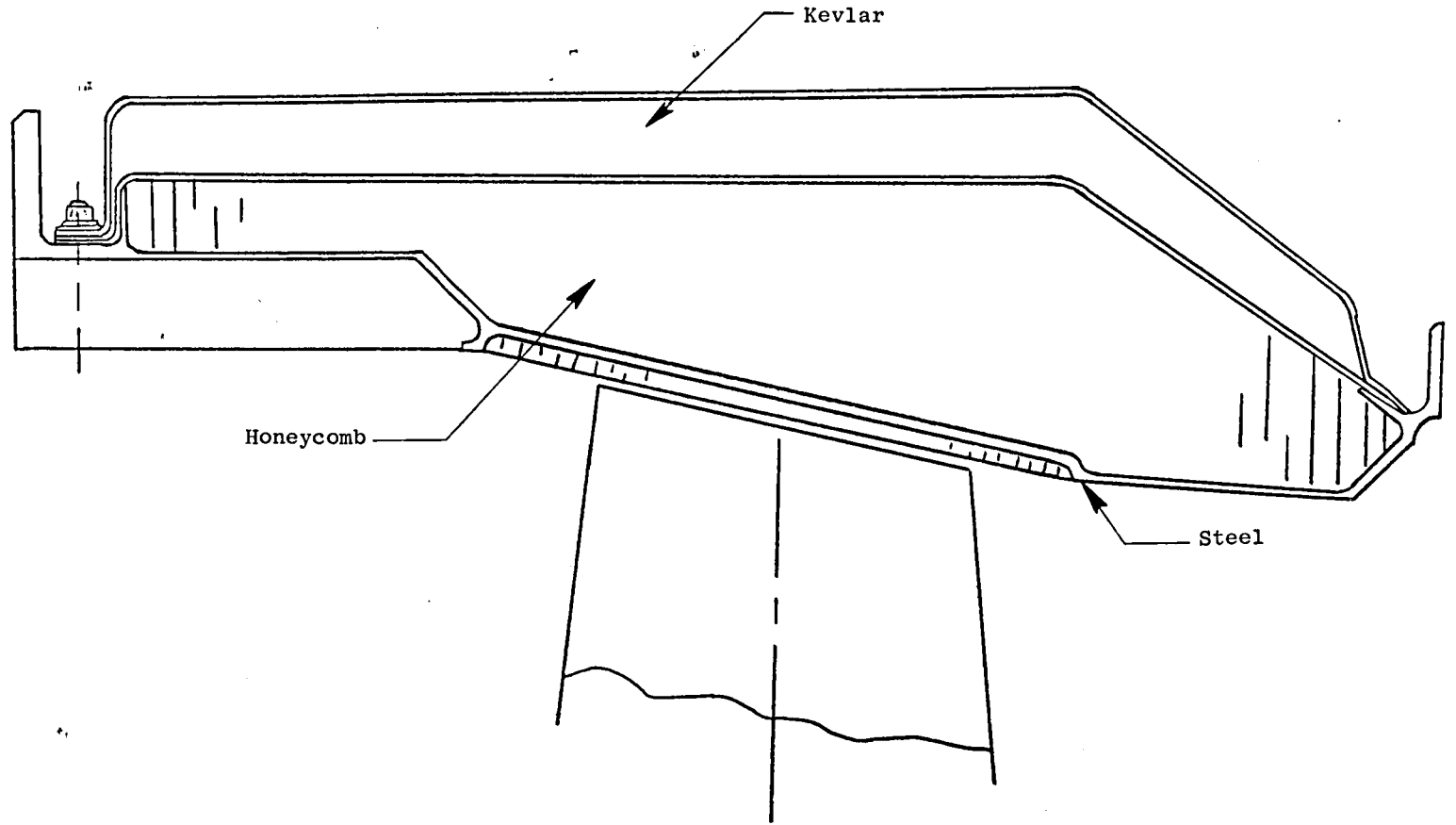


Figure 81. Lightweight Containment System..

5.0 CONCLUSIONS AND RECOMMENDATIONS

A summary of the conclusions drawn from the analytical work and testing is presented below, along with some recommendations for future work.

5.1 CONCLUSIONS

1. The concept consisting of a thin steel face backed up by dry Kevlar cloth, similar to some of the lightweight armor concepts developed by the U.S. Army, proved to be the most weight-effective concept considered for the containment of fan blades and fan blade fragments. The weight savings available through the use of this concept has been estimated at 18% for a replacement application and 30 to 40% if provided as original equipment.
2. The use of a nesting area to keep the released fragment out of the fan rotor path showed significant advantages. The practice minimizes the secondary damage that occurs in current systems which let the fragment bounce around in the rotor path and damage other blades. In addition, this nesting area, if properly designed, can provide the required casing stiffness at a very low weight. It provides tracking control of the blade or fragment keeping the fragment within the containment system and making the process much more repeatable.
3. The analytical effort performed under this program gave promise of developing a method that will allow prediction of blade motion based on a set of initial conditions and a mathematical description of the containment system. Initial blade/blade interactions can also be determined.
4. The final concepts tested in the gas gun phase of the program showed good containment features, including nesting and tracking. However, the finned systems tested were heavier than the steel/Kevlar system.

5.2 RECOMMENDATIONS

1. In order for the concepts developed by this program to be applied to production hardware as early as possible, it is necessary to generate enough parametric data on the selected system to permit an optimum design to be made with respect to the following: the amount of Kevlar actually needed, the ratio of Kevlar to steel, and the amount of damage caused not only by a full airfoil but by smaller objects as well. The repairability of these systems when struck by small objects must also be evaluated.

2. The analytical method should be expanded to better account for interaction of the failed blade with a following blade. The ability to correlate the analysis with actual test results must also be demonstrated in considerable detail.
3. Although the basic containment concept has been defined, the specific material, composition, and form must be further refined. This will require both analysis and tests of potential candidate materials (such as Kevlar 29 versus Kevlar 49), weaves (bidirectional versus unidirectional), felts, and configurations.
4. The ability to scale up the containment system from the 13,560 J (10,000 ft-lb) of energy thus far demonstrated to the energy level of a CF6-size blade must be demonstrated. As can be seen from Figure 82, this requires considerable extrapolation of the existing data, and the ability to contain these very large energies must be demonstrated.
5. Once the ability to contain the energy of a released CF6 blade has been demonstrated, the full containment ring function must be demonstrated. This will require releasing a single CF6 blade from a full rotor in a rig which very closely represents the engine low-pressure system structure. This type of test not only demonstrates the ability of the containment system to contain the released blade, but also evaluates the effects of blade/blade and blade/casing interaction and the effects of the total unbalance loads on the rest of the structure. This must then be followed by endurance testing on a demonstrator engine.

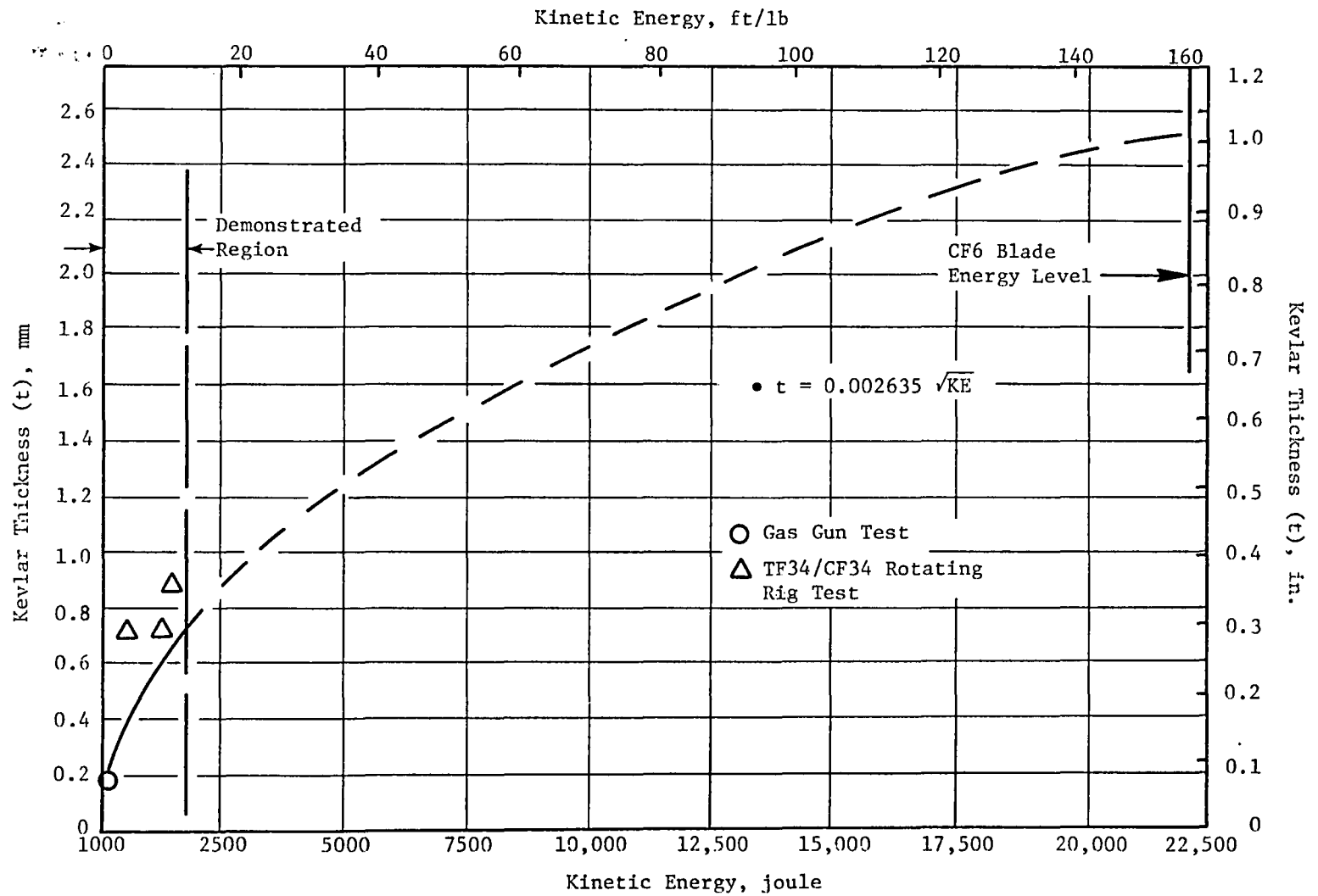


Figure 82. Amount of Kevlar Required Versus Kinetic Energy.

6.0 REFERENCES

1. Coppa, A.P., and Semon, H.W., "New Developments in Rotor Blade Containment Technology", General Electric Company, TIS Report No. 695DB, July 1969.

DISTRIBUTION LIST FOR FINAL REPORT

NASA CR 159544

CONTRACT NAS 3-20118

	<u>Mail Stop</u>	<u>Copies</u>
NASA-Lewis Research Center 21000 Brookpark Road Cleveland, OH 44135		
Attn: Contracting Officer	500-312	1
Technical Report Control Officer	5-5	1
Technology Utilization Office	3-16	1
AFSC Liaison Office	501-3	1
M&S Division Contract File	49-1	1
Library	60-3	1
R. H. Johns	49-3	1
G. T. Smith	49-3	10
C. C. Chamis	49-3	1
J. C. Freche	49-1	1
J. P. Barranger	77-1	1
A. G. Holmes	100-1	1
C. L. Walker	77-5	1
S. Weiss	500-204	1
National Aeronautics & Space Administration Washington, DC 20546		
Attn: NHS-22/Library		2
RWS-3/D. A. Gilstad		1
RWS-3/D. N. Mayer		1
NASA-Ames Research Center Moffett Field, CA 94035		
Attn: Library	202-3	1
NASA-Goddard Space Flight Center Greenbelt, MD 20771		
Attn: 252/Library		1
NASA-John F. Kennedy Space Center Kennedy Space Center, FL 32931		
Attn: Library	AD-CS0-1	1
NASA-Langely Research Center Hampton, VA 23365		
Attn: Library	185	2
H. F. Hardrath	188M	1
NASA-Lyndon B. Johnson Space Center Houston, TX 77001		
Attn: JM6/Library		1
NASA-George C. Marshall Space Flight Center Marshall Space Flight Center, AL 35812		
Attn: AS61/Library		1

Copies

Jet Propulsion Laboratory 4800 Oak Grove Drive Pasadena, CA 91103 Attn: Library	1
NASA S&T Info Facility P. O. Box 8757 Baltimore-Washington Int. Airport MD 21240 Attn: Acquisition Dept.	30
Air Force Systems Command Aeronautical Systems Division Wright-Patterson AFB, OH 45433 Attn: Library C. W. Cowie	1 1
Aerospace Corp. 2400 E. El Segundo Blvd. Los Angeles, CA 90045 Attn: Library-Documents	1
Air Force Office of Scientific Research Washington, DC 20333 Attn: Library	1
Department of the Army U. S. Army Material Command Washington, DC 20315 Attn: AMCRD-RC	
U. S. Army Ballistics Research Lab. Aberdeen Proving Ground, MD 21005 Attn: Dr. Donald F. Haskell DRXBR-BM	1
Mechanics Research Lab. Army Materials and Mechanics Research Center Watertown, MA 02172 Attn: Dr. Donald W. Oplinger	1
U. S. Army Missile Command Redstone Scientific Information Center Redstone Arsenal, AL 35808 Attn: Document Section	1

Copies

Commanding Officer
 U. S. Army Research Office (Durham)
 Box CM, Duke Station
 Durham, NC 27706
 Attn: Library

1

Bureau of Naval Weapons
 Department of the Navy
 Washington, DC 20360
 Attn: RRRE-6

1

Commander
 U. S. Naval Ordnance Laboratory
 White Oak
 Silver Springs, MD 20910
 Attn: Library

1

Director, Code 6180
 U. S. Naval Research Laboratory
 Washington, DC 20390
 Attn: Library

1

Denver Federal Center
 U. S. Bureau of Reclamation
 P. O. Box 25007
 Denver, CO 80225
 Attn: P. M. Lorenz

1

National Technical Information Service
 Springfield, VA 22151

4

Naval Air Propulsion Test Center
 Aeronautical Engine Department
 Trenton, NJ 08628
 Attn: Mr. James Salvino

1

Naval Air Propulsion Test Center
 Aeronautical Engine Dept.
 Trenton, NJ 08628
 Attn: Mr. Robert DeLucia

1

Naval Air Propulsion Test Center
 Aeronautical Engine Department
 Trenton, NJ 08628
 Attn: Mr. G. J. Mangano

1

Federal Aviation Administration
 Code ANE-214, Propulsion Section
 12 New England Executive Park
 Burlington, MA 01803
 Attn: Mr. Robert Berman

1

Copies

Federal Aviation Administration DOT
 Office of Aviation Safety, FOB 10A
 800 Independence Ave., S.W.
 Washington, DC 20591
 Attn: Mr. John H. Enders 1

Federal Aviation Administration
 AFS-140
 Washington, DC 20591
 Attn: Mr. A. K. Forney 1

FAA, AFS-140
 800 Independence Ave., S.W.
 Washington, DC 20591
 Attn: Dr. Thomas G. Horeff 1

FAA, ARD-520
 2100 2nd Street, S.W.
 Washington, DC 20591
 Attn: Cdr. John J. Shea 1

National Transportation Safety Board
 800 Independence Ave., S.W.
 Washington, DC 20594
 Attn: Mr. Edward P. Wizniak, TE-20 1

Solar Energy Division
 Energy Research and Development Admin.
 200 Mass. Ave., N.W.
 Washington, DC 20545
 Attn: Dr. John W. Leech 1

MIT, Room 33-313
 Cambridge, MA 02139
 Attn: Professor John Dugundji 1

Rockwell International Corp.
 Los Angeles International Airport
 Los Angeles, CA 90009
 Attn: Mr. Joseph Gausselin
 D 422/402 AB71 1

MIT, Room 41-211
 Cambridge, MA 02139
 Attn: Dr. Kyohei Kondo 1

MIT, Room 41-219
 Cambridge, MA 02139
 Attn: Mr. Allen Lush 1

MIT, Room 33-122
 Cambridge, MA 02139
 Attn: Mr. Fred Merlis 1

Copies

MIT, Room 33-207 Cambridge, MA 02139 Attn: Professor Rene H. Miller	1
MIT, Room 41-219 Cambridge, MA 02139 Attn: Mr. Thomas R. Stagliano	1
MIT, Room 41-219 Cambridge, MA 02139 Attn: Professor Emmett A. Witmer	1
MIT, Room 41-219 Cambridge, MA 02139 Attn: Mr. Jose J. A. Rodal	1
MIT, Room 6-202 Cambridge, MA 02139 Attn: Dr. David Roylance	1
University of Illinois at Chicago Circle Dept. of Materials Engineering Box 4348 Chicago, IL 60680 Attn: Dr. Robert L. Spilker	1
Detroit Diesel Allison General Motors Corp. Speed Code T3, Box 894 Indianapolis, IN 46206 Attn: Mr. William Springer	1
Detroit Diesel Allison General Motors Corp. Indianapolis, IN 46206 Attn: Mr. Joseph Berg	1
AVCO, Lycoming Division 550 South Main Street Stratford, CT 06497 Attn: Mr. Herbert Kaehler	1
AVCO, Lycoming Division 550 South Main Street Stratford, CT 06497 Attn: Mr. John Veneri	1
Beech Aircraft Corp., Plant 1 Wichita, KA 67201 Attn: Mr. M. K. O'Connor	1

Copies

Boeing Aerospace Co. Impact Mechanics Lab. P. O. Box 3999 Seattle, WA 98124 Attn: Dr. R. J. Bristow	1
Boeing Commercial Airplane Co. P. O. Box 3707 Seattle, WA 98124 Attn: Dr. Ralph B. McCormick	1
Boeing Commercial Airplane Co. P. O. Box 3707 M/S 73-01 Seattle, WA 98124 Attn: Mr. David T. Powell	1
Boeing Commercial Airplane Co. P. O. Box 3707 Seattle, WA 98124 Attn: Dr. John H. Gerstle	1
Boeing Company Wichita, KA Attn: Mr. C. F. Tiffany	1
McDonnell Douglas Aircraft Corp. P. O. Box 516 Lambert Field, MO 63166 Attn: Library	1
Douglas Aircraft Co. 3855 Lakewood Blvd. Mail Code 36-41 Long Beach, CA 90846 Attn: Mr. M. A. O'Connor, Jr.	1
General Dynamics P. O. Box 748 Forth Worth, TX 76101 Attn: Library	1
General Dynamics/Convair Aerospace P. O. Box 1128 San Diego, CA 92112 Attn: Library J. Jensen	1 1

Copies

General Electric Co.
 Interstate 75, Bldg. 500
 M.D. K221
 Cincinnati, OH 45215
 Attn: Mr. Leonard Beitch 1

General Electric Co.
 Aircraft Engine Group
 Cincinnati, OH 45215
 Attn: Dr. R. E. Duttweiler 1

General Electric Co.
 Aircraft Engine Group
 Cincinnati, OH 45215
 Attn: Dr. B. L. Koff 1

General Electric Co. - 175
 Gimson Road - K59
 Cincinnati, OH 45215
 Attn: Mr. John Schneider 1

General Electric Company
 Aircraft Engine Group
 Lynn, MA 01902
 Attn: Mr. Herbert Garten 1

Grumman Aircraft Engineering Corp.
 Bethpage, Long Island, NY 11714
 Attn: Library 1

IIT Research Institute
 Technology Center
 Chicago, IL 60616
 Attn: Library 1
 I.M. Daniel 1

Lockheed California Co.
 P. O. Box 551
 Dept. 73-31, Bldg. 90, PL. A-1
 Burbank, CA 91520
 Attn: Mr. D. T. Pland 1

Lockheed California Co.
 P. O. Box 551
 Dept. 75-71, Bldg. 63, PL. A-1
 Burbank, CA 91520
 Attn: Mr. Jack E. Wignot 1

Northrop Space Laboratories
 3401 West Broadway
 Hawthorne, CA 90250
 Attn: Library 1

Copies

North American Rockwell, Inc.
 Rocketdyne Division
 6633 Canoga Ave.
 Canoga Park, CA 91304
 Attn: Library, Dept. 596-306

1

North American Rockwell, Inc.
 Space & Information Systems Div.
 12214 Lakewood Blvd.
 Downey, CA 90241
 Attn: Library

1

Norton Company
 Industrial Ceramics Div.
 Armor & Spectramic Products
 Worcester, MA 01606
 Attn: Mr. George E. Buron

1

Norton Company
 1 New Bond Street
 Industrial Ceramics Div.
 Worcester, MA 01606
 Attn: Mr. Paul B. Gardner

1

United Aircraft Corporation
 Pratt & Whitney Group
 Government Products Division
 P. O. B2691
 West Palm Beach, FL 33402
 Attn: Library
 Mr. J. T. Dixon

1

1

United Aircraft Corporation
 Pratt & Whitney Aircraft Group
 400 Main Street
 East Hartford, CT 06108
 Attn: Library
 Dr. J. E. Doherty
 Dr. S. A. Sattar
 Dr. A. T. Weaver

1

1

1

1

United Aircraft Corporation
 Hamilton Standard Division
 Winsor Locks, CT 06096
 Attn: Dr. G. P. Towsend

1

Aeronautical Research Association of
 Princeton, Inc.
 P. O. Box 2229
 Princeton, NJ 08540
 Attn: Dr. Thomas McDonough

1

Copies

Republic Aviation
Fairchild Hiller Corp.
Farmington, L.I., NY
Attn: Library 1

Rohr Industries
Foot of H Street
Chula Vista, CA 92010
Attn: Mr. John Meaney 1

TWA, Inc.
Kansas City International Airport
P.O. Box 20126
Kansas City, MO 64195
Attn: Mr. John J. Morelli 1

TRW Systems, Inc.
One Space Park
Redondo Beach, CA 90278
Attn: Technical Library,
Document Acquisition 1

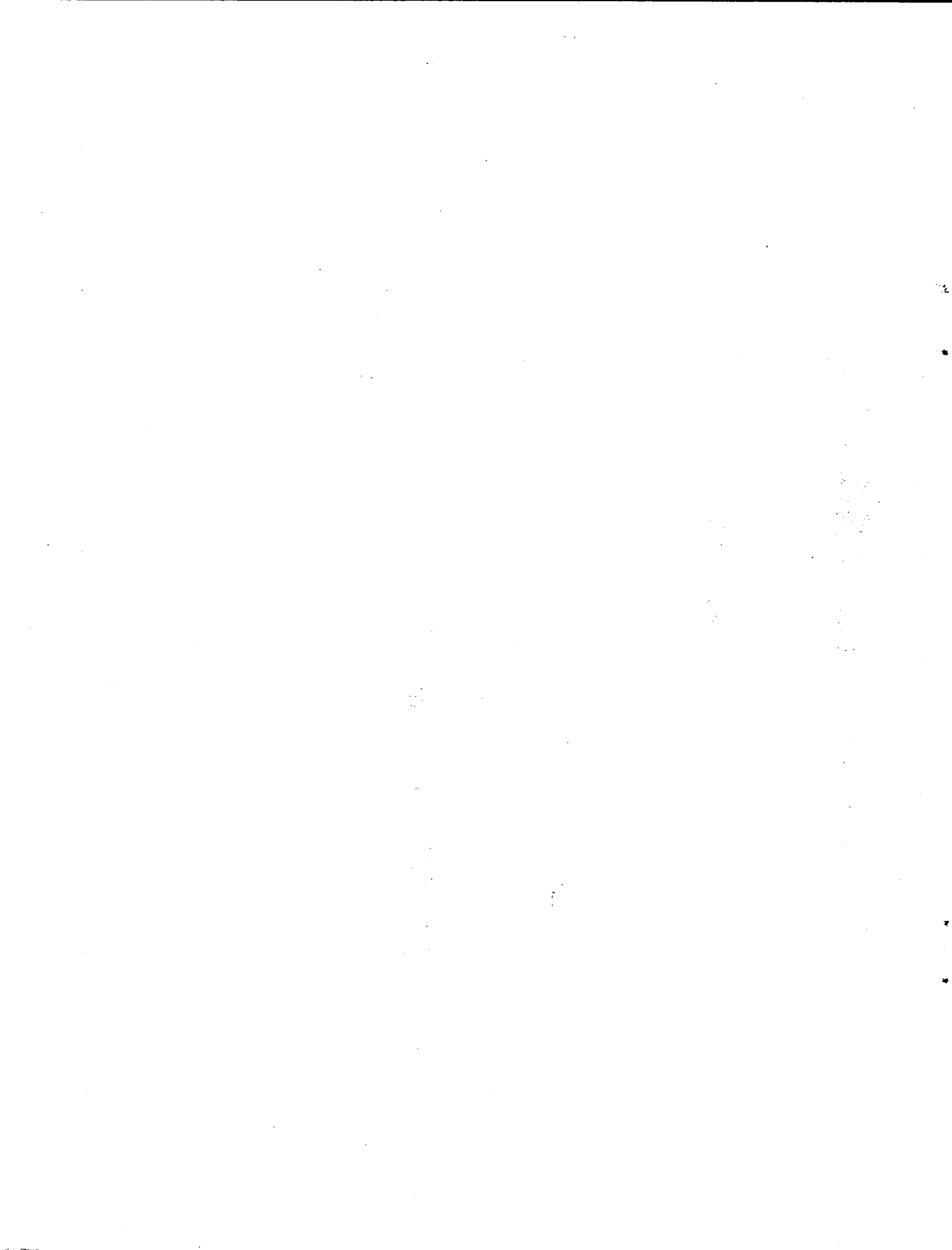
Mr. Herbert J. Rubel
1451 Holly Lane, N.E.
Atlanta, GA 30329 1

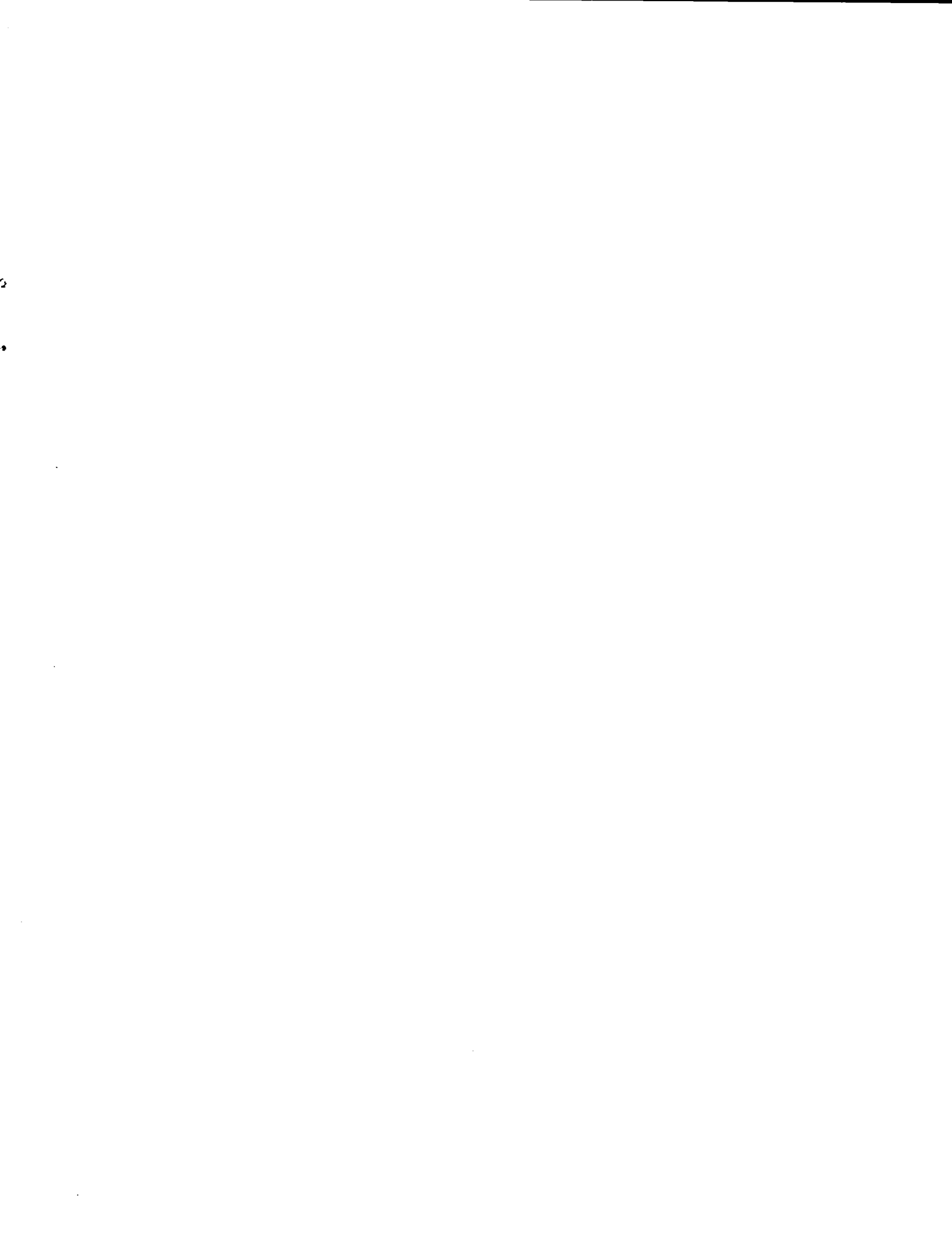
Canadair, Ltd.
P.O. Box 6087
Montreal, CANADA H3C 3G9
Attn: Mr. E. G. Carrington 1

Civil Aviation Authority
Airworthiness Division
Brabazon House
Redhill Surrey RH 1 1 SQ
ENGLAND
Attn: Mr. G. L. Gunstone 1

British Aircraft Corp., Ltd.
Commercial Aircraft Division
Filton House, Bristol BS 99 7AR
ENGLAND
Attn: Mr. J. C. Wallin
British Aircraft Corp., Ltd. 1

Rolls-Royce (1971) Limited
Moor Lane, P.O. Box 31
Derby DEX 8 8J
UNITED KINGDOM
Attn: Mr. Denis M. McCarthy
Chief Engineer, Staff Engineering 1





DO NOT REMOVE SLIP FROM MATERIAL

Delete your name from this slip when returning material to the library.

NAME	DATE	MS
N. Knight	6-98	903
L. Lawson	9-98	400